Turn-off luminescence sensing, white light emission and magnetic studies of two-dimensional lanthanide MOFs

Krishna Manna, Jean-Pascal Sutter, Srinivasan Natarajan

Turn off Luminescence Sensing, White – Light Emission and Magnetic Studies on Two-Dimensional Lanthanide MOFs

Krishna Manna[a], Jean-Pascal Sutter[b]* and Srinivasan Natarajan[a]*

[a] *Framework solids Laboratory, Solid State and Structural Chemistry Unit, Indian Institute of Science, Bangalore- 560012 (India). E-mail: snatarajan@iisc.ac.in*

[b] *Laboratoire de Chime de Coordination du CNRS, Université de Toulouse, CNRS, 205 route de Narbonne, 31077 Toulouse (France), E-mail : jean-pascal.sutter@lcc-toulouse.fr*

Abstract: [Ln(BPTA)$_{1.5}$(Phen)]·0.5DMF; Ln = Y, Eu, Gd, Tb, Dy (**1b-5b**) were prepared employing 2,5-bis(prop-2-yn-1-yloxy)terephthalic acid (2, 5 - BPTA) as the primary ligand and 2, 2′ bipyridine (**1a-5a**) and 1, 10 phenanthroline (**1b-5b**) as the secondary ligands. Single crystal structural studies on [Gd(BPTA)$_{1.5}$(Bpy)]·0.5DMF, **3a** and [Dy(BPTA)$_{1.5}$(Phen)]·0.5DMF, **5b** compounds indicated that the compounds have two-dimensional structure. The Y-compound exhibits blue emission and the other compounds exhibits emission in the expected region (λ_{ex} = 350 nm). White light emission was achieved by careful mixing of the red (Eu^{3+}) and green (Tb^{3+}) components in the blue emitting Y – compound. Thus, $Y_{0.96}Tb_{0.02}Eu_{0.02}$ (bpy), and $Y_{0.939}Tb_{0.06}Eu_{0.001}$ (phen) was found to show white emission, when excited using a wavelength of 350 nm. The introduction of N-N containing ancillary ligands (i.e. bpy and phen) increased the overall quantum yield (QY) of white light emission to 31% and 43% respectively. The high QY observed for the Tb and Eu compounds was found to be sensitive and selective for the fluorometric detection of azinphos-methyl pesticide and trinitrophenol (TNP) in aqueous medium in ppb level. The same behaviour was observed in utilising the compounds as an onsite paper strip sensors. Magnetic properties were also studied revealing for the Tb and Dy derivatives slow relaxation of the magnetisation at low temperature. The present study highlights the usefulness of rigid π – conjugated molecules such as 2, 2′ - bipyridine and 1, 10 – phenanthroline in enhancing the many utilities of rare – earth containing MOFs towards white - light emission, sensing of harmful and dangerous substances and magnetic properties.

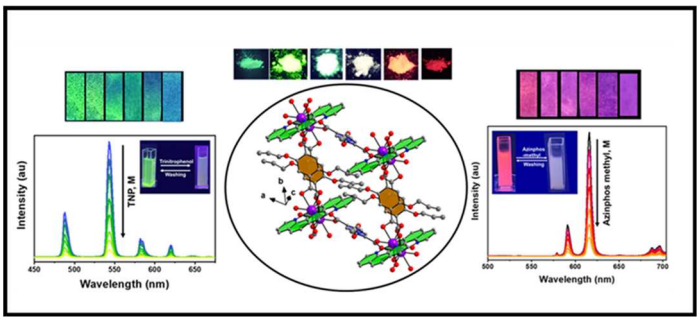

Introduction

The predictable coordination geometries of the *d*-block elements have been employed in the study of coordination polymers/MOFs over the years.[1–9] The *f* – block elements have also been explored for their structure and properties.[10–14] The *f* – block rare earth elements, generally, have coordination numbers that are higher than that observed with the *d* – block elements. One of the interests in the use of rare – earth elements is their characteristic emissions arising from the sharp *f-f* electronic transitions.[15–19] One of the drawbacks of the lanthanide ions is their low molar absorptivity, which results in weak emission when excited directly.[20–23] The lanthanide ion emission, however, can be significantly enhanced by employing suitable chelate that can absorb and transfer the energy across to the lanthanide ions.[24–29] The direct excitation of the ligand (chelate) leads to the excited singlet state, which undergoes a triplet state transition through intersystem crossing. Strong lanthanide metal – centred emission can be observed by the energy transfer from the excited triplet state of the chelate to the lanthanide ion through a non – radiative process. This approach is known as 'antenna effect' and has been exploited extensively over the years to observe intense and characteristic emissions from the lanthanide ions.[11,30–33]

In inorganic materials chemistry, compounds possessing multi – functionality has been one of the desired properties. In MOFs, the multi – functionality is achieved by having functional ligands.[34–37] The ligands, both primary as well as secondary, have extended π – conjugation and can be employed for many different applications. The π – conjugated ligands give MOFs excellent luminescence behaviour, which were exploited towards the detection of many different species in aqueous solutions, with low detection limits.[38–43] Thus, many harmful ions such as arsenate, chromates, organic molecules including pesticides, explosives *etc* have been detected by the use of turn - off luminescence behaviour.[44–53]

Along this line, we have reported 2D and 3D framework compounds assembled from Ln(III) ions and 2,5-bis(prop-2-yn-1-yloxy)terephthalic acid (2, 5 **–** BPTA) that exhibited luminescence and catalytic properties.[54] In these compounds, the coordination spheres of the Ln ions contained H_2O as the ligand which is not ideal for luminescence efficiency. In the present study, the coordinated water molecules were replaced with 2, 2' - bipyridine and 1, 10 – phenanthroline units, which enhances the luminescence behaviour of the rare -earth ions significantly. We have prepared rare – earth containing two dimensional layered compounds, $[Ln(BPTA)_{1.5}(Bpy)]\cdot 0.5DMF$ and $[Ln(BPTA)_{1.5}(Phen)]\cdot 0.5DMF$; (Ln = Y, Eu, Gd, Tb, Dy), and explored the compounds towards the sensing of pesticides (azinphos-methyl), nitroaromatics (trinitrophenol). In addition, the Y – compound, $[Y(BPTA)_{1.5}(Bpy)]\cdot 0.5DMF$ and $[Y(BPTA)_{1.5}(Phen)]\cdot 0.5DMF$ were found to be blue emitting – aided by the primary ligand, which were modified to obtain white light emission. The magnetic behaviour was also investigated. In this paper, we describe and discuss the synthesis and characterization of the compounds.

Experimental

Synthesis: The synthesis of all the compounds, $[Ln(BPTA)_{1.5}(Bpy)]\cdot 0.5DMF$ and $[Ln(BPTA)_{1.5}(Phen)]\cdot 0.5DMF$; (Ln = Y, Eu, Gd, Tb, Dy) were carried out by slow inter – diffusion of three different layered solutions of respectively, the Ln(III) ion, the bpy or phen ligand and 2,5 – BPTA in 1/1/1 ratio, following a procedure reported earlier.[54] The synthesis conditions are summarized in ESI (Table S1).

Initial Characterization: The compounds were characterized using: (i) Powder X-ray diffraction (PXRD) (Figure S1, S2); (ii) SEM-EDX analysis (Figure S3, S4); (iii) the IR spectra (Figure S5); (iv) the UV-Vis spectra (Figure S6); (v) Thermogravimetric analysis (TGA) (Metler-Toledo) (Figure S7); (vi) the

photoluminescence spectra (Horiba FluoroMax Plus Figure S15) and elemental analyses (carbon, hydrogen, oxygen and nitrogen) (Table S1B).

Magnetic measurements were carried out Physical property Measurement System (PPMS, Quantum Design) using VSM or ACMS configuration for either DC or AC measurements. The samples were compressed in pellets or mixed to grease and hold in a gelatin capsule. Magnetic susceptibility data were collected in a field of 1 kOe and isothermal magnetization were recorded up to 70 kOe. The susceptibility data have been corrected for the diamagnetic contributions of the holder and all the atoms using the Pascal tables.[55] AC susceptibility were recorded with H_{AC} = 3 Oe in a frequency range between 1 and 10^4 Hz. The software PHI was used for fitting the $\chi_M T = f(T)$ and M = $f(H)$ behaviors.[56]

Single crystal structure determination was carried out at 100 K on a Bruker SMART APEX CCD X-ray diffractometer using graphite-monochromator MoKα radiation (λ = 0.71073 Å). The structures were solved by direct methods and refined against $|F^2|$ using full-matrix least-squares employing SHELXL2018 suite of programs.[57,58] The alkyne chains of the ligand and lattice DMF molecule were found to be disordered and modelled isotropically.[59] A summary of the crystal data and the relevant refinement parameters for the compounds $[Gd(BPTA)_{1.5}(Bpy)]\cdot 0.5DMF$ **(3a)** and $[Dy(BPTA)_{1.5}(Phen)]\cdot 0.5DMF$ **(5b)** are listed in Table 1. CCDC 2262684, 2262689 contain the crystallographic data for this paper. The data can be obtained free of charge from The Cambridge Crystallographic Data Centre via www.ccdc.cam.ac.uk/data_request/cif.

IR spectroscopic studies indicated the expected IR bands (Figure S5), which are summarized in Table S5 (Figure S5, ESI). The UV-Vis absorption spectra indicated bands corresponding to the π-π* and n-π* transitions of the ligands, 2, 5 – BPTA, 2, 2′ - bipyridine and 1, 10 – phenanthroline.[60,61] The spectra exhibited a red shift in the absorption of the π-π* and n-π* transitions in the metalated compounds (Figure S6, Table S6).

Thermal Studies: Thermogravimetric analysis (TGA) on all the compounds was carried out from 30–1000 °C (heating rate = 5 °C/min) in flowing N_2 atmosphere (Figure S7). The thermal decomposition behaviour of all the compounds (**1a-5a** and **1b-5b)** were found to be comparable (Figure S7). For example, the Y compound (**1a**), exhibited a weight loss of ~2.7% in the region of 130-190 °C which corresponds to the loss of half of lattice DMF molecule (calc ~ 2.5%). After the elimination of the DMF, the compound exhibits a broad weight loss, which is accompanied by the decomposition of the framework. The final product after the TGA studies were found to be Y_2O_3 PXRD (Figure S8).

Results and Discussions

Structure of the compounds

The obtained product after the synthesis, in all the cases were single crystals only. The single crystal structures were found to exhibit considerable disorder in the structure, specially involving the terminal $-CH_2-C\equiv CH$ units of the ligand. We obtained much better-quality crystals for $[Gd(BPTA)_{1.5}(Bpy)]\cdot 0.5DMF$ **(3a)** and $[Dy(BPTA)_{1.5}(Phen)]\cdot 0.5DMF$ **(5b)** samples, which were solved to obtain the single crystal structures. The experimental powder diffraction data (PXRD) for **3a** and **5b** were found to match exactly with the simulated powder diffraction data (PXRD) obtained from single crystal structure. The experimental PXRD patterns of the other compounds with 2, 2′ bipyridine was matched with that of $[Gd(BPTA)_{1.5}(Bpy)]\cdot 0.5DMF$**, 3a**, and for the 1, 10 phenanthroline compounds the PXRD patterns were matched with $[Dy(BPTA)_{1.5}(Phen)]\cdot 0.5DMF$, **5b** to establish the phase purity of the prepared compounds. In all the compounds, we did not observe any additional peaks. (Figure S1a, S1b). The structure of the Gd – containing compound **(3a)** is used as an illustration of the structural arrangement of 2, 2′ bipyridine compounds and Dy – containing compound (**5b**) is used for phenanthroline containing compounds. **3a** has 48 non-hydrogen atoms with one crystallographically independent Gd^{3+} ion, one and half 2, 5 – BPTA anion and one 2, 2′ bipyridine (Figure S9a). The primary

ligand, 2, 5 –BPTA, can be considered into two different types (acid-1 and acid-2) for the ease of describing the connectivity (Figure S9b).

Structural parameter	Compound 3a	Compound 5b
Empirical formula	$[Gd(BPTA)_{1.5}(Bpy)]\cdot 0.5DMF$	$[Dy(BPTA)_{1.5}(Phen)]\cdot 0.5DMF$
Crystal system	Triclinic	Triclinic
Space group	P-*1*	P-*1*
a (Å)	11.08(7)	11.27(9)
b (Å)	11.51(7)	11.43(9)
c (Å)	12.37(7)	12.97(10)
α(º)	82.11(2)	80.42(3)
β(º)	89.57(2)	72.42(3)
γ(º)	71.20(2)	72.44(3)
V (Å^3)	1479.24(16)	1513.5(2)
Z	1	1
T(K)	100(2)	100(2)
ρ_{calcd} (g cm^{-3})	1.702	1.728
μ (mm^{-1})	2.305	2.532
λ (Mo Kα/Å)	0.71073	0.71073
θ range (deg)	1.66– 25.13	1.88 – 25.04
Final *R* indices[$I>2\sigma(I)$]	*R1*= 0.038 *wR2*= 0.091	*R1*= 0.040 *wR2*= 0.081
R indices (all data)	*R1*= 0.048 *wR2*= 0.096	*R1*= 0.056 *wR2*= 0.088
R_{int}	0.0769	0.09
$^a R_1 = \sum \lvert\lvert F_o\rvert - \lvert F_c\rvert\rvert / \sum \lvert F_o\rvert$; $wR_2 = \{\sum [w(F_o^2 - F_c^2)] / \sum [w(F_o^2)^2]\}^{1/2}$. $w = 1/[\rho^2(F_o)^2 + (aP)^2 + bP]$. $P = [\max(F_o, 0) + 2(F_c)^2]/3$ where a = 0.039 and b = 5.866 for **3a;** a = 0.0297 and b = 4.16 for **5b**		

Table 1: Crystallographic data and structure refinement parameters for the bipyridine and 1, 10 phenanthroline compounds $[Gd(BPTA)_{1.5}(Bpy)]\cdot 0.5DMF$ **(3a)** and $[Dy(BPTA)_{1.5}(Phen)]\cdot 0.5DMF$ **(5b)**

The Gd^{3+} ion is 9 – coordinated with seven oxygen atoms and two nitrogen atoms of 2, 2' bipyridine forming a distorted monocapped square antiprismatic arrangement (Figure S10a). All the seven oxygens, are from the carboxylate group, of which O1_4 has a μ^3 connectivity connecting two metal centres and a carbon, and the remaining ones have μ^2 connectivity (one metal centre and one carbon atom). The important bond distances and angles are listed in Table S2, S3. Of the two acids, acid 1 connects to four Gd-centres through the carboxylate oxygens and the acid-2 connects to three Gd-centres (Figure S9b)**.**

The two-dimensional structure has edge shared gadolinium dimers (Figure 1a), which are connected through the 2, 5 – BPTA ligand (acid-1) forming a one-dimensional chain (Figure S11a). A similar one-dimensional chain is also formed by the connectivity with the acid-2 (Figure S11b). The two 1D chains are connected to give rise to a two-dimensional layer (Figure 1b). The 2, 2' bipyridine unit binds in the cis mode to the Gd - centre with an intra layer separation of 11.50 Å between the two bipyridine units (Figure S11c). The inter – layer separation between the 2, 2' bipyridine ligand was observed to be 3.99 Å (centroid – centroid distance Figure 1c). In the Dy compound with 1, 10 phenanthroline, the structural arrangement is similar to that observed with 2, 2' - bipyridine, except that the 1, 10 – phenanthroline units bind with the metal centre and the metal centre has a trigonal tricapped prismatic arrangement (Figure S10b, Figure S12 – S14). The phenanthroline units have an intra-layer separation of 11.5 Å (Figure S14) and a inter layer separation of 3.65 Å (Figure 2).

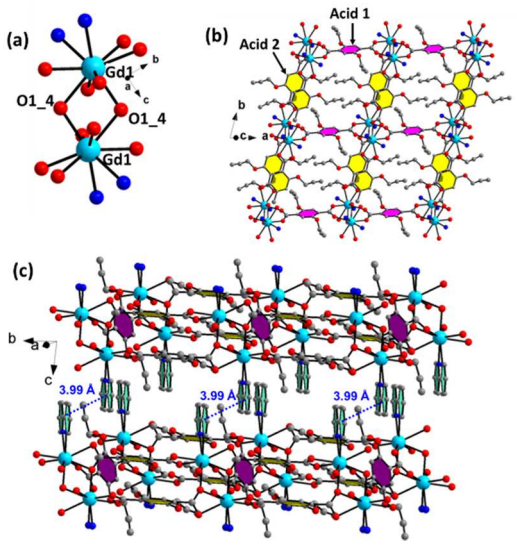

Figure 1. (a) The view of $Gd_2O_{12}N_4$ dimers observed in compound **3a (b)** View of the 2D layers. Note the two different acids (acid 1 and acid 2) that connect the dimers to extended layer structure **(c)** The arrangement of the layers. Note that the secondary ligand, 2, 2′ bipyridine, projects into the inter – lamellar space.

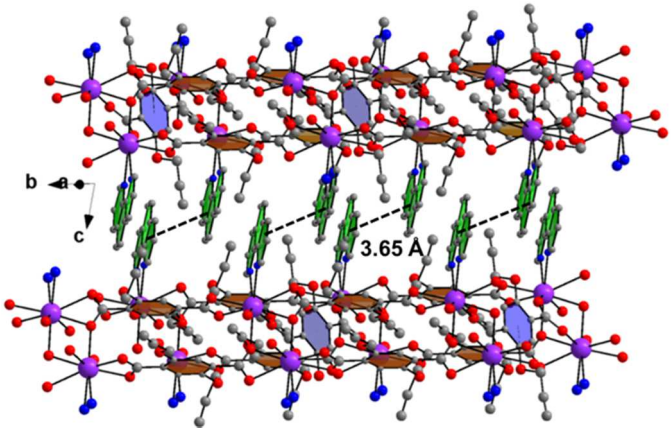

Figure 2. View of the layer arrangement in compound **5b.** The 1, 10 phenanthroline units hang in the inter layer space from the rare – earth centres

Photophysical studies Luminescence

The lanthanide compounds are known to exhibit characteristic and enhanced emissions when sensitized suitably by molecules having π-systems.[62] The enhanced emission is especially noticeable when organic moieties with extended π – conjugation binds directly with the rare earth metal centres, which would improve the energy transfer. Normally the ligand molecules are excited to a singlet state, which undergoes intersystem crossing (ISC) to a triplet state and transfers the energy non – radiatively to the lanthanide ion, which then exhibits the characteristic emission.[63,64] In the present compounds, there are two ligands, one is the carboxylate, 2, 5 – BPTA, and the other is 2, 2′ - bipyridine or 1, 10 – phenanthroline. The ligand, 2, 5 – BPTA, was shown to behave as an antenna towards lanthanide emission,[54] as do bpy and phen.[65,35,66] molecules also exhibit luminescence. The 2, 5 – BPTA ligand exhibits a broad emission centred around 428 nm when excited using a wavelength of 350 nm. The 2, 2′ - bipyridine, on the other hand, gives an emission band centred at 380 nm (l_{ex} = 350 nm), and the phenanthroline moiety gives the emission centred at 430 nm (l_{ex} = 350 nm). The ligand centred

emission in the compounds containing the rare earth ions, exhibit a broad emission band in the range of 400-500 nm, when excited using a wavelength of 350 nm. This emission would be due to the intra-ligand luminescence (π* → n or π* → π) (Figure S15). The Dy compound **5a** exhibits sharp emissions at 477 and 573 nm with the former a bit weaker compared to the later, and for **5b (**λ_{ex}=350 nm) at 573 and 590 nm. These are characteristic emissions due to the *f–f* transitions $F_{9/2} \rightarrow {}^{6}H_{J}$ **,** where J=15, 13, 11 (Figure S15e, S15f).[67,68]

In case of the bipyridine containing compounds, (Ln = Eu^{3+} (**2a**), Tb^{3+} (**4a**), and Y^{3+} (**1a**)), we observed red, green, and blue emissions, when excited using a wavelength of 350 nm (Figure S16a). The Y compound exhibited a blue emission centred around 515 nm, which is the intra-ligand electronic transitions (π* → π transition). The Eu compound exhibits intense red emission with emission bands at 590, 616, 650, and 695 nm, which can be attributed to the $^5D_0 \rightarrow {}^7F_1$, $^5D_0 \rightarrow {}^7F_2$, $^5D_0 \rightarrow {}^7F_3$, and $^5D_0 \rightarrow {}^7F_4$ transitions, respectively. The Tb compound exhibits emission in the green region with bands at 488, 544, 585, and 620 nm, respectively, that corresponds to $^5D_4 \rightarrow {}^7F_6$, $^5D_4 \rightarrow {}^7F_5$, $^5D_4 \rightarrow {}^7F_4$, and $^5D_4 \rightarrow {}^7F_3$ transitions (Figure S16a). For the phenanthroline containing compounds also we observed similar emission behaviour (Figure S16b) upon excitation at 350 nm. It has been known that the water molecules, generally, reduces the lanthanide emission due to non – radiative decay associated with the vibronic coupling.[69–72] In the present study, the coordinated water molecules were replaced by 2, 2′ bipyridine and 1, 10 phenanthroline, which incidentally increases the rigidity of the structure resulting in an enhanced emission as well as lifetime for the Y, Tb and Eu compounds. The lifetime of the $^5D_0$ (Eu^{3+}), $^5D_4$ (Tb^{3+}) and Y^{3+} at ambient temperatures (298 K) was measured by monitoring the corresponding $^5D_0 \rightarrow {}^7F_2$ (Eu^{3+}) and $^5D_4 \rightarrow {}^7F_5$ (Tb^{3+}) transitions. The lifetime of the both the phenanthroline and bipyridine containing compounds were found to be 1.36 ms and 50.96 ms for the Y compound coordinated with bipyridine (**1a**) and phenanthroline (**1b**) ligands. The lifetime of the Tb compound was found to be 1.004 ms (bipyridine, **4a**) and 1.27 ms (phenanthroline, **4b**). The Eu–MOF has a lifetime of 0.40 ms for the bipyridine compound (**2a**) and 1.32 ms in the case of the phenanthroline compound **(2b)** (Figure S17). It is satisfying to notice that the life - time values are indeed significantly increased compared to those observed for the compounds with coordinated water molecules.[54] The increased lifetime values likely result from the reduced vibronic coupling and increased rigidity to the structure brought about by the chelating N-N ligand. The chelation also appears to increase the overall intensity of the emission.[73–78]

White light emission studies

The luminescence study with Dy derivative (**5a**) indicated emission at 477 nm (blue) and 573 nm (yellow) regions (Figure S15e). There have been indications that the Dy – compounds under suitable conditions can exhibit white light emission.[68,79] In our studies, we found the 477 nm emission to be much weaker compared to the 573 emission. As a result, the blue emission was found to be dominant (yellow component intensity is very less) and a white emission is not observed. The chromaticity data was found to be (0.17, 0.107), which suggests only blue emission and not white emission.

In order to achieve a white light emission in the present compounds, we turned our attention to the three-component option. As, we have established blue, green and red emissions from Y, Tb and Eu – derivatives we attempted an appropriate mixing of these three Ln ions in a same compound to attain white light emission. To this end, we have doped the Y MOFs (**1a** and **1b**) with different concentrations of Eu^{3+} and Tb^{3+} ions. Before, we have screened single rare – earth ion doping to achieve maximum intensity in the emission of the Eu^{3+}/Tb^{3+} ion in the Y frameworks. These studies indicated that the highest emission intensity was achieved at 3% Tb^{3+} and 5% Eu^{3+} substitutions in **1a** (Figure S18a, 18b) and 7% Tb^{3+} and 0.5% Eu^{3+} substitution in **1b** (Figure S19a, S19b). The bipyridine containing Y compound was initially screened towards white light emission by introducing both the Tb^{3+} and Eu^{3+} ions. Thus, 2% of the Tb^{3+} ions substituted Y compound was employed as the base compound and the

Eu^{3+} ion concentration was varied (0%, 0.5%, 1%, 2%, 3%, and 4%). We noticed a progressive change in colour which eventually gave the white light emission at 2% Eu^{3+} substitution (Figure 3a). This was confirmed by the CIE chromaticity coordinates indicating that at 2% Eu^{3+} substitution white light emission was obtained (CIE coordinate: 0.33. 0.345) (Figure 4a, Table S7). On higher substitution of Eu^{3+} ions, we observed an increase in the red luminescence (Figure 3a).

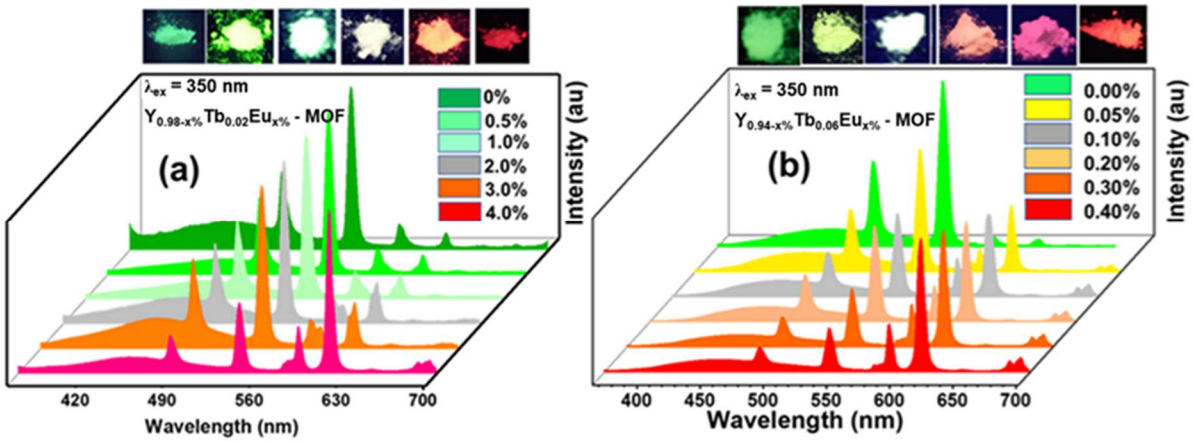

Figure 3. (a) PL emission spectra (λ_{ex} = 350 nm) of bipyridine containing $Y_{0.98-x\%}Tb_{0.02}Eu_{x\%}$ samples with different Eu^{3+} concentrations (0 < x < 4.0) **(b)** PL emission spectra (λ_{ex} = 350 nm) of 1, 10 phenanthroline containing $Y_{0.94-x\%}Tb_{0.06}Eu_{x\%}$ samples with different Eu^{3+} concentrations (0 < x < 0.4). Note that white light emission was observed at 2 % and 0.1 % for the bpy and phen compounds, respectively.

The phenanthroline containing compounds were also subjected to a similar study with 2% Tb^{3+} ions substituted in the Y compound as the starting material and varying the Eu^{3+} ions concentration from x = 0.0, 0.5, 1.0, 2.0, 3.0, 4.0 %. This approach resulted in compounds having green to red emission without giving rise to a white emission (see Figure S20). Then, we reduced the red component (Eu^{3+}) significantly to small values of x = 0.0, 0.05. 0.1, 0.2, 0.3, 0.4 %. This was needed as we observed maximum intensity for the red emission with a 0.5% of Eu^{3+} content. The lower concentrations of red component in the compounds, however, gave emission in the orange region. It occurred to us that to observe the white emission, the green component needs to be increased. Thus, we prepared compounds having 6% Tb^{3+} as the base compound and varied the Eu^{3+} ions concentration with Eu^{3+} (x = 0.0, 0.05. 0.1, 0.2, 0.3, 0.4 %). This approach was found to be successful and we observed a gradual change in colour from green to red via white with the increase of the Eu^{3+} concentration. White light emission was achieved at 0.1% Eu^{3+} concentration in $Y_{0.939}Tb_{0.06}Eu_{0.001}$ compound (Figure 3b); with the CIE chromaticity coordinates found to be close to the ideal value for the white light emission (CIE: 0.332, 0.331) (Figure 4b, Table S7). When co – doping Eu^{3+} ions in $Y_{0.94-x}Tb_{0.06}Eu_x$ compounds, it was observed that the emission intensity of Tb^{3+} ion decreased on increasing the concentration of Eu^{3+} ions. This is in agreement with an energy transfer from Tb^{3+} ions to Eu^{3+} ions, which has been observed before.[80–83]

We made attempts to understand the transfer of energy from the Tb^{3+} ions to the Eu^{3+} ions. For this, we recorded the excitation spectra of the Y-MOF: Eu^{3+} and the emission spectrum of Y-MOF: Tb^{3+} compound with both the phenanthroline as well as bipyridine. As can be seen in Figure S21a, S21b, there is an overlap between the excitation spectra of Eu^{3+} and emission spectra of Tb^{3+} containing compounds, which supports an energy transfer between the Tb^{3+} and Eu^{3+} in the mixed – Ln materials. We have investigated the excitation spectrum of the $Y_{0.96-x}Tb_{0.02}Eu_{0.02}$ – compound (bpy) and monitored the emission of the $^5D_0 \rightarrow {}^7F_2$ transition of Eu^{3+} ions at 616 nm. The excitation spectrum has both the ligand centred transition as well as the *f–f* transitions of the Eu^{3+} ions, along with the $^7F_6 \rightarrow {}^5D_4$ (488 nm) transition of the Tb^{3+} ions (Figure S22a). The emission spectra when excited at λ_{ex}=488 nm, ($^7F_6 \rightarrow$

$^5D_4$ transition), gave the emission that correspond to the Eu^{3+} ions (Figure S22b). This indicates good energy transfer between the Tb^{3+} and Eu^{3+} metal centres. Similar behaviour was also noted for the phenanthroline derivatives (Figure S23a, S23b).

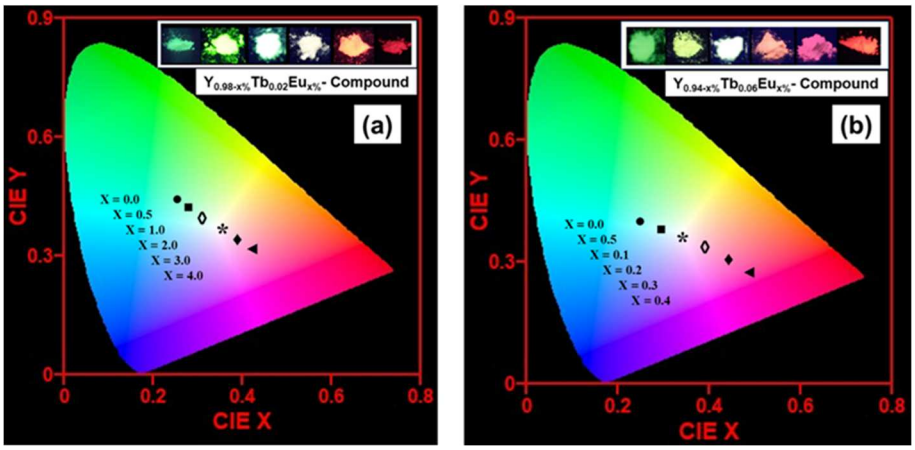

Figure 4. CIE colour coordinate diagram of **(a)** $Y_{0.98-x\%}Tb_{0.02}Eu_{x\%}$ samples ($0 < x < 4.0$) and **(b)** $Y_{0.94-x\%}Tb_{0.06}Eu_{x\%}$ samples ($0 < x < 0.40$) with different Eu^{3+} concentrations. The insets show the actual emission colour (λ_{ex} = 350 nm).

To further understand the energy transfer from Tb^{3+} ions to Eu^{3+} ions, we have monitored the fluorescence decay of the Tb^{3+} in $Y_{0.98-x}Tb_{0.02}Eu_x$– compound ($0 < x < 4.0$ in bpy derivatives) (λ_{ex} 350 nm) at 544 nm ($^5D_4 \rightarrow {}^7F_5$ transition, Figure 5a). The average lifetime of the Tb^{3+} ions continuously decrease with increase in the Eu^{3+} concentration: 1.03, 0.83, 0.81, 0.79, 0.73 and 0.62 ms for x = 0, 0.5, 1.0, 2.0, 3.0 and 4.0. Same trend was found for the phenanthroline containing $Y_{0.94-x}Tb_{0.06}Eu_x$– compounds ($0 < x < 0.4$, λ_{ex} = 350 nm), where the lifetime of the Tb^{3+} ions appear to decay somewhat faster with lifetime values of 1.40, 1.31, 1.25, 0.84, 0.61 and 0.49 ms for x = 0, 0.05, 0.10, 0.2, 0.3 and 0.4, respectively (Figure 5b). We have also plotted the lifetime values of the Tb^{3+} ions *vs.* the concentration of Eu^{3+} ions, which appears to indicate that the lifetime decreases monotonically with increasing the concentration of the Eu^{3+} ions (Figure S24).

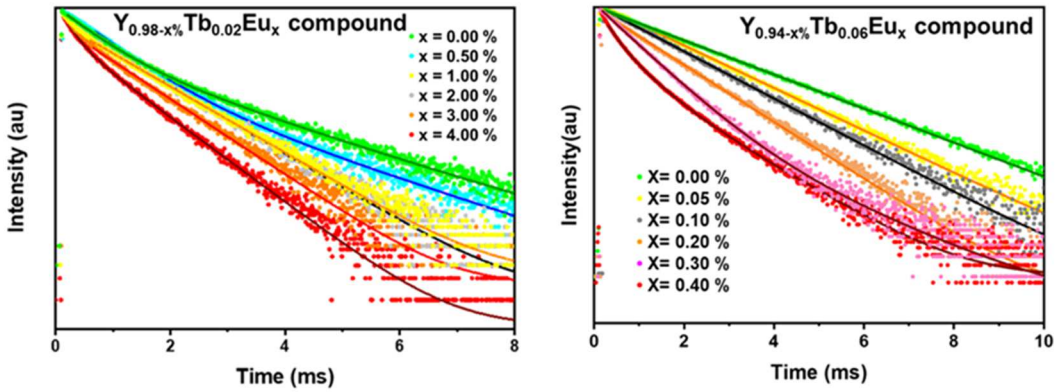

Figure 5. The decay curves for the luminescence of Tb^{3+} ions as a function of different Eu^{3+} ion substitutions in **(a)** $Y_{0.98-x\%}Tb_{0.02}Eu_{x\%}$ and **(b)** $Y_{0.94-x\%}Tb_{0.06}Eu_{x\%}$ – samples, (λ_{ex} = 350 nm and monitored at 544 nm).

It is probably pertinent to compare the white light emission in the present compounds with those reported on similar compounds (Table S8).[79–83] It is clear that the QY as well as the correlated colour temperature (CCT) values observed in the present compounds are reasonable and comparable to the

reported compounds, especially those containing the rare earth ions. The present compounds have 2, 2' - bipyridine and 1, 10 – phenanthroline moieties binding with the rare earth centre, which provides excellent antenna effect.[19,84–91] The combination of the antenna effect, energy transfer from Tb^{3+} ions to Eu^{3+} ions along with the blue emission from the Y – framework appears to be a good recipe for the white light emission (Figure 6). It may be noted that the white light emission is achieved with small concentrations of the Tb^{3+} and Eu^{3+} ions in the host lattice compared to the previously reported ones (Table S8). The quantum yield (QY) of the white light achieved in the present study was found to be 31% in the bipyridine containing compound ($Y_{0.96}Tb_{0.02}Eu_{0.02}$) and 43% for the phenanthroline containing one ($Y_{0.939}Tb_{0.06}Eu_{0.001}$). The observed QY values compares well with those reported before for similar compounds (Table S8).[92–102] The QY for the other rare earth compounds, prepared in the present study, also exhibits reasonable values: 22 % (**1a**), 37 % (**1b**), 31 % (**2a**), 49 % (**2b**), 83 % (**4a**) and 79 % (**4b**) has been obtained.

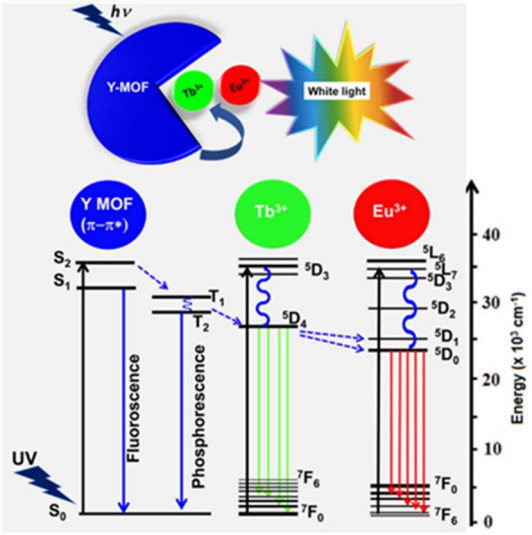

Figure 6. Schematic of the energy transfer mechanism.

It has been known that the Tb^{3+} containing compounds always have better QY values compared to the Eu^{3+} containing ones.[18,103] This is due to the smaller energy gap of $^5D_0 \rightarrow {}^7F_0$ levels of Eu^{3+} ions compared to the $^5D_4 \rightarrow {}^7F_0$ energy levels of Tb^{3+} ions.[17,109] In the present compounds also we observed a similar trend with the Eu^{3+} containing compounds exhibiting a lower quantum yield compared to the Tb^{3+} containing ones. The net quantum yield between the bpy and phen containing compounds differs only marginally. It has been proposed that in designing suitable ligands for the antenna effect, it is preferable that the ΔE of the ligand ($^1S^* \rightarrow {}^3T^*$) is ≈ 5000 cm^{-1} and that of the lanthanides ΔE ($^3T^* \rightarrow$ lanthanide emission band) in the range of ~ 2500 – 3000 cm^{-1}.[103] These values are guideline values only. In many cases small differences in the ligand states can lead to the difference in the overlap between the emission spectra of the donor and the absorption spectra of the acceptor. Such situations can lead to differences in the observed QY of the lanthanide compounds.[109-115] This may be the reason for the observed difference in the QY between the bpy and phen containing compounds of europium and terbium.

Sensing studies

The luminescence behaviour of the MOF compounds have been exploited towards the detection of harmful substances in aqueous solutions.[36,67,104–106] Though much of the study concentrated on the luminescence behaviour of the organic linkers of the MOFs, there has been increasing attention towards utilising the lanthanide luminescence as the probe.[107–111] The good emission efficiency of the present Eu^{3+} (**2a, 2b**) and Tb^{3+} (**4a, 4b**) materials made them desirable to

explore these compounds towards the fluorescence turn off detection of some of harmful pesticides and nitroaromatics in aqueous solution. For this, aqueous dispersions were prepared by mixing 2 mg of the Tb and Eu -compounds into 2 mL of H_2O. This was ultrasonicated for 1 hr at room temperature and the resulting suspension was diluted to 10 mL. Subsequently, using aliquots of 2 mL of this mixture, 10 mM solution of different nitroaromatics and pesticides in acetonitrile were added incrementally.

Pesticides Detection in Aqueous Medium: We have explored the detection of azinphos-methyl pesticide in aqueous solution. Azinphos-methyl is an organophosphorus pesticide that has been in widespread use. It has been shown that organs and tissues of human beings are severely affected towards the exposure of organophosphorus compounds,[44] therefore, it is important to detect the presence of these in aqueous solutions. We monitored the luminescence intensity of 616 nm ($^5D_0 \rightarrow {}^7F_2$) for Eu – phen and 544 nm ($^5D_4 \rightarrow {}^7F_5$) for Tb – phen compounds (l_{ex} = 350 nm) with and without the addition of the pesticides.

The luminescence quenching (turn off) studies were carried out with an incremental addition of azinphos-methyl to the Tb and Eu dispersed in water. The luminescence of MOFs gradually loses the intensity up to 92 % of the initial intensity for the Tb – phen and 90 % in the case of Eu-phen on adding 75 µM of azinphos–methyl solution (Figure 7, inset shows the change in the colour during the incremental addition of the pesticide). A luminescence quenching titrations at low concentrations (30 µM) of the pesticide (Figure 8). It has been established that the low concentration linear response is because of the static quenching due to the interactions between the analytes and the host. At higher concentrations, energy would be transferred between the host and the analytes and is known as the dynamic quenching (Figure S25). It has been known that the excitation light source may also be absorbed by the analyte and indirectly contribute to the quenching of the luminescence in addition to the static and dynamic quenching. From the Stern – Volmer plot, the obtained K_{SV} values was found to be 1.88 × 10^4 M^{-1} for the Tb-phen MOF and 3.8 × 10^4 for the Eu-phen MOF (Figure 8). These values suggest good sensitivity towards azinphos–methyl pesticide detection.

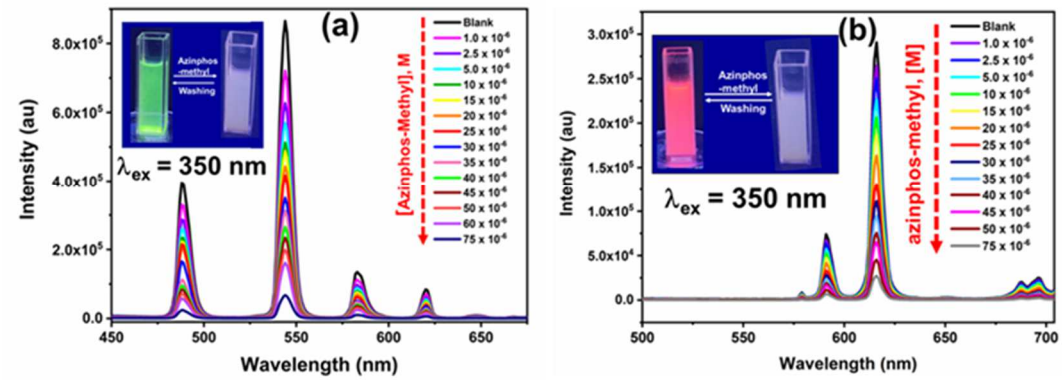

Figure 7. Emission spectra of **(a)** Tb-phen MOF and **(b)** Eu-phen MOF upon incremental addition of azinphos-methyl (λ_{ex} = 350 nm).

The limit of detection (LOD) was calculated to be 1.06 ppb and 4.93 ppb, respectively, for azinphos-methyl pesticide using the Tb and Eu – phen compounds (Table S9). These values are comparable to those reported earlier in the literature (Figure S26).[41,42,112,113] The selectivity in sensing of azinphos-methyl was examined in the presence of other pesticides (Figure S27a, 27b). The investigations indicated that the Tb and Eu-phen compounds are selective for azinphos-methyl only. We observed significant changes in the luminescence spectra for the azinphos-methyl pesticide and a small change for chlorpyrifos. For other pesticides, the decrease in the luminescence intensity was marginal (Figure S28a and Figure S28b).

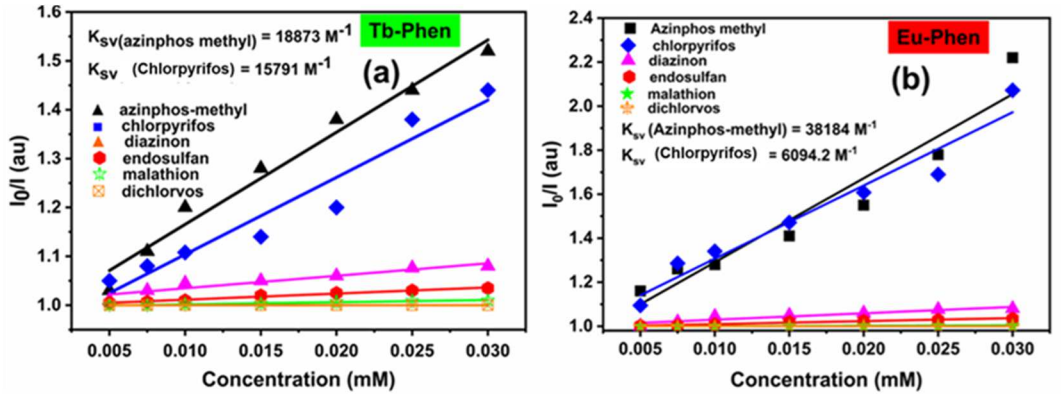

Figure 8. Plot of I_0/I of **(a)** Tb and **(b)** Eu-phen MOFs (at 544 nm and 616 nm) *vs* concentration of azinphos-methyl (up to 30 µM).

We have examined the stability of the MOF compounds towards the fluorescence detection of azinphos-methyl. For this, the MOF suspension was allowed to be in contact with 75 µM azinphos-methyl solution for 24 h at room temperature. The compound was filtered, and the structural integrity was investigated by PXRD. The PXRD patterns were found to be consistent with the simulated PXRD patterns of the compounds (Figure S29). The recyclability studies towards the sensing of azinphos-methyl were attempted, which indicated good stability as well as recyclability for at least up to four cycles (Figure S30).

The turn - off luminescence of the compounds towards azinphos-methyl intensity can be understood by comparing the absorption of the MOFs and the azinphos-methyl compound (Figure. S31a). The absorption bands of the azinphos-methyl are centred at ~300 nm, which has overlaps with the absorption spectra of the compounds (Figure. S31a). This overlap indicates competition for the excitation energy. In addition, the emission spectra of the MOFs and the tail of the UV-Vis absorption spectra of the azinphos-methyl has some overlap (Figure S31b). This opens up the possibility of resonance energy transfer between the lanthanide MOFs and the pesticide, which would help in the transfer of energy from the ligand excited state to the LUMO of the analytes.

We made attempts to understand the interactions between azinphos-methyl and the compounds, which leads to the luminescence quenching. To this end, we soaked the Eu and Tb MOF compounds **2b** and **4b** with azinphos-methyl solution for 12h followed by IR spectroscopic studies. The -C≡C stretching of the terminal alkyne for the pristine Tb - compound appears at 2126 cm^{-1} (Table S5), which appears to shift to 2121 cm^{-1} after the interaction with azinphos–methyl. This suggests that there may be some electron donation to the pesticide. The IR bands corresponding to -C=O and -C=N appears at 1670 and 1614 $cm^{-1}$for the pristine compound, which also exhibits a red shift of 4 and 12 cm^{-1} (Figure 9a). It is likely that the -C≡C moiety along with the –C=O and –C=N groups have interactions with the pesticide molecule. Similar observations were reported earlier.[114–117] Similar behaviour was also observed for the Eu-phen MOF compound as well (Figure 9b)

We have also explored the Tb and Eu – bpy compounds towards the luminescence sensing of azinphos-methyl pesticide, and the reduction of luminescence intensity was observed to be 90.9 % and 87 %, respectively, with a LOD value of 6.8 ppb and 7.17 ppb (Figure S32, S33).

The present compounds exhibit good sensitivity as well as selectivity towards azinphos-methyl. We wanted to explore the suitability of the present compounds towards the detection of azinphos-methyl without the need for extensive experimental set-up. Thus, we prepared a simple paper strip-based detector. The MOF suspension, which was employed for the liquid phase detection of azinphos-methyl, was prepared and 2 cm × 4 cm Whatman filter paper strips were dipped in the solution and dried under atmospheric conditions. The Tb/Eu (phen/bpy) coated paper strips exhibited the expected green and red luminescence under the UV lamp (Figure 10, inset). The Tb-phen coated paper strips were dipped

in 75 µM solutions of the azinphos-methyl for a few seconds and investigated under UV-lamp. We observed a drastic change in the fluorescence colour from green to black (Figure S34). This clearly indicates that the present compounds are useful for onsite detection of azinphos-methyl pesticide. We carried out the same studies on the test rare-earth coated paper strips with other well-known pesticides such as chlorpyrifos, diazinon, endosulfan, malathion and dichlorvos. We did not observe any drastic changes in the green luminescence in the presence of these pesticides (Figure S34). This study also confirms that the Tb-phen paper strips are specific for azinphos-methyl only.

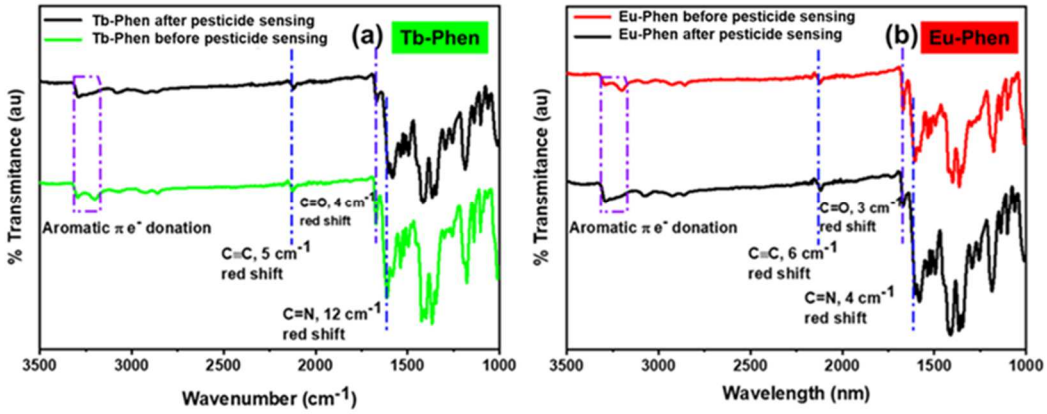

Figure 9. IR spectra of **(a)** Tb phen and **(b)** Eu phen MOF before and after the pesticide interactions. The vertical lines are the guide to highlight the shift in the bands.

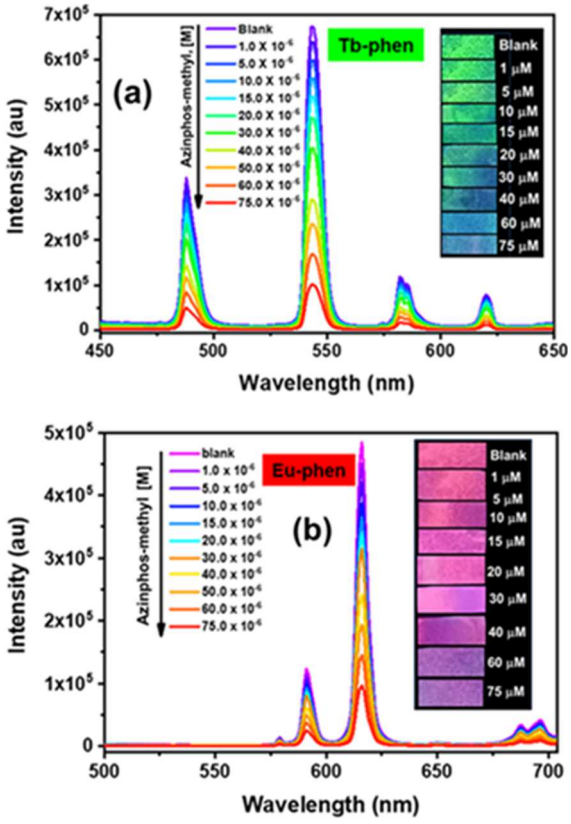

Figure 10. Paper strip-based sensing of azinphos-methyl **(a)** Tb-phen MOF and **(b)** Eu-phen MOF (λ_{ex} = 350 nm). Inset shows the actual colour of the paper strips under UV light.

The limit of detection (LOD) value for the azinphos-methyl was evaluated for the paper strip sensing by soaking the test strip with different concentrations of azinphos-methyl solution (1 μM to 75 μM). The paper strips were dried and examined under a UV lamp (Figure 10a, inset). The studies revealed that the intensity of the green emission gradually diminished with the increase in the concentrations of the azinphos-methyl solution (Figure 10a). The calculated LOD value (low concentration region), was found to be 4.45 ppb (Figure S35), which is closer to the LOD value obtained in aqueous medium (1.06 ppb). We have also examined the efficacy of the paper strip-based sensing for azinphos-methyl with Eu-phen, Tb-bpy, Eu-bpy, which gave LOD values of 5.28 ppb, 7.19 ppb and 16 ppb, respectively (Figure10b, S35 and S36).

Nitroaromatics Detection in Aqueous Medium: Similar to the pesticide detection, we have carried out the luminescence quenching titrations by gradual addition of the nitroaromatic acetonitrilic solutions to the MOFs dispersed in water. The change in the luminescence intensity (monitored at 616 nm for Eu-bpy and at 544 nm for Tb-bpy MOF) with the increasing addition of trinitrophenol (TNP) was monitored (Figure 11). We observed a reduction of 93 % and 92 % of the original luminescence intensity on addition of the TNP (100 μM).

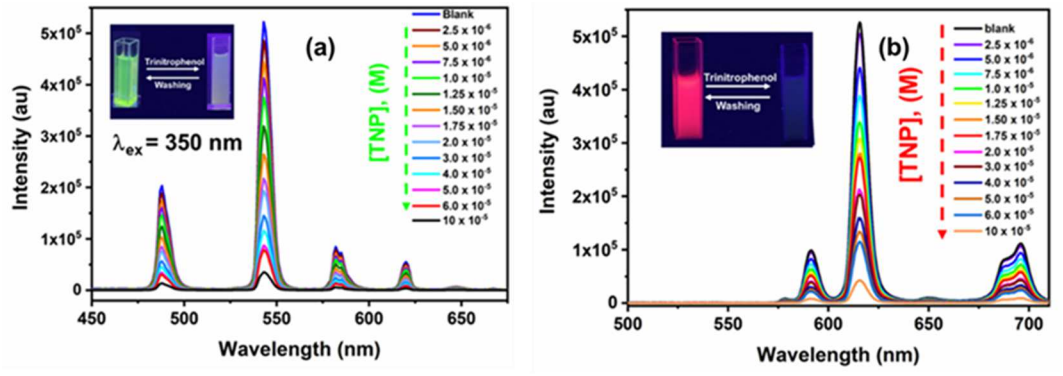

Figure 11. Emission spectra of **(a)** Tb-bpy and **(b)** Eu-bpy MOF upon incremental addition of Trinitrophenol (TNP) (λ_{ex} = 350 nm).

We have also examined the sensing of TNP in the presence of benzene and toluene as these aromatics usually remain as impurity along with nitroaromatics explosives. To this end, we added toluene and benzene (100 μM each) to the Tb and Eu-bpy MOF compounds followed by the stepwise addition of TNP. We observed that the reduction of the luminescence intensity was unaffected by the presence of benzene and toluene (Figure S37, S38). We have checked the luminescence quenching behaviour with other substituted phenol derivatives, like 4 – aminophenol, 4-aminobenzonitrile, 4-chlorophenol etc., and we observed that the luminescence is unaffected by the addition of these compounds to the MOF solutions (Figure S37, S38). The calculated K_{SV} values for the TNP sensing was found to be 73428 M^{-1} for the Eu – bpy MOF and 78476 M^{-1} for the Tb -bpy MOF. The large K_{SV} values indicates that the presence of TNP turns off the luminescence intensity of the Tb and Eu- bpy MOFs (Figure 12). The Stern-Volmer fitting of the luminescence data indicates both static quenching (low concentrations) and dynamic quenching (higher concentrations) would be responsible for the loss of luminescence intensity (Figure S39). The calculated LOD value was found to be 0.97 and 1.23 ppb (Figure S40, Table S9). The Tb and Eu – phen compounds exhibited a related turn-off luminescence sensing of TNP, (λ_{ex} = 350 nm); a reduction of luminescence intensity of respectively, 95 % and 93 % was observed. LOD value of 0.34 ppb and 2.88 ppb (Figure S41, S42) were obtained.

We have also examined the possible detection of other nitro aromatics, such as 1,3-dinitro benzene (DNB), 2,4-dinitro toluene (DNT), nitro benzene (NB), and 4-nitro toluene (NT), by using the bpy containing compounds. For the Tb – bpy MOF, we observed a quenching efficiency of ~77% and ~52%, respectively, for the DNT and DNB molecules. Only marginal quenching of the luminescence intensity was noted for the NB and NT molecules (Figure S43 for Tb-bpy MOF).[118] Similar behaviour was noted in the case of Eu-bpy MOF as well (Figure S44).

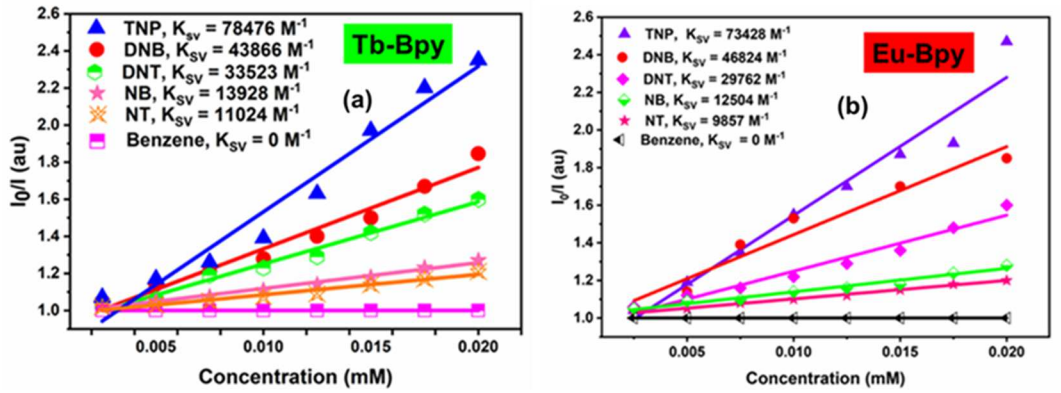

Figure 12. Plot of I_0/I of **(a)** Tb-bpy and **(b)** Eu-bpy MOFs (at 544 and 616 nm) *vs* concentration of trinitrophenol (TNP) (up to 100 μM).

The MOF compounds were found to be stable as well as recyclable during the nitroaromatics sensing (Figure S45a and S45b). The possible mechanism for the nitroaromatics detection by the present compounds is similar to those observed for the pesticide detection. We observed considerable overlap in the UV-Vis spectra of the host and the analyte (Figure S46a) suggesting competition between the compounds and the analyte (TNP) for the absorption of the photons. The overlap between the emission spectra of the MOF and the absorption spectra of the analyte indicates possible energy transfer that would result in the decrease of the luminescence intensity (Figure S46b). The IR spectroscopic investigations indicated a shift of 3 cm^{-1} in the -C≡C (Figure S47) and 7 cm^{-1} shift in the -C=N bands, which is suggestive of interactions between the MOF and the TNP. We observed the –NO stretching frequency at ~1550 cm^{-1}, which also suggests that the nitroaromatics and MOFs interact strongly (Figure S47). Similar observations have been made earlier.[119–122]

The detection of trinitrophenol (TNP) was also obtained with a paper strip coated with **4a,** Tb – bpy. The strips were dipped in 100 μM solution of the nitroaromatics and other phenol substituted derivatives and the green emission was affected only in the presence of TNP (Figure S48). We have also investigated the LOD of TNP by dipping the coated strips in TNP solution of varying concentrations (2.5 – 100 μM). The strips were dried and the change in the luminescence behaviour was examined (Figure 13a), revealing a gradual decrease in the luminescence intensity with increasing concentration of the TNP. The calculated LOD value was found to be 3.06 ppb, which is comparable to the value obtained for the detection in the solution state (0.97 ppb, Figure S49). We attempted paper strip-based sensing for **2a, 2b, 4b**, the other compounds, Eu-bpy, Tb-phen, Eu-phen: LOD values of 3.3 ppb, 2.42 ppb and 2.11 ppb, respectively, (Figure13b, S49 and S50) were obtained.

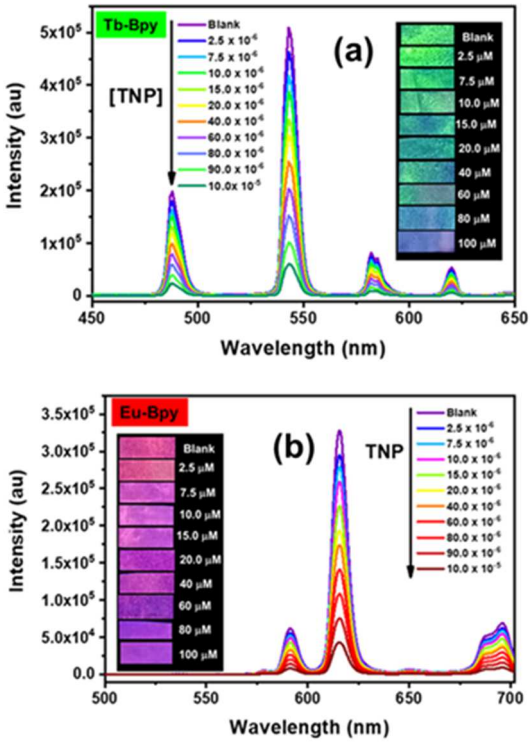

Figure 13. Paper – strip sensing of Trinitrophenol (TNP) using **(a)** Tb – bpy MOF and **(b)** Eu- bpy MOF (λ_{ex} = 350 nm). Inset shows the actual colour of the paper strips under UV-light.

Magnetic studies:

An interesting feature of these compounds is the binuclear [Ln2] unit, which acts as node of the extended coordination network. In this unit, the Ln(III) ions are bridged by the oxygen atoms of carboxylate groups (Figure 1a). Such an arrangement was document to possibly give rise to blocking of the magnetisation, i.e. Single Molecule Magnet behaviour, for lanthanide ions displaying magnetic anisotropy, such as Tb(III) and Dy(III).[123–125] Therefore, the magnetic behaviors for the Gd (**3a,b**), Tb (**4a,b**), and Dy (**5a,b**) derivatives were investigated. The temperature dependence of the magnetic susceptibility for **3b**, **4b**, and **5b** are plotted in the form of $\chi_M T$ versus T in Figure 14, where χ_M stands for the molar susceptibility relative to a $[(LnPhen)_2(BPTA)_3]$ moiety. The behaviours for the Bpy homologues (i.e. **3a**, **4a**, and **5a**) are very similar and can be found in SI (Figure S51). The values of $\chi_M T$ obtained at 300 K, 15.9 $cm^{-3}mol^{-1}K$ for **3b**, 22.6 for **4b**, and 27.4 for **5b**, are is good agreement with the expected paramagnetic contributions of two Ln ions, that is 15.76, 23.6, and 28.3 $cm^{-3}mol^{-1}K$ respectively for the Gd(III), Tb(III), and Dy(III).

For **3a**, the value for $\chi_M T$ remains unchanged as T is reduced to about 15 K, below which it falls sharply to 12.8 $cm^{-3}mol^{-1}K$ for 2 K. Such a behavior is suggesting a weak antiferromagnetic interaction between the Gd(III) centers. The field dependence of the magnetization at 2 K leads to a magnetization at saturation of 14.0 μ_B for 70 kOe (Figure S52). These behaviors were simultaneously modeled by a dimer model for two S = 7/2 centers, which yielded an exchange parameter of J = -0.03 cm^{-1} (based on $H = -J\mathbf{S}_{Gd1}\cdot\mathbf{S}_{Gd2}$) and g = 2.01. The $\chi_M T$ versus T behaviours for **4b** and **5b** are characterized by a constant decay as T decreases, which is the result of the crystal field effect applying for these ions. Below about 15 K, however, they show a marked difference. While for **5b** the decrease of $\chi_M T$ continues up to 17.4 $cm^3mol^{-1}K$ for 2 K, a slight rise is observed for **4b**. The latter reveals a ferromagnetic interaction that compensates the effect of the crystal field on the temperature dependence $\chi_M T$.[126] The absence of such a characteristic signature for **5b** does not exclude a ferromagnetic interaction between the Dy;

the expected increase in $\chi_M T$ may simply be smaller than the decrease induced by the crystal field effect.[127] This is supported by the comparison of the behaviour of **5b** with the behaviour obtained for Dy(III) diluted to about 8% in an Y(III) framework, i.e. $[(Y_{0.92}Dy_{0.08}Phen)_2(BPTA)_3]$. In the latter, the presence of $[Dy_2]$ units can be ruled out, so the magnetic behavior will be that of isolated Dy(III) ions. The subtraction of this intrinsic contribution of the Dy(III) from the behaviour of **5b** allows to qualitatively evidence the exchange contribution occurring for the bimetallic unit,[126,127] which is clearly ferromagnetic for $[Dy_2]$ (Figure S53). The same approach confirmed also the ferromagnetic interaction for the Tb derivative **4b** (Figure S54). The possibility for slow relaxation of the magnetisation for the Tb and Dy derivatives was evaluated by AC susceptibility studies (test frequency was 1 kHz). For all the derivative, no out of phase component of the magnetic susceptibility (χ_M'') was found in the absence of a DC field whereas the onset of an χ_M'' component appeared below 5 K when a field of 1 kOe was applied (Figure S54). But no maximum was visible above 2 K, therefore no further investigations were undertaken.

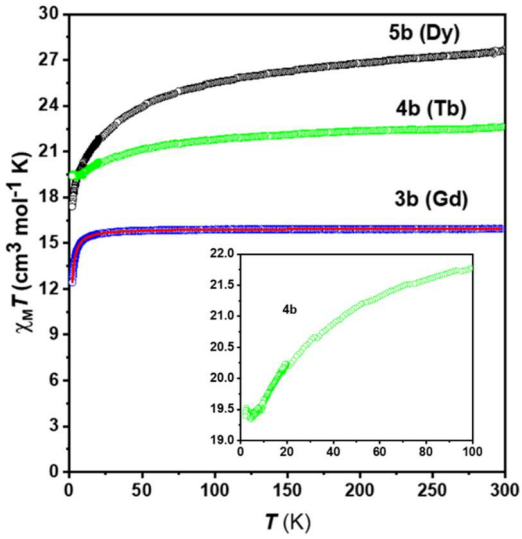

Figure 14. Experimental $\chi_M T$ versus T behaviors for **3b**, **4b**, **5b**, and (insert) low temperature behavior for the Tb derivative. The full line is the calculated behavior for the Gd compound (see text for parameters).

Conclusions

Two dimensional lanthanide compounds, $[Ln(BPTA)_{1.5}(bpy)]\cdot 0.5DMF$; Ln = Y, Eu, Gd, Tb, Dy (**1a-5a**) and $[Ln(BPTA)_{1.5}(phen)]\cdot 0.5DMF$; Ln = Y, Eu, Gd, Tb, Dy (**1b-5b**) with 2,5-bis(prop-2-yn-1-yloxy)terephthalic acid (2, 5 – BPTA) as a primary ligand and 2, 2' bipyridine and 1, 10 phenanthroline as the secondary ligand has been prepared and their structures determined by single crystal X-ray studies. The use of larger 1, 10 phenanthroline secondary ligands results in the lanthanides to have a tricapped trigonal prismatic geometry compared to mono – capped square antiprismatic geometry for the 2, 2' bipyridine ligands. The rigid secondary ligands act to produce good antenna effect that results in intense characteristic emissions from the rare- earth metal centres. The Y – compounds exhibit good blue emission and along with the Eu (red) and Tb (green) substitutions gave rise to white emission. The compounds, $(Y_{0.96}Tb_{0.02}Eu_{0.02})$ – bpy and $(Y_{0.939}Tb_{0.06}Eu_{0.001})$ – phen exhibit white emission with 31 % and 43 % quantum yield (QY). The intense rare earth emission along with good QY was exploited for sensing of pesticides and nitroaromatics. Paper – strip-based detectors have been prepared and established to be efficient in the detection of azinphos-methyl (pesticide) and trinitrophenol (explosive) with good selectivity and sensitivity (ppb) levels. The present study highlights the many different aspects of rare-

earth based compounds and their fluorescence-based utilities towards detection of harmful substances in the environment.

Acknowledgements

SN thanks to Science and Engineering research Board, (SERB) Govt. of India for the award of JC Bose national fellowship. SN and KM thanks CSIR, Government of India, for the award of a research grant and a research fellowship. JPS is grateful to the Infosys Foundation for the position of Visiting Professor at the Indian Institute of Science (2020-2023). The authors are thankful to Dr. Muniratinam Nethaji (IPC), Mr. Apurba Kumar Pal (IPC) Mr Dinesh Chakravarthy Senthurpandi (IPC) and Dr. Sourav Roy (SSCU) for their help in modelling the disorder in the single crystal. Authors also thank Prof. P. Thilagar and Muhammed Munthasir A T (IPC) Indian Institute of Science, for the lifetime measurements and to Dr. L.-M. Lacroix and Mrs G. Ballon (INSA, Toulouse) for recording the magnetic data.

References

1 H. Furukawa, K. E. Cordova, M. O'Keeffe and O. M. Yaghi, *Science (80-.).*, 2013, **341**, 1230444.
2 S. Riedel and M. Kaupp, *Coord. Chem. Rev.*, 2009, **253**, 606–624.
3 I. Strauss, A. Mundstock, D. Hinrichs, R. Himstedt, A. Knebel, C. Reinhardt, D. Dorfs and J. Caro, *Angew. Chemie Int. Ed.*, 2018, **57**, 7434–7439.
4 C. K. Brozek and M. Dincă, *Chem. Sci.*, 2012, **3**, 2110–2113.
5 T. Liao, L. Kou, A. Du, Y. Gu and Z. Sun, *J. Am. Chem. Soc.*, 2018, **140**, 9159–9166.
6 S. Li, Y. Gao, N. Li, L. Ge, X. Bu and P. Feng, *Energy Environ. Sci.*, 2021, **14**, 1897–1927.
7 *Chem. Rev.*, 2012, **112**, 673–674.
8 S. Natarajan and P. Mahata, *Chem. Soc. Rev.*, 2009, **38**, 2304–2318.
9 S. Natarajan and K. Manna, *ACS Org. Inorg. Au*, , DOI:10.1021/acsorginorgau.3c00033.
10 J.-C. G. Bünzli, *J. Coord. Chem.*, 2014, **67**, 3706–3733.
11 J. Rocha, L. D. Carlos, F. A. A. Paz and D. Ananias, *Chem. Soc. Rev.*, 2011, **40**, 926–940.
12 S. Sahoo, S. Mondal and D. Sarma, *Coord. Chem. Rev.*, 2022, **470**, 214707.
13 P. Mahata and S. Natarajan, *Inorg. Chem.*, 2007, **46**, 1250–1258.
14 P. Mahata, G. Madras and S. Natarajan, *J. Phys. Chem. B*, 2006, **110**, 13759–13768.
15 W. Huang, F. Pan, Y. Liu, S. Huang, Y. Li, J. Yong, Y. Li, A. M. Kirillov and D. Wu, *Inorg. Chem.*, 2017, **56**, 6362–6370.
16 G. Ji, J. Liu, X. Gao, W. Sun, J. Wang, S. Zhao and Z. Liu, *J. Mater. Chem. A*, 2017, **5**, 10200–10205.
17 K. A. White, D. A. Chengelis, K. A. Gogick, J. Stehman, N. L. Rosi and S. Petoud, *J. Am. Chem. Soc.*, 2009, **131**, 18069–18071.
18 G. Blasse and B. C. Grabmaier, in *Luminescent Materials*, eds. G. Blasse and B. C. Grabmaier, Springer Berlin Heidelberg, Berlin, Heidelberg, 1994, pp. 1–9.
19 A. R. Ramya, D. Sharma, S. Natarajan and M. L. P. Reddy, *Inorg. Chem.*, 2012, **51**, 8818–8826.
20 W. T. Carnall, P. R. Fields and B. G. Wybourne, *J. Chem. Phys.*, 2004, **42**, 3797–3806.
21 D. Markovitsi, T.-H. Tran-Thi, R. Even and J. Simon, *Chem. Phys. Lett.*, 1987, **137**, 107–112.
22 P. Di Bernardo, G. R. Choppin, R. Portanova and P. L. Zanonato, *Inorganica Chim. Acta*, 1993, **207**, 85–91.
23 C. V. Banks, M. R. Heusinkveld and J. W. O'laughlin, *Anal. Chem.*, 1961, **33**, 1235–1240.
24 Y. Lu and B. Yan, *Chem. Commun.*, 2014, **50**, 15443–15446.
25 X.-Z. Xie, Y.-R. Zhang, Y.-J. Wu, X.-B. Yin and Y. Xia, *J. Phys. Chem. C*.
26 J. Wu, H. Zhang and S. Du, *J. Mater. Chem. C*, 2016, **4**, 3364–3374.
27 T. Gorai, W. Schmitt and T. Gunnlaugsson, *Dalt. Trans.*, 2021, **50**, 770–784.
28 Y. Cui, B. Chen and G. Qian, *Coord. Chem. Rev.*, 2014, **273–274**, 76–86.
29 B. Yan, *Acc. Chem. Res.*, 2017, **50**, 2789–2798.
30 Y. Zhao and D. Li, *J. Mater. Chem. C*, 2020, **8**, 12739–12754.
31 M. D. Allendorf, C. A. Bauer, R. K. Bhakta and R. J. T. Houk, *Chem. Soc. Rev.*, 2009, **38**, 1330–1352.
32 S. Zhao, J. Xiao, T. Zheng, M. Liu, H. Wu and Z. Liu, *ACS Omega*, 2019, **4**, 16378–16384.
33 K. Wu, X.-Y. Liu, Y.-L. Huang, M. Xie, X. Xiong, J. Zheng, W. Lu and D. Li, *Inorg. Chem. Front.*, 2022, **9**, 1714–1721.
34 K.-M. Ge, D. Wang, Z.-J. Xu and R.-Q. Chu, *J. Mol. Struct.*, 2020, **1208**, 127862.
35 G. Accorsi, A. Listorti, K. Yoosaf and N. Armaroli, *Chem. Soc. Rev.*, 2009, **38**, 1690–1700.
36 K. Zheng, Z.-Q. Liu, Y. Huang, F. Chen, C.-H. Zeng, S. Zhong and S. W. Ng, *Sensors Actuators B Chem.*, 2018, **257**, 705–713.
37 J.-Z. Gu, Y.-H. Cui, J. Wu and A. M. Kirillov, *RSC Adv.*, 2015, **5**, 78889–78901.
38 J. Liu, W. Zuo, W. Zhang, J. Liu, Z. Wang, Z. Yang and B. Wang, *Nanoscale*, 2014, **6**, 11473–11478.
39 B. Chen, Y. Yang, F. Zapata, G. Lin, G. Qian and E. B. Lobkovsky, *Adv. Mater.*, 2007, **19**, 1693–1696.
40 M. Chen, W.-M. Xu, J.-Y. Tian, H. Cui, J.-X. Zhang, C.-S. Liu and M. Du, *J. Mater. Chem. C*, 2017, **5**, 2015–2021.
41 C. N. Pope, *J. Toxicol. Environ. Heal. Part B*, 1999, **2**, 161–181.
42 B. E. Mileson, J. E. Chambers, W. L. Chen, W. Dettbarn, M. Ehrich, A. T. Eldefrawi, D. W. Gaylor, K. Hamernik, E. Hodgson, A. G. Karczmar, S. Padilla, C. N. Pope, R. J. Richardson, D. R. Saunders, L. P. Sheets, L. G. Sultatos and K. B. Wallace, *Toxicol. Sci.*, 1998, **41**, 8–20.
43 D. K. Singha, P. Majee, S. K. Mondal and P. Mahata, *ChemistrySelect*, 2017, **2**, 5760–5768.
44 D. K. Singha, P. Majee, S. Mandal, S. K. Mondal and P. Mahata, *Inorg. Chem.*, 2018, **57**, 12155–12165.

45 L. D. Rosales-Vázquez, A. Dorazco-González and V. Sánchez-Mendieta, *Dalt. Trans.*, 2021, **50**, 4470–4485.
46 T. Kundu, K. Manna, A. K. Jana and S. Natarajan, *New J. Chem.*, 2019, **43**, 13263–13270.
47 L. Yang, Y.-L. Liu, C.-G. Liu, F. Ye and Y. Fu, *Inorg. Chem. Commun.*, 2020, **122**, 108272.
48 J. Tiwari, P. Tarale, S. Sivanesan and A. Bafana, *Environ. Sci. Pollut. Res.*, 2019, **26**, 28650–28667.
49 O. Abuzalat, D. Wong, S. S. Park and S. Kim, *Nanoscale*, 2020, **12**, 13523–13530.
50 J. C. Sanchez, S. J. Toal, Z. Wang, R. E. Dugan and W. C. Trogler, *J. Forensic Sci.*, 2007, **52**, 1308–1313.
51 Z.-Q. Shi, N.-N. Ji and H.-L. Hu, *Dalt. Trans.*, 2020, **49**, 12929–12939.
52 P. Ghosh, S. K. Saha, A. Roychowdhury and P. Banerjee, *Eur. J. Inorg. Chem.*, 2015, **2015**, 2851–2857.
53 S. S. Nagarkar, A. V Desai and S. K. Ghosh, *Chem. Commun.*, 2014, **50**, 8915–8918.
54 K. Manna, J.-P. Sutter and S. Natarajan, *Inorg. Chem.*, , DOI:10.1021/acs.inorgchem.2c02611.
55 O. Kahn, *Inc. New York, NY, USA*, 1993, 393.
56 N. F. Chilton, R. P. Anderson, L. D. Turner, A. Soncini and K. S. Murray, *J. Comput. Chem.*, 2013, **34**, 1164–1175.
57 G. Sheldrick, *Acta Crystallogr. Sect. C*, 2015, **71**, 3–8.
58 O. V Dolomanov, L. J. Bourhis, R. J. Gildea, J. A. K. Howard and H. Puschmann, *J. Appl. Crystallogr.*, 2009, **42**, 339–341.
59 P. Müller, *Crystallogr. Rev.*, 2009, **15**, 57–83.
60 K. Manna, B. Suresh Kumar, T. Maity and S. Natarajan, *ChemNanoMat*, 2022, **8**, e202200081.
61 K. Manna, R. Kumar, A. Sundaresan and S. Natarajan, *Inorg. Chem.*, 2023, **62**, 13738–13756.
62 J. Georges, *Analyst*, 1993, **118**, 1481–1486.
63 B. Alpha, R. Ballardini, V. Balzani, J.-M. Lehn, S. Perathoner and N. Sabbatini, *Photochem. Photobiol.*, 1990, **52**, 299–306.
64 H.-Q. Yin, X.-Y. Wang and X.-B. Yin, *J. Am. Chem. Soc.*, 2019, **141**, 15166–15173.
65 J. M. Stanley and B. J. Holliday, *Coord. Chem. Rev.*, 2012, **256**, 1520–1530.
66 J. Feng and H. Zhang, *Chem. Soc. Rev.*, 2013, **42**, 387–410.
67 J. González, P. Sevilla, G. Gabarró-Riera, J. Jover, J. Echeverría, S. Fuertes, A. Arauzo, E. Bartolomé, E. C. Sañudo, Q. Zhang, J. Wang, A. M. Kirillov, W. Dou, C. C. Xu, C. C. Xu, L. Yang, R. Fang and W. Liu, *ACS Appl. Mater. Interfaces*, 2021, **10**, 23976–23986.
68 J. González, P. Sevilla, G. Gabarró-Riera, J. Jover, J. Echeverría, S. Fuertes, A. Arauzo, E. Bartolomé and E. C. Sañudo, *Angew. Chemie - Int. Ed.*, 2021, **60**, 12001–12006.
69 A. P. Penner, W. Siebrand and M. Z. Zgierski, *J. Chem. Phys.*, 1978, **69**, 5496–5508.
70 G. E. Buono-core, H. Li and B. Marciniak, *Coord. Chem. Rev.*, 1990, **99**, 55–87.
71 A. D'Aléo, A. Picot, A. Beeby, J. A. Gareth Williams, B. Le Guennic, C. Andraud and O. Maury, *Inorg. Chem.*, 2008, **47**, 10258–10268.
72 P. Ramaswamy, S. Mandal, N. N. Hegde, R. Prabhu, D. Banerjee, S. V Bhat and S. Natarajan, *Eur. J. Inorg. Chem.*, 2010, **2010**, 1829–1838.
73 N. E. Borisova, T. B. Sumyanova, A. V Kharcheva, P. I. Matveev, A. V Ivanov, E. A. Razumova and S. V Patsaeva, *Dalt. Trans.*, 2018, **47**, 16755–16765.
74 L. J. Charbonnière, R. Ziessel, M. Montalti, L. Prodi, N. Zaccheroni, C. Boehme and G. Wipff, *J. Am. Chem. Soc.*, 2002, **124**, 7779–7788.
75 V. Bekiari, G. Pistolis and P. Lianos, *Chem. Mater.*, 1999, **11**, 3189–3195.
76 P. G. Sammes and G. Yahioglu, *Chem. Soc. Rev.*, 1994, **23**, 327–334.
77 Y. Jing-he, Z. Gui-yun and W. Bo, *Anal. Chim. Acta*, 1987, **198**, 287–292.
78 W.-J. Chai, W.-X. Li, X.-J. Sun, T. Ren and X.-Y. Shi, *J. Lumin.*, 2011, **131**, 225–230.
79 Q.-Y. Yang, K. Wu, J.-J. Jiang, C.-W. Hsu, M. Pan, J.-M. Lehn and C.-Y. Su, *Chem. Commun.*, 2014, **50**, 7702–7704.
80 A. Bhim, A. Mohanty and S. Natarajan, *Dalt. Trans.*, 2020, **49**, 17649–17657.
81 G.-W. Xu, Y.-P. Wu, W.-W. Dong, J. Zhao, X.-Q. Wu, D.-S. Li and Q. Zhang, *Small*, 2017, **13**, 1602996.
82 D. Zhao, D. Yue, L. Zhang, K. Jiang and G. Qian, *Inorg. Chem.*, 2018, **57**, 12596–12602.
83 T. Li, P. Li, Z. Wang, S. Xu, Q. Bai and Z. Yang, *Dalt. Trans.*, 2015, **44**, 16840–16846.
84 Z. V Dobrokhotova, S. P. Petrosyants, A. B. Ilyukhin, Y. S. Zavorotny, V. I. Gerasimova, Y. A. Mikhlina, N. N. Efimov and V. M. Novotortsev, *Inorganica Chim. Acta*, 2017, **456**, 76–85.
85 A. M. Kłonkowski, S. Lis, Z. Hnatejko, K. Czarnobaj, M. Pietraszkiewicz and M. Elbanowski, *J. Alloys Compd.*, 2000, **300**–**301**, 55–60.
86 A. De, S. Bala, S. Saha, K. S. Das, S. Akhtar, A. Adhikary, A. Ghosh, G.-Z. Huang, S. P. Chowdhuri, B. B. Das, M.-L. Tong and R. Mondal, *Dalt. Trans.*, 2021, **50**, 3593–3609.

87 M. R. Silva, P. Martín-Ramos, J. T. Coutinho, L. C. J. Pereira and J. Martín-Gil, *Dalt. Trans.*, 2014, **43**, 6752–6761.
88 H.-B. Xu, L.-X. Shi, E. Ma, L.-Y. Zhang, Q.-H. Wei and Z.-N. Chen, *Chem. Commun.*, 2006, **15**, 1601–1603.
89 A. Thirumurugan and S. Natarajan, *Eur. J. Inorg. Chem.*, 2004, **2004**, 762–770.
90 A. Thirumurugan and S. Natarajan, *Dalt. Trans.*, 2004, 2923–2928.
91 D. Sarma, M. Prabu, S. Biju, M. L. P. Reddy and S. Natarajan, *Eur. J. Inorg. Chem.*, 2010, **2010**, 3813–3822.
92 S. Zou, Q. Li and S. Du, *RSC Adv.*, 2015, **5**, 34936–34941.
93 C.-Y. Sun, X.-L. Wang, X. Zhang, C. Qin, P. Li, Z.-M. Su, D.-X. Zhu, G.-G. Shan, K.-Z. Shao, H. Wu and J. Li, *Nat. Commun.*, 2013, **4**, 2717.
94 C. de Mello Donegá, S. A. Junior and G. F. de Sá, *J. Alloys Compd.*, 1997, **250**, 422–426.
95 Y. Wen, T. Sheng, X. Zhu, C. Zhuo, S. Su, H. Li, S. Hu, Q.-L. Zhu and X. Wu, *Adv. Mater.*, 2017, **29**, 1700778.
96 T. Song, G. Zhang, Y. Cui, Y. Yang and G. Qian, *CrystEngComm*, 2016, **18**, 8366–8371.
97 H. Cai, L.-L. Xu, H.-Y. Lai, J.-Y. Liu, S. W. Ng and D. Li, *Chem. Commun.*, 2017, **53**, 7917–7920.
98 D.-D. Xu, W.-W. Dong, M.-K. Li, H.-M. Han, J. Zhao, D.-S. Li and Q. Zhang, *Inorg. Chem.*, 2022, **61**, 21107–21114.
99 Y.-P. Xia, C.-X. Wang, L.-C. An, D.-S. Zhang, T.-L. Hu, J. Xu, Z. Chang and X.-H. Bu, *Inorg. Chem. Front.*, 2018, **5**, 2868–2874.
100 Q. Gong, Z. Hu, B. J. Deibert, T. J. Emge, S. J. Teat, D. Banerjee, B. Mussman, N. D. Rudd and J. Li, *J. Am. Chem. Soc.*, 2014, **136**, 16724–16727.
101 L.-L. Ma, G.-P. Yang, G.-P. Li, P.-F. Zhang, J. Jin, Y. Wang, J.-M. Wang and Y.-Y. Wang, *Inorg. Chem. Front.*, 2021, **8**, 329–338.
102 X.-Y. Li, W.-J. Shi, X.-Q. Wang, L.-N. Ma, L. Hou and Y.-Y. Wang, *Cryst. Growth Des.*, 2017, **17**, 4217–4224.
103 P. Hanninen and ¨nninen ? Harri Ha ¨rma, *Lanthanide Luminescence, Photophysical, Analytical and Biological Aspects*, 2011, vol. 7.
104 K. Manna and S. Natarajan, *Inorg. Chem.*, 2023, **62**, 508–519.
105 Y. Yang, L. Zhao, M. Sun, P. Wei, G. Li and Y. Li, *Dye. Pigment.*, 2020, **180**, 108444.
106 L. Xu, Y. Xu, X. Li, Z. Wang, T. Sun and X. Zhang, *Dalt. Trans.*, 2018, **47**, 16696–16703.
107 X. Zhang, Z. Zhan, X. Liang, C. Chen, X. Liu, Y. Jia and M. Hu, *Dalt. Trans.*, 2018, **47**, 3272–3282.
108 Y. Du, H. Yang, R. Liu, C. Shao and L. Yang, *Dalt. Trans.*, 2020, **49**, 13003–13016.
109 A.-N. Dou, L.-B. Yang, X.-D. Fang, Q. Yin, M.-D. Li, J. Li, M.-Y. Wang, A.-X. Zhu and Q.-Q. Xu, *CrystEngComm*, 2018, **20**, 3609–3619.
110 S. Wang, B. Sun, Z. Su, G. Hong, X. Li, Y. Liu, Q. Pan and J. Sun, *Inorg. Chem. Front.*, 2022, **9**, 3259–3266.
111 O. V Angelsky, A. Y. Bekshaev, M. V Vasnetsov, C. Y. Zenkova, P. P. Maksimyak and J. Zheng, *Front. Phys.*, 2022, **10**, 1168.
112 D. K. Singha, P. Majee, S. K. Mondal and P. Mahata, *Polyhedron*, 2019, **158**, 277–282.
113 J. Tang, X. Ma, J. Yang, D.-D. Feng and X.-Q. Wang, *Dalt. Trans.*, 2020, **49**, 14361–14372.
114 A. Afzalinia and M. Mirzaee, *ACS Appl. Mater. Interfaces*, 2020, **12**, 16076–16087.
115 Z. Hu, S. Pramanik, K. Tan, C. Zheng, W. Liu, X. Zhang, Y. J. Chabal and J. Li, *Cryst. Growth Des.*, 2013, **13**, 4204–4207.
116 C. Li, J. Huang, H. Zhu, L. Liu, Y. Feng, G. Hu and X. Yu, *Sensors Actuators B Chem.*, 2017, **253**, 275–282.
117 J.-S. Hu, S.-J. Dong, K. Wu, X.-L. Zhang, J. Jiang, J. Yuan and M.-D. Zheng, *Sensors Actuators B Chem.*, 2019, **283**, 255–261.
118 D. K. Singha, S. Bhattacharya, P. Majee, S. K. Mondal, M. Kumar and P. Mahata, *J. Mater. Chem. A*, 2014, **2**, 20908–20915.
119 S. Jensen, K. Tan, W. Lustig, D. Kilin, J. Li, Y. J. Chabal and T. Thonhauser, *J. Mater. Chem. C*, 2019, **7**, 2625–2632.
120 S. Content, W. C. Trogler and M. J. Sailor, *Chem. – A Eur. J.*, 2000, **6**, 2205–2213.
121 T. Kundu, A. K. Jana and S. Natarajan, *Cryst. Growth Des.*, 2014, **14**, 4531–4544.
122 T. Wang, Y. Jia, Q. Chen, R. Feng, S. Tian, T.-L. Hu and X.-H. Bu, *Sci. China Chem.*, 2016, **59**, 959–964.
123 F. Habib and M. Murugesu, *Chem. Soc. Rev.*, 2013, **42**, 3278–3288.
124 H.-R. Tu, W.-B. Sun, H.-F. Li, P. Chen, Y.-M. Tian, W.-Y. Zhang, Y.-Q. Zhang and P.-F. Yan, *Inorg. Chem. Front.*, 2017, **4**, 499–508.
125 M. J. Giansiracusa, S. Al-Badran, A. K. Kostopoulos, G. F. S. Whitehead, E. J. L. McInnes, D. Collison, R. E. P. Winpenny and N. F. Chilton, *Inorg. Chem. Front.*, 2020, **7**, 3909–3918.
126 M. L. Kahn, J.-P. Sutter, S. Golhen, P. Guionneau, L. Ouahab, O. Kahn and D. Chasseau, *J. Am. Chem. Soc.*, 2000, **122**, 3413–3421.
127 J. Sutter, M. L. Kahn and O. Kahn, *Adv. Mater.*, 1999, **11**, 863–865.

SUPPORTING INFORMATION

Materials

The chemicals required for the synthesis of the compounds: $La(NO_3)_3.xH_2O$ (Ln= Y, Eu, Gd, Tb, Dy) propargyl bromide (80 wt% in toluene, 0.3% magnesium oxide as stabilizer) (Sigma-Aldrich); the compounds for the catalytic studies and 2, 5-dihyroxyterephthalic acid (TCI); THF, DMF, EtOH, KOH, MeOH, HCl (SDfine, India). The organophosphorus pesticides and nitroaromatics (Sigma) were used as purchased without any purifications. The water used was double distilled through a Millipore membrane. All the chemicals were used as purchased without any further purifications.

Synthetic procedure of the Ligand and MOF Compounds

The primary ligand, 2,5-bis(prop-2-yn-1-yloxy) terephthalic acid (2, 5 BPTA) was prepared by employing a known procedure.[1]

All the compounds were prepared by the sequential layering of three different solutions. The lanthanide nitrates, $Ln(NO_3)_3 \cdot xH_2O$, (0.05 mmol , ~0.020 g) was dissolved in 1 mL water (Solution **A**). Buffer solution (1 mL) was prepared by mixing 1:1 H_2O and DMF (Solution **B**). 2, 2′ Bipyridine (0.05 mmol, 0.008 g, compound **1a-5a**) or 1, 10 phenanthroline (0.05 mmol, 0.009 g, compound **1b-5b**) was dissolved in the buffer solution. The ligand 2,5-BPTA (0.05 mmol, 0.013 g) was dissolved in 1 mL of N, N-DMF (Solution **C**). In a Teflon-capped reaction vessel, solution **A** (1 mL) containing the lanthanide salt was added at the bottom. Then, 1 mL of solution **B** was carefully layered on the top of solution **A** followed by the addition of 1 mL of solution **C**. The reaction vessel was closed with a cap, and kept undisturbed in an oven at 75 ºC for 3-7 days. In the case of 2, 2′ bipyridine, large amount of cubic block shaped colourless crystals were isolated after 7 days. In case of 1, 10 phenanthroline, products with similar morphology came after 3 days. The yield in all cases was found to be in the range of ~60 - 70 % with respect to the lanthanide ions. Elemental analysis for all the compounds is listed in Table S1. Powder X-ray diffraction (PXRD) studies (Figure S1) has confirmed the phase purity of the prepared samples. The mixed metal compounds were also prepared employing a similar procedure (Figure S2, S3).

Table S1A. Synthesis of compound 1-5 in layering method

Compound	Layer A	Layer B	Layer C	Temp (°C)	Time (days)	Shape and colour of crystal
Compounds 1a-5a	$Ln(NO_3)_3 \cdot xH_2O$ salt (0.020 g, 0.05 mmol) in 1 mL of water	2, 2'-bipyridine (0.008 g, 0.05 mmol) dissolved in the 1 mL buffer solution of DMF and water	2,5 BPTA (0.013 g, 0.05 mmol) in 1 mL of DMF	**75**	**7**	Colourless, cubic
Compounds 1b-5b	$Ln(NO_3)_3 \cdot xH_2O$ salt (0.020 g, 0.05 mmol) in 1 mL of water	1, 10 phenanthroline, (0.009 g, 0.05 mmol) in the 1 mL buffer solution of DMF and water	2,5 BPTA (0.013 g, 0.05 mmol) in 1 mL of DMF	**75**	**3**	Colourless, cubic

Table S1B Elemental Analysis of Compound **1-5 (a, b)**

Compound	%C		%H		%N		%O	
	As Synthesized	Calc.	As Synthesized	Calc.	As Synthesized	Calc.	As Synthesized	Calc.
Compound **1a**	55.34	55.46	3.12	3.3	4.35	4.17	23.07	23.83
Compound **2a**	49.87	50.69	2.93	3.02	4.01	3.81	21.95	21.78
Compound **3a**	50.19	50.33	2.86	3.00	3.85	3.79	21.41	21.63
Compound **4a**	50.13	50.22	2.53	2.99	4.01	3.78	21.55	21.58
Compound **5a**	49.34	49.98	2.71	2.98	3.9	3.76	21.6	21.47
Compound **1b**	56.84	56.99	2.99	3.19	4.1	4.03	23.41	23.01
Compound **2b**	52.71	52.26	2.59	2.92	3.81	3.69	20.71	21.09
Compound **3b**	52.06	51.89	2.53	2.9	3.86	3.67	20.69	20.95
Compound **4b**	52.09	51.78	2.78	2.9	3.76	3.66	20.21	20.91
Compound **5b**	51.76	51.54	2.5	2.88	3.66	3.64	20.85	20.80

Table S2a Selected bond lengths (Å) and bond angles (deg) for **3a,** Gd containing 2, 2'-bipyridine MOF.

Compound **3a**			
Bond length(Å)		**Bond angle (°)**	
Gd1-O1_4	2.36(4)	O1_4-Gd1-O1_5	76.71(15)
Gd1-O1_5	2.36(4)	O1_4-Gd1-N1_2	147.89(17)
Gd1-N1_2	2.54(5)	O1_4-Gd1-N1'_2	147.89(17)
Gd1-N1'_2	2.57(4)	O1_3_a-Gd1-O1_4	90.66(13)
Gd1-O1_3_a	2.49(3)	O2_3_a-Gd1-O1_4	90.66(13)
Gd1-O2_3_a	2.40(4)	O1_4-Gd1-O1_4_b	72.88(12)
Gd1-O1_4_b	2.58(3)	O1_4-Gd1-O2_4_b	122.86(14)
Gd1-O2_4_b	2.49(5)	O1_4-Gd1-O2_5_b	72.44(14)
Gd1-O2_5_b	2.38(5)	O1_5-Gd1-N1_2	80.24(16)
		O1_5-Gd1-N1'_2	134.47(16)
		O1_3_a-Gd1-O1_5	75.32(15)
		O2_3_a-Gd1-O1_5	128.41(14)
		O1_4_b-Gd1-O1_5	68.85(14)
		O2_4_b-Gd1-O1_5	79.37(19)
		O1_5-Gd1-O2_5_b	136.34(14)
		N1_2-Gd1-N1'_2	63.00(18)
		O1_3_a-Gd1-N1_2	73.29(15)
		O2_3_a-Gd1-N1_2	83.45(16)
		O1_4_b-Gd1-N1_2	121.89(16)
		O2_4_b-Gd1-N1_2	77.24(18)
		O2_5_b-Gd1-N1_2	139.85(15)
		O1_3_a-Gd1-N1'_2	114.87(15)
		O2_3_a-Gd1-N1'_2	75.32(15)
		O1_4_b-Gd1-N1'_2	107.70(15)
		O2_4_b-Gd1-N1'_2	67.56(18)
		O2_5_b-Gd1-N1'_2	77.09(15)
		O1_3_a-Gd1-O2_3_a	53.12(14)
		O1_3_a-Gd1-O1_4_b	136.56(12)
		O1_3_a-Gd1-O2_4_b	143.77(19)
		O1_3_a-Gd1-O2_5_b	124.03(15)
		O2_3_a-Gd1-O1_4_b	153.50(14)
		O2_3_a-Gd1-O2_4_b	142.74(16)
		O2_3_a-Gd1-O2_5_b	82.41(15)
		O1_4_b-Gd1-O2_4_b	50.12(14)
		O1_4_b-Gd1-O2_5_b	72.98(15)
		O2_4_b-Gd1-O2_5_b	92.2(2)

a = 1-x, 1-y, 1-z
b = 1-x, 2-y, 1-z

Table S2b Selected bond lengths (Å) and bond angles (deg) for **5b,** Dy containing 1,10-phenanthroline MOF

Compound **5b**			
Bond length(Å)		**Bond angle (°)**	
Dy1-O1_3	2.34(5)	O1_3-Dy1-O1_4	72.44(15)
Dy1-O1_4	2.36(4)	O1_3-Dy1-N1_2	82.16(16)
Dy1-N1_2	2.50(6)	O1_3-Dy1-N10_2	131.72(16)
Dy1-N10_2	2.54(5)	O1_3-Dy1-O2_3_b	139.57(13)
Dy1-O2_3_b	2.38(4)	O1_3-Dy1-O1_4_b	77.95(14)
Dy1-O1_4_b	2.45(3)	O1_3-Dy1-O2_4_b	68.56(15)
Dy1-O2_4_b	2.57(5)	O1_3-Dy1-O1_5_c	131.09(13)
Dy1-O1_5_c	2.38(4)	O1_3-Dy1-O2_5_c	77.20(13)
Dy1-O2_5_c	2.43(3)	O1_4-Dy1-N1_2	147.39(16)
		O1_4-Dy1-N10_2	147.33(16)
		O2_3_b-Dy1-O1_4	72.47(14)
		O1_4-Dy1-O1_4_b	74.47(12)
		O1_4-Dy1-O2_4_b	117.74(14)
		O1_4-Dy1-O1_5_c	99.85(13)
		O1_4-Dy1-O2_5_c	79.59(12)
		N1_2-Dy1-N10_2	65.24(17)
		O2_3_b-Dy1-N1_2	137.42(16)
		O1_4_b-Dy1-N1_2	120.29(15)
		O2_4_b-Dy1-N1_2	68.80(15)
		O1_5_c-Dy1-N1_2	81.52(15)
		O2_5_c-Dy1-N1_2	75.03(14)
		O2_3_b-Dy1-N10_2	76.12(16)
		O1_4_b-Dy1-N10_2	88.51(13)
		O2_4_b-Dy1-N10_2	66.90(17)
		O1_5_c-Dy1-N10_2	79.99(14)
		O2_5_c-Dy1-N10_2	122.78(13)
		O2_3_b-Dy1-O1_4_b	73.87(14)
		O2_3_b-Dy1-O2_4_b	112.28(14)
		O2_3_b-Dy1-O1_5_c	74.58(14)
		O2_3_b-Dy1-O2_5_c	115.08(14)
		O1_4_b-Dy1-O2_4_b	51.51(14)
		O1_4_b-Dy1-O1_5_c	148.18(15)
		O1_4_b-Dy1-O2_5_c	148.38(13)
		O2_4_b-Dy1-O2_5_c	142.28(14)
		O1_5_c-Dy1-O2_5_c	132.58(16)

b = 1-x, 1-y, 1-z
c = 1-x, 2-y, 1-z

Table S4 Hydrogen bonding for **3a** compound

D-H···A (Å)	d(D-H) (Å)	d(H-A) (Å)	d(D···A) (Å)	∠DHA (°)	Symmetry transforms
Compound **3a**					
C3'_2–H3'_2···O1_6	0.95	2.57	3.49(9)	165.00	x,y,1+z
C2_6–H2A_6···O1_8	0.99	2.44	3.42(6)	170.00	1-x,1-y,1-z
C2_6–H2A_6···O1_7	0.99	2.56	3.52(6)	165.00	1-x,1-y,1-z
C4_6–H4_6···O1_1	0.95	2.10	3.04(19)	170.00	1+x,y,z
C4_9–H4_9···O1_1	0.95	2.19	3.09(2)	157.00	1-x,2-y,-z

Table S5. List of important IR bands observed in **1-5(a, b)**

Compound	ν(≡C–H) (cm^{-1})	ν(C≡C) (cm^{-1})	ν(COO) acid (cm^{-1})	ν(C=C) (cm^{-1})	ν(C=N) (cm^{-1})	$\nu(O–H)_{str}$ non coordinated H_2O (cm^{-1})	ν(C-H) Aromatic
2,5 BPTA	~3261	~2126	~1693		-	-	
Compound **1a-5a**	~3243	~2117	~1657	~1584	~1528	~3640	~3060
Compound **1b-5b**	~3309	~2127	~1670	~1610	~1539	~3400-3300-	~3065
2, 2' Bipyridine	-	-	-	~1578	~1557	-	~3052
1, 10 phenanthroline	-	-	-	~1644	~1586	~3363	~3056

The IR spectra of the ligand, 2, 5 BPTA, (Figure S5a) exhibits a sharp band at 3261 cm^{-1}, which can be assigned to the stretching of the alkyne ≡C–H group. The band at 2126 cm^{-1} corresponds to the C≡C stretching. A broad band in the 3000-2780 cm^{-1} corresponds to the aromatic C–H stretching from the benzene ring and the stretching of the methylene group. The IR spectra of 2, 2' - bipyridine and 1, 10 – phenanthroline shows aromatic stretching bands at 3052 and 3056 cm^{-1}. The typical C=C and C=N frequency appears at 1584 and 1528 cm^{-1} for bipyridine and 1610, 1539 cm^{-1} for phenanthroline. For the compound **1a-5a**, a sharp peak at ~3640 cm^{-1} corresponds to the stretching frequency of the lattice water molecule. Also, the C=N stretching frequency appears to be red shifted to 1528 cm^{-1} for the electron donation from N to the metal centres. For compounds **1b-5b,** also, the C=N bond appears at ~1539 cm^{-1} which is red shifted from the uncoordinated phenanthroline. There are previous reports in this kind of observations.[2–4] In addition to these, other IR bands that corresponds to -C=O, ≡C–H, C≡C etc. have been observed. All the observed IR bands were listed in Table S5.

Table S6. List of UV-Vis spectra observed in **1-5 (a, b)**

Sl No:	Compound	Wavelength (nm)	Optical transition
UV-Vis			
1	Ligand	278 340	π-π* n-π*
2	2, 2′ bipyridine	232 285	π-π* n-π*
3	1, 10 phenanthroline	256 330	π-π* n-π*
4	Compound **1a-5a**	~280 312-365	π-π* n-π*
5	Compound **1b-5b**	~290 311-364	π-π* n-π*

The room temperature UV-Vis spectra of the ligand (Figure S6a) showed absorption bands corresponding to the л–л* (278 nm) and the n–л* (340 nm) transitions. For the 2, 2′ bipyridine, the bands are observed at λ_{max} 235 and 282 nm for the л–л* and n–л* transitions. Compared to 2,2′-bipyridine, 1,10-phenanthroline possesses a more rigid geometry with the three aromatic rings substantially coplanar and the two nitrogen atoms in juxtaposition.[5] This means that with a greater extent of conjugation, less energy is needed (and the longer the wavelength of radiation) to excite an electron for the л → л* transition, so that extensively conjugated compounds can absorb longer wavelength. Here, the rigidity of phenanthroline is reflected in the structured UV absorption spectral features, where we observed the λ_{max} 256 and 330 nm for the л–л* and n–л* transitions.[6,7] Compound **1a-5a** exhibited a red-shift in the UV-Vis spectra of both the л–л* and n–л* transitions at 280 and 320-350 nm. On the other hand, the UV-Vis spectra of the phenanthroline complexes showed the bands at ~290 nm for the л → л* transition and 311-364 nm for the n–л* transitions.[8] Here in individual peaks are not observed for the ligand, metal and the bipyridine; a overall broad band is observed due to the overlapping of the absorption spectra. Similar kind of observations has been made before.[9] All the observed UV-Vis band is tabulated in Table S6.

Table S7. CIE chromaticity coordinates (x, y) for $Y_{0.98-x}Tb_{0.02}Eu_x$– MOF material samples with different Eu^{3+} concentrations (0 < x < 4.0) and $Y_{0.94-x}Tb_{0.06}Eu_x$– MOF material samples

$Y_{1-0.02-x}Tb_{0.02}Eu_x$ (x = 0.0, 0.5, 1.0, 2.0, 3.0, 4.0 %)			
Sample code	**CIE X**	**CIE Y**	**CCT (K)**
0.0% Eu	0.252	0.455	7885
0.5 % Eu	0.286	0.423	6986
1.0 % Eu	0.303	0.391	6560
2.0 % Eu	**0.33**	**0.345**	**5604**
3.0 % Eu	0.370	0.312	3766
4.0 % Eu	0.411	0.295	2273
$Y_{1-0.06-x}Tb_{0.06}Eu_x$ (x = 0.0, 0.05, 0.10, 0.20, 0.30, 0.40 %)			
0.0% Eu	0.22	0.431	9444
0.05 % Eu	0.291	0.391	7035
0.1 % Eu	**0.332**	**0.331**	**5517**
0.2 % Eu	0.401	0.312	2271
0.3 % Eu	0.435	0.295	1883
0.4 % Eu	0.491	0.274	2291

Table S8. Comparison of the literature reported white light emitting MOF materials with the present White light emitting materials

MOFs	**Excitation wavelength (nm)**	**CIE chromaticity (x, y)**	**CCT (K)**	**Quantum yield (%)**	**Ref.**
$[Dy(TETP)(NO_3)_3]\cdot 4H_2O$	365	0.33, 0.35	-	58%	[10]
$[Zn_3(TCPB)_2(H_2O)_2]\cdot 2H_2O\cdot 4DMF$ 1.05% Eu and 1.56% Tb	254	0.3292, 0.3543	-	-	[11]
NKU-114@9-AA	365	0.34, 0.32	5101	42.07%	[12]
$Eu_{0.005}Tb_{0.095}$-$Bi_{0.9}$-MOF	325	0.33, 0.31	-	-	[13]
$Eu_{0.09}Tb_{0.21}$@1	365	-	-	48.5%	[14]
$[Ir(ppy)_2(bpy)]^+$@$[(CH_3)_2NH_2]_{15}[(Cd_2Cl)_3(TATPT)_4]\cdot 12DMF\cdot 18H_2O$	370	0.31, 0.33	5409	84.5 %	[15]
BGR MOF	360	0.333, 0.336	-	-	[16]
$Tb_{0.31179}Eu_{0.1099}Gd_{0.5782}$-SURMOF	360	0.331, 0.329	5614	-	[17]
ZJU-1:1.0%Tb^{3+},2.0%Eu^{3+}	312	0.32, 0.31		6.11	[18]
$[Eu(H_2O)_2(OH)(Hsfpip)]\cdot H_2O$	380	0.31, 0.35		16.5	[19]
$Y_{0.96}Tb_{0.02}Eu_{0.02}$ (BPTA-bpy)	345	0.334 0.346	5432	28	[20]
$Y_{0.96}Tb_{0.02}Eu_{0.02}$ (BPTA-bpy)	350	0.33, 0.345	5604	31	this work
$Y_{0.939}Tb_{0.06}Eu_{0.001}$(BPTA-phen)	350	0.332, 0.331	5517	43	this work

LOD calculation

The luminescence intensity of the compound was plotted as a function of cation concentration. The limit of detection (LOD) is given by: LOD = 3σ/m, where σ is the standard deviation of the blank measurements without adding the anion and m is the slope of the linear plot.

Table S9. Standard deviation and detection limit calculation for the azinphos-methyl pesticide and nitroaromatics sensing using the Tb and Eu MOFs.

Blank readings of MOFs (without analyte)	Luminescence intensity	Standard deviation (σ)	Slope from the graph (m)	Detection limit (3σ/m)	Limit of detection (LOD) (ppb)
PESTICIDE SENSING					
Tb phen-MOF					
Reading 1	865249	11.2	1.008×10^{7} mM^{-1}	3.33×10^{-6} mM	1.06
Reading 2	865263				
Reading 3	865251				
Reading 4	865239				
Reading 5	865271				
Eu-phen-MOF					
Reading 1	260676	20.84	4.07×10^{6} mM^{-1}	1.53×10^{-5} mM	4.93
Reading 2	260678				
Reading 3	260698				
Reading 4	260743				
Reading 5	260640				
NITROAROMATICS SENSING					
Tb bpy-MOF					
Reading 1	522106	24.61	1.75×10^{7} mM^{-1}	4.21×10^{-6} mM	0.97
Reading 2	522171				
Reading 3	522116				
Reading 4	522128				
Reading 5	522157				
Eu bpy-MOF					
Reading 1	526117	27.89	1.53×10^{7}	5.46×10^{-6}	1.23
Reading 2	526112				
Reading 3	526137				
Reading 4	526157				
Reading 5	526188				

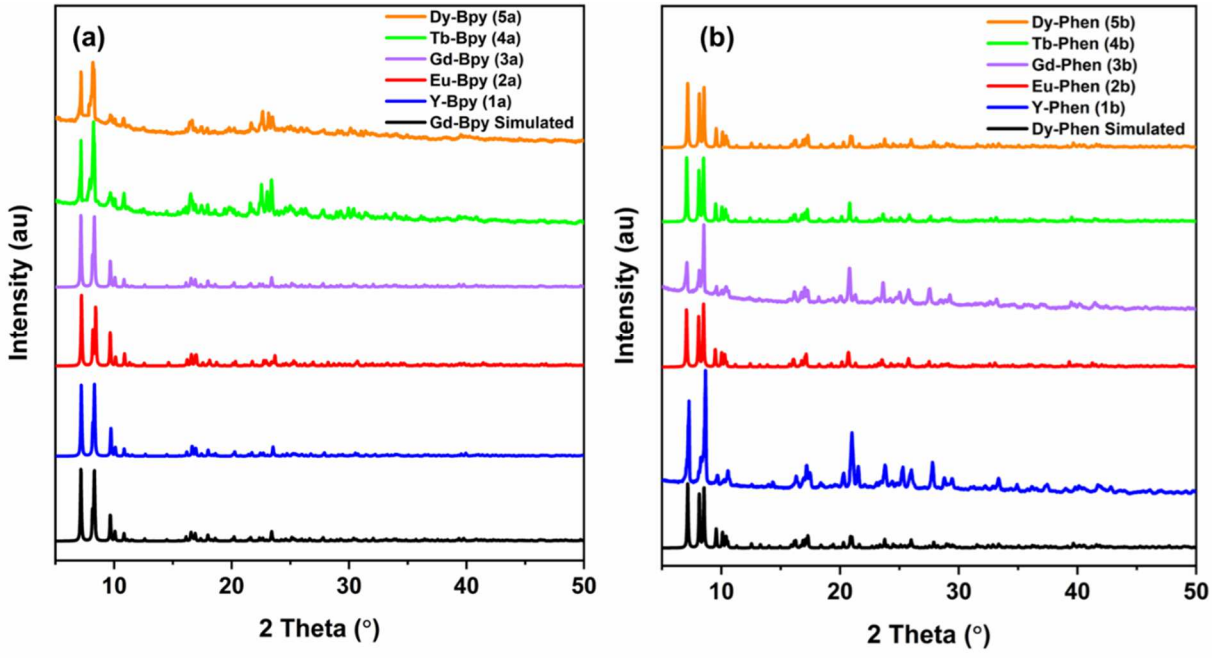

Figure S1. Experimental and simulated PXRD patterns of (a) 3a compound and (b) 5b compound. Note the experimental PXRD pattern of other compounds exactly matches with the simulated pattern of **3a** and **5b**.

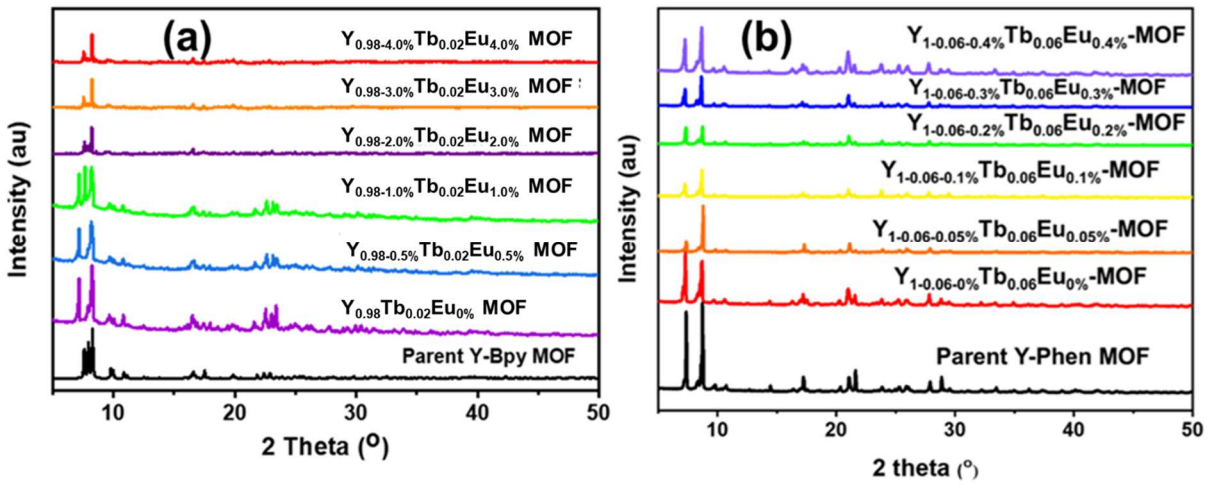

Figure S2. PXRD patterns of **(a)** $Y_{0.98-x\%}Tb_{0.02}Eu_{x\%}$– MOF samples (bpy series) and **(b)** $Y_{0.94-x\%}Tb_{0.06}Eu_{x\%}$– MOF samples (phen series), confirming the structural integrity

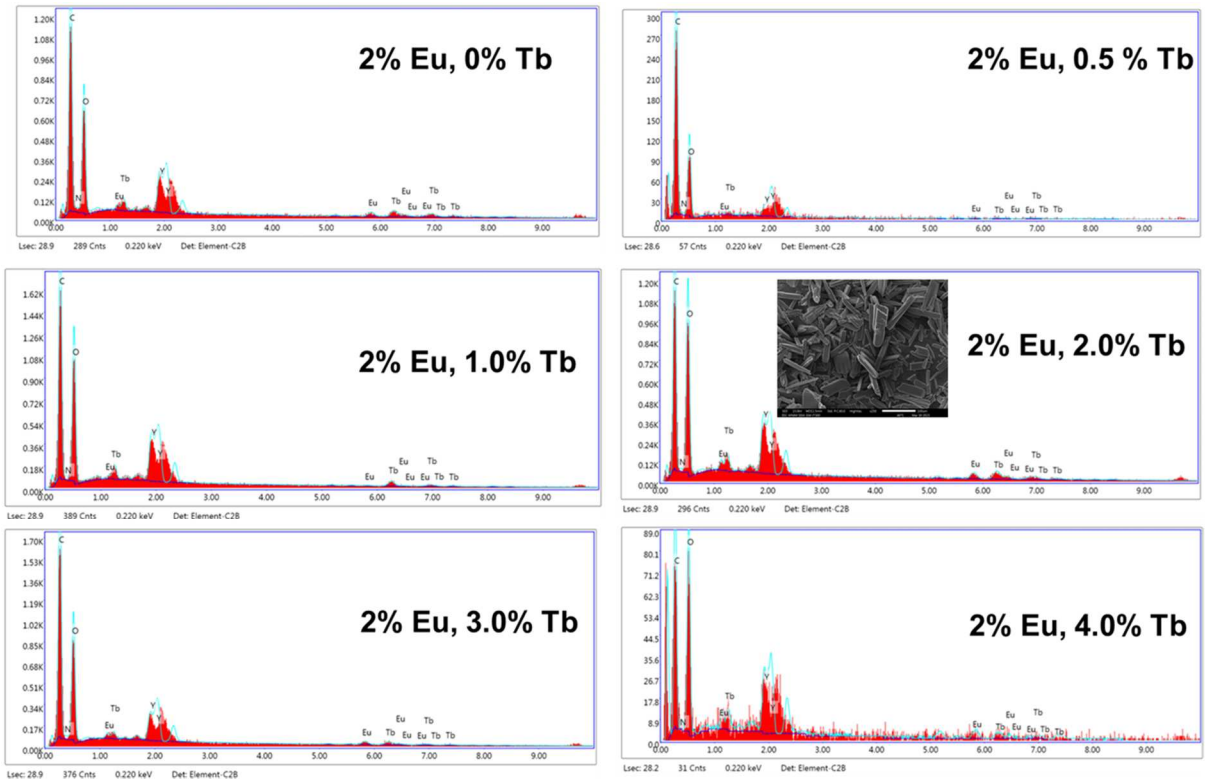

Figure S3. EDX mapping of all dopped Y – bipyridine MOFs ($Y_{1-0.02-x}Tb_{0.02}Eu_x$ (x = 0.0, 0.5, 1.0, 2.0, 3.0, 4.0 %)) samples , SEM image of 2%Tb, 2% Eu, Y- bipyridine MOF

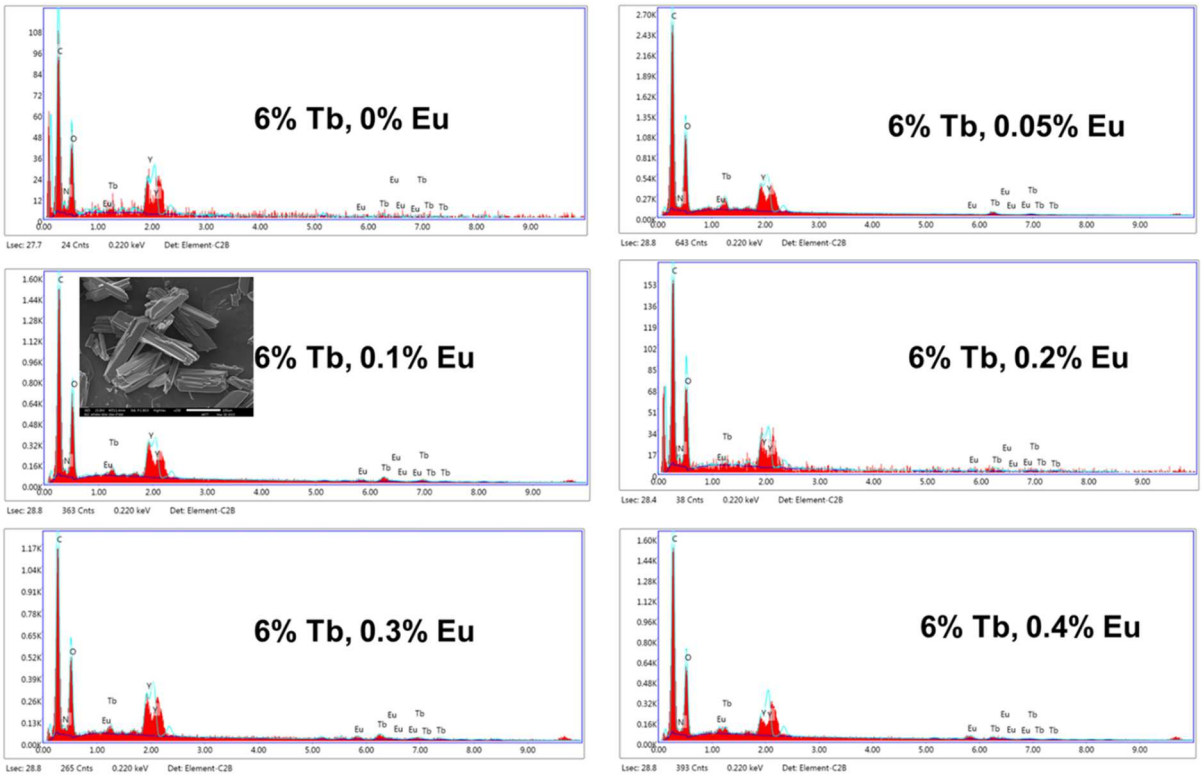

Figure S4. EDX mapping of all dopped Y – bipyridine MOFs ($Y_{1-0.06-x}Tb_{0.06}Eu_x$ (x = 0.0, 0.05, 0.1, 0.2, 0.3, 0.4 %)) samples, SEM image of 6%Tb, 0.1% Eu, Y- 1, 10 phenanthroline MOF

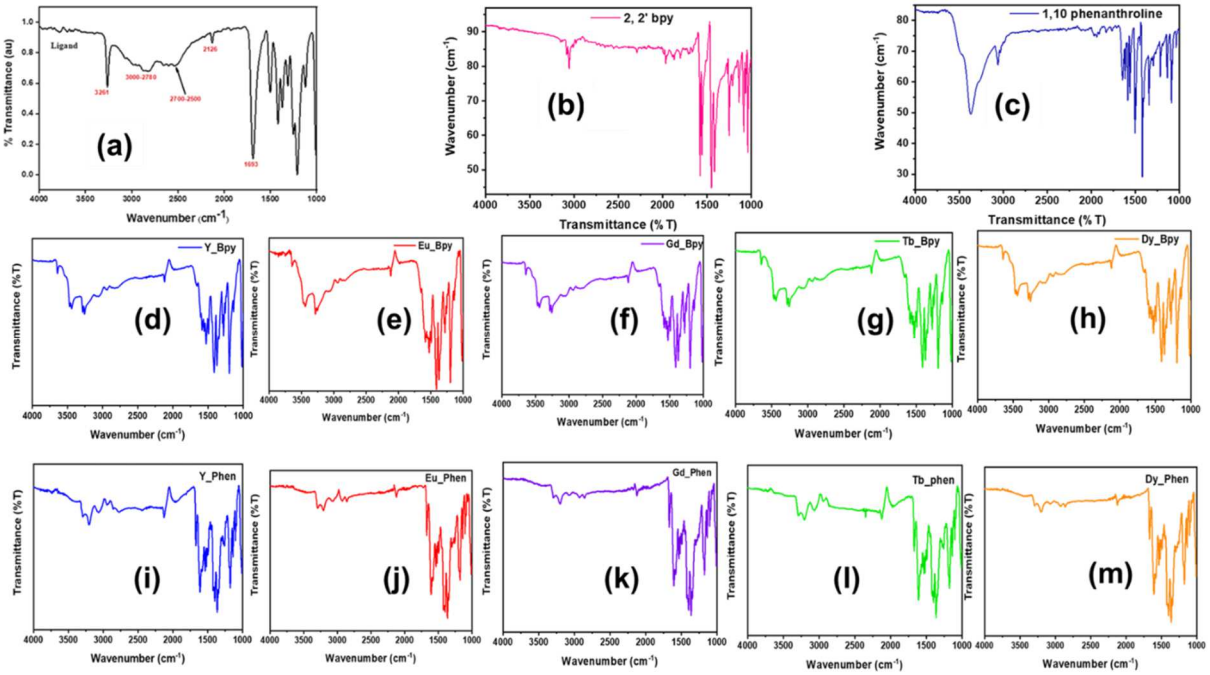

Figure S5. Infrared spectra of ligand (2, 5 BPTA) **(a)**, 2, 2' - bipyridine (b), 1, 10 – phenanthroline (c) Compounds **1a-5a** (d-h) and Compounds **1b-5b** (i-m).

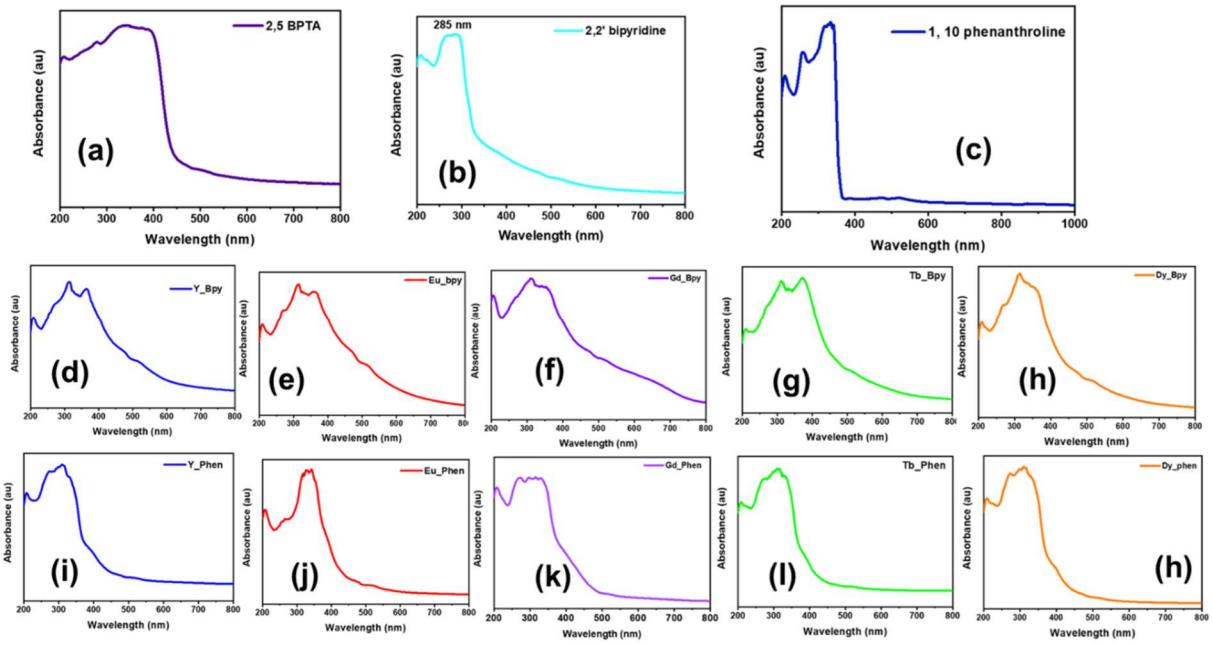

Figure S6. The solid-state UV−Vis absorption spectrum of compound **1-5(a,b)**.

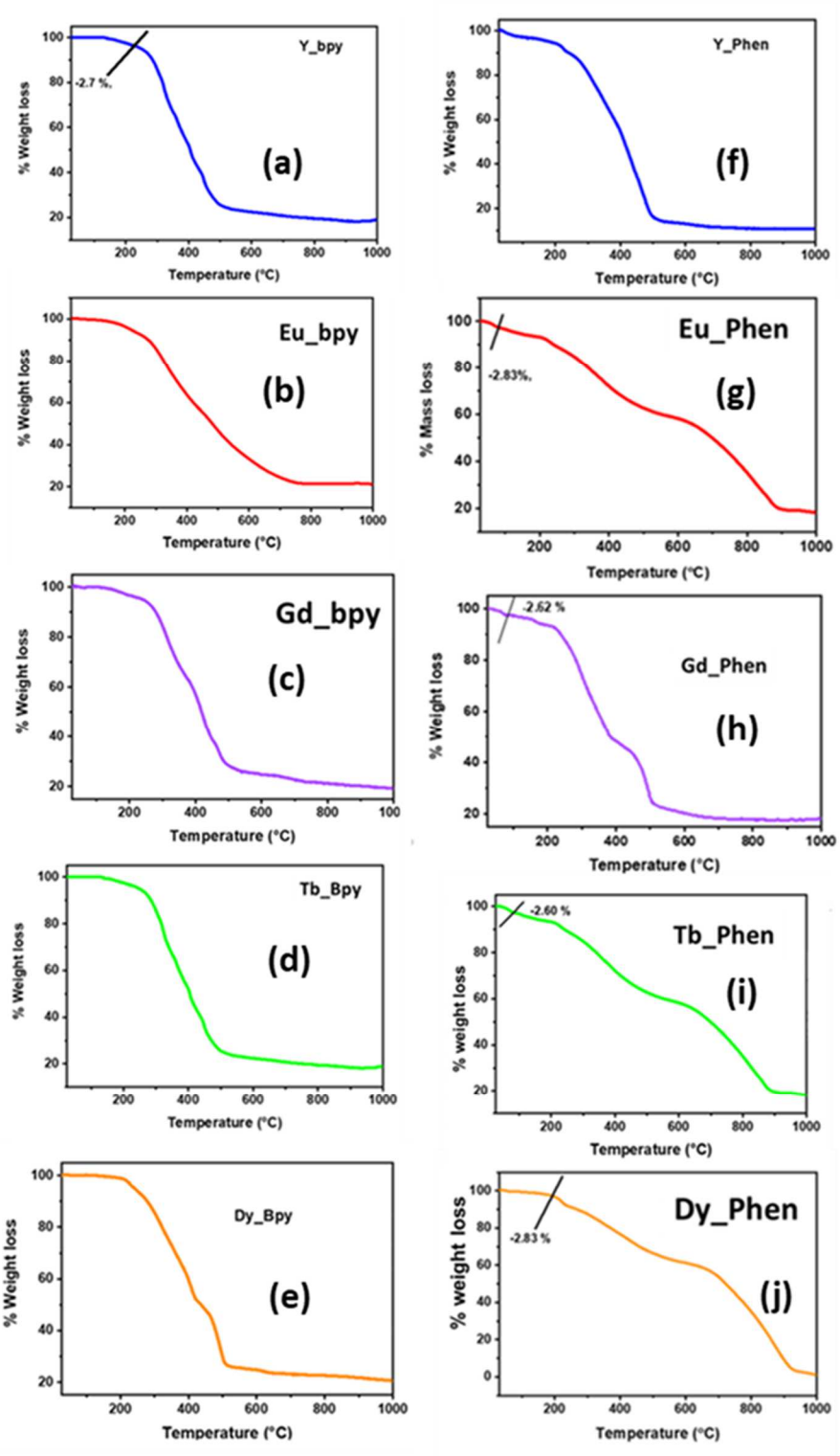

Figure S7. Thermogravimetric analysis curve (TGA) curve of compounds **1a-5a** (a-e) and compounds **1b-5b** (f-j).

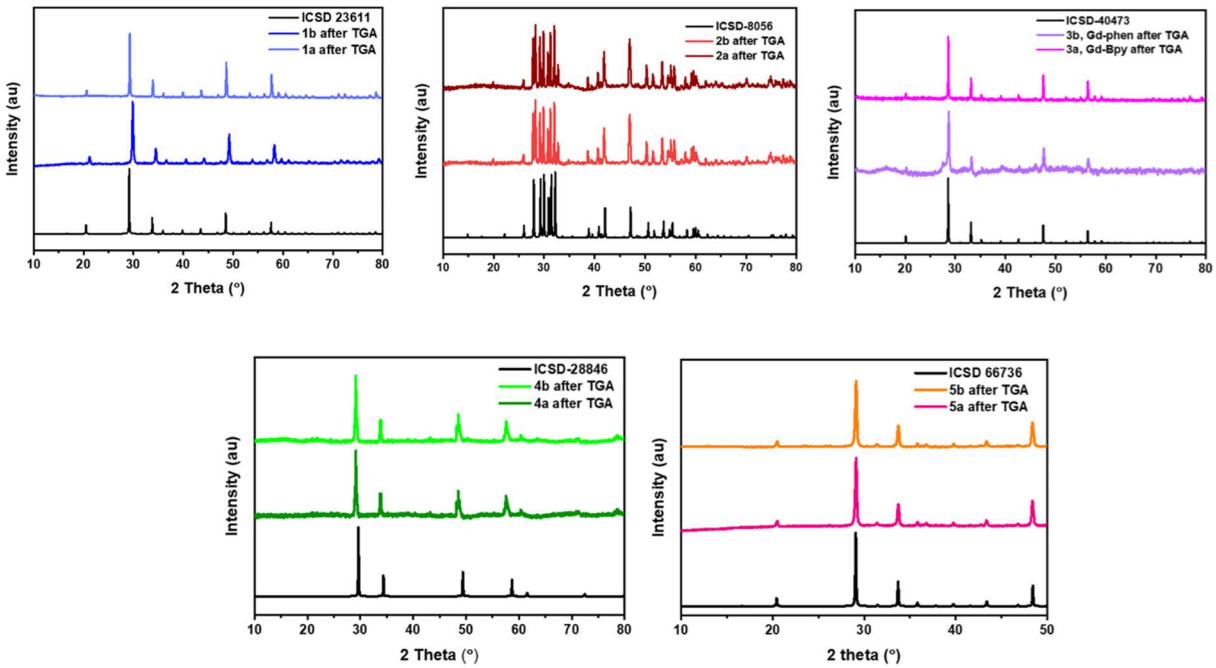

Figure S8. PXRD analysis after thermogravimetric analysis curve (TGA) curve of Compounds **1-5 (a, b).**

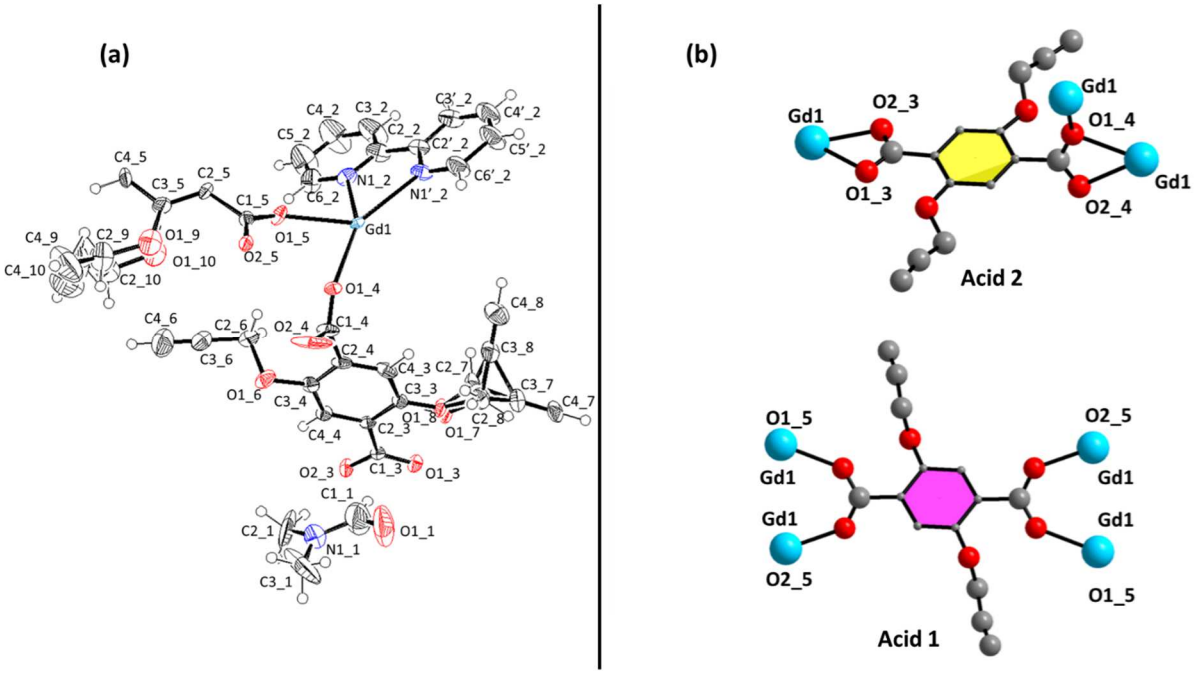

Figure S9. (a) Asymmetric unit of **3a (**Gd-bipyridine compound**)** (Thermal ellipsoid with 50% probability); (b) The various coordination modes of the 2, 5 BPTA anions in Gd MOF, acid 1 and acid 2

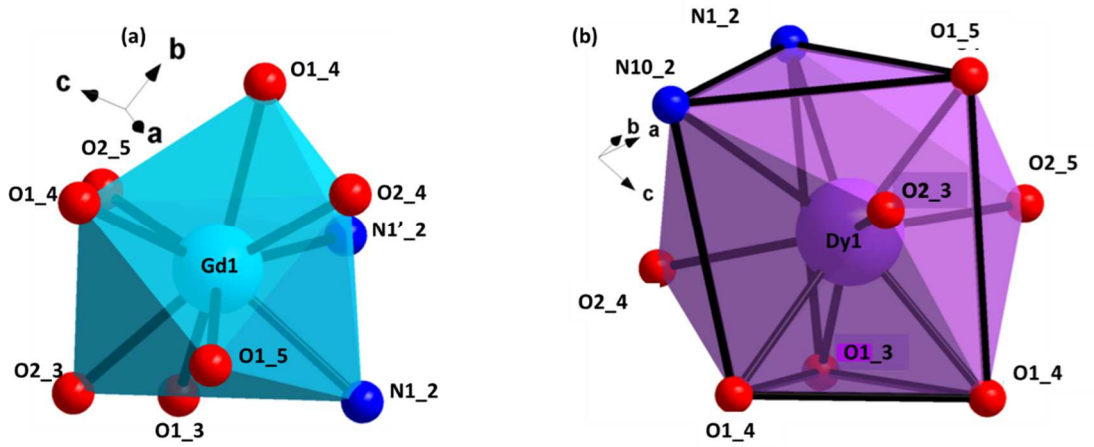

Figure S10. Metal coordination of **(a) Gd** bpy **(3a**) MOF, $[Gd(BPTA)_{1.5}(Bpy)]\cdot 0.5DMF$ capped square antiprismatic geometry and **(b) Dy** phenanthroline **(5b)** MOF, $[Dy(BPTA)_{1.5}(Phen)]\cdot 0.5DMF$ tricapped trigonal prismatic geometry.

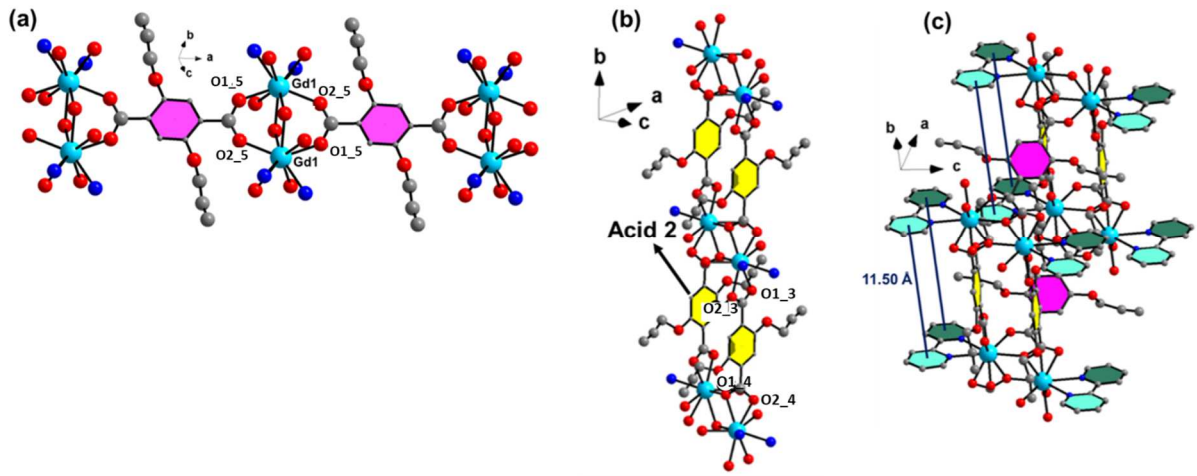

Figure S11. (a) 1D chain formation by acid – 1 **(b)** 1D chain formation by acid 2 **(c)** distance between the bipyridine units in a single layer **(d)** The lattice water molecule interactions with layers.

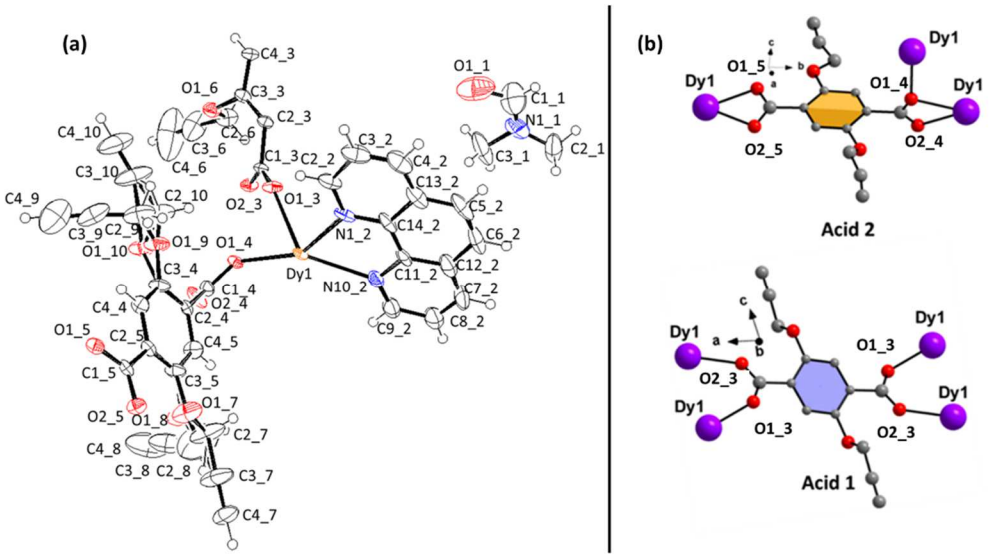

Figure S12. (a) Asymmetric unit of **5b** (Dy-phen compound) (Thermal ellipsoid with 50% probability); **(b)** The various coordination modes of the 2, 5 BPTA anions in Dy MOF, acid 1 and acid 2

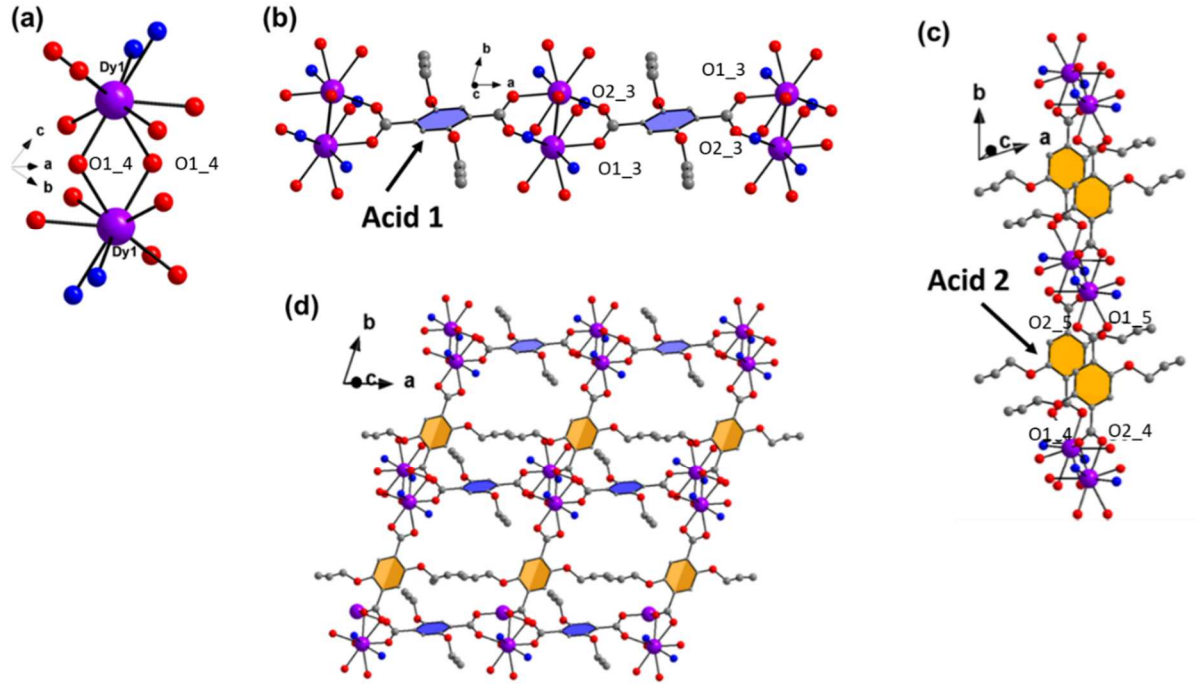

Figure S13. (a) Dimeric unit formed by O6 atom **(b)** 1D chain propagation by the Acid 1-unit **(c)** 1D chain propagation by Acid 2 (d) 2D layer formation in **5b**; phenanthroline containing MOF

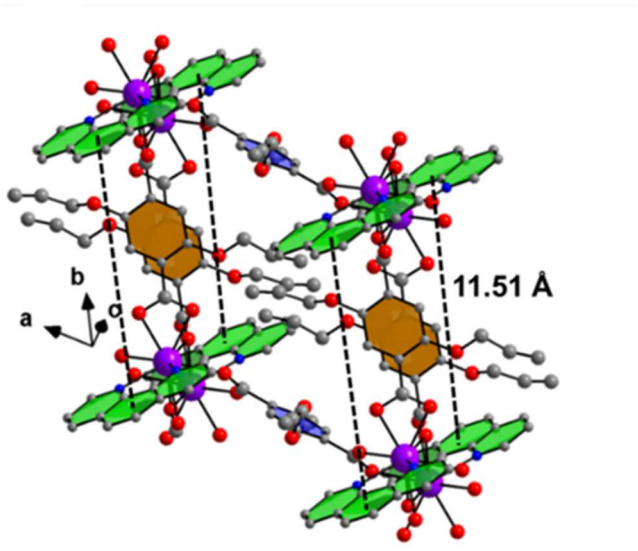

Figure S14. Distance between 1, 10 phenanthrolines in a single layer

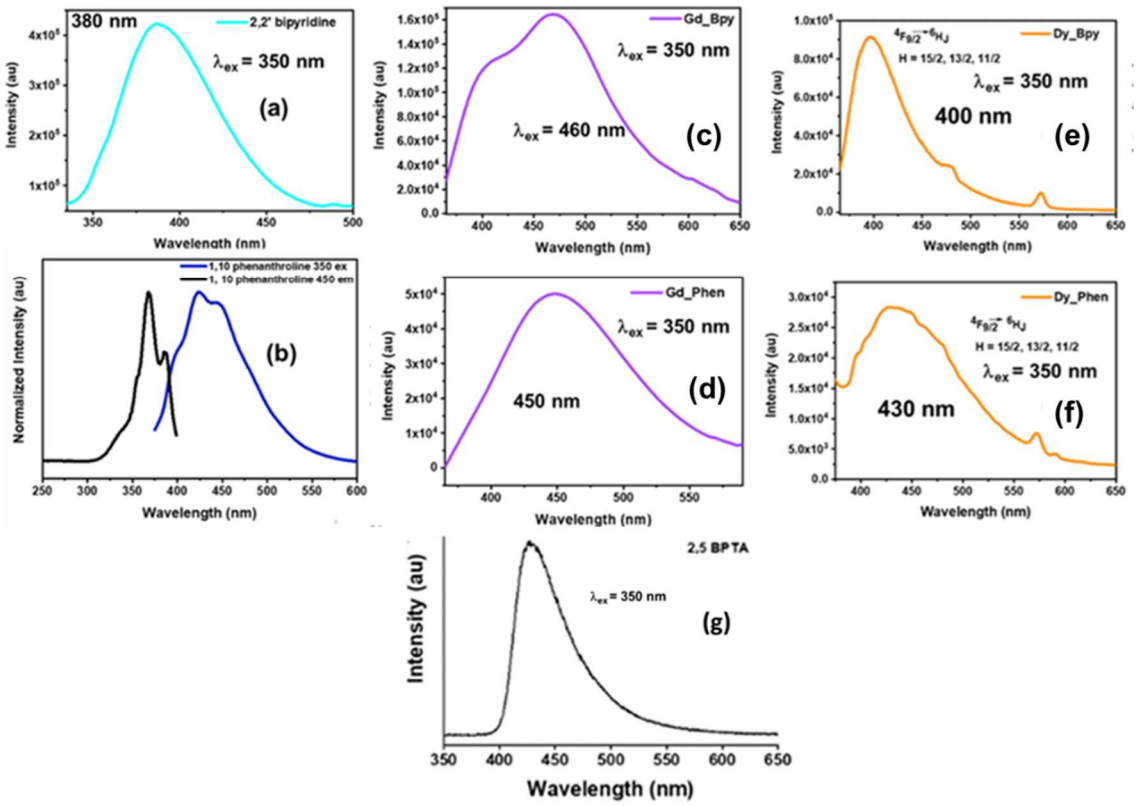

Figure S15. Room-temperature photoluminescence spectra for 2, 2’ bipyridine, 1, 10 phenanthroline, compound **3a** (c), **3b** (d), **5a** (e), **5b** (f) and the ligand (g)

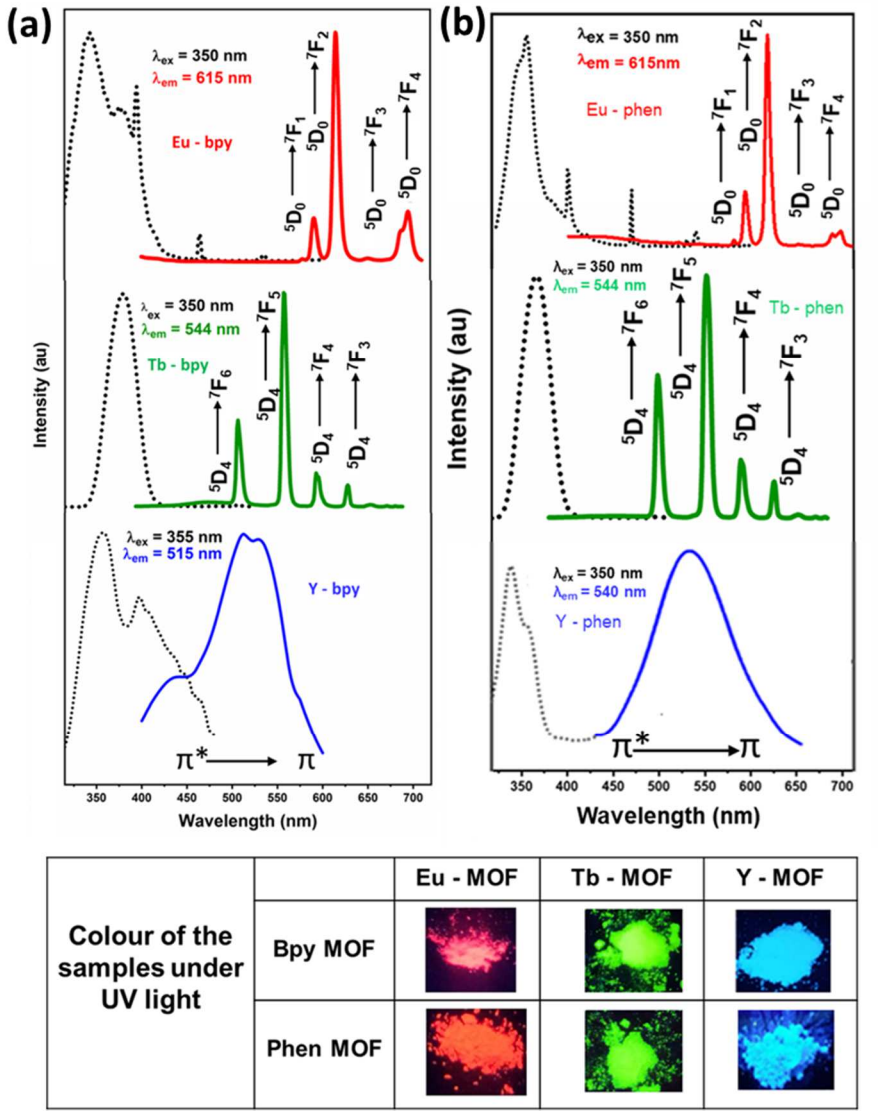

Colour of the samples under UV light		Eu - MOF	Tb - MOF	Y - MOF
	Bpy MOF			
	Phen MOF			

Figure S16. Excitation (black dotted) and emission spectra of Eu-MOF, Tb-MOF, Y-MOF in the solid-state Inset: Photograph showing the luminescence colour of the MOFs under long UV lamp. Note the characteristic red, green and blue colour for Eu^{3+}, Tb^{3+} and the Y containing compound, **(a)** 2, 2′ Bipyridine containing compounds **(b)** 1, 10 phenanthroline containing compounds.

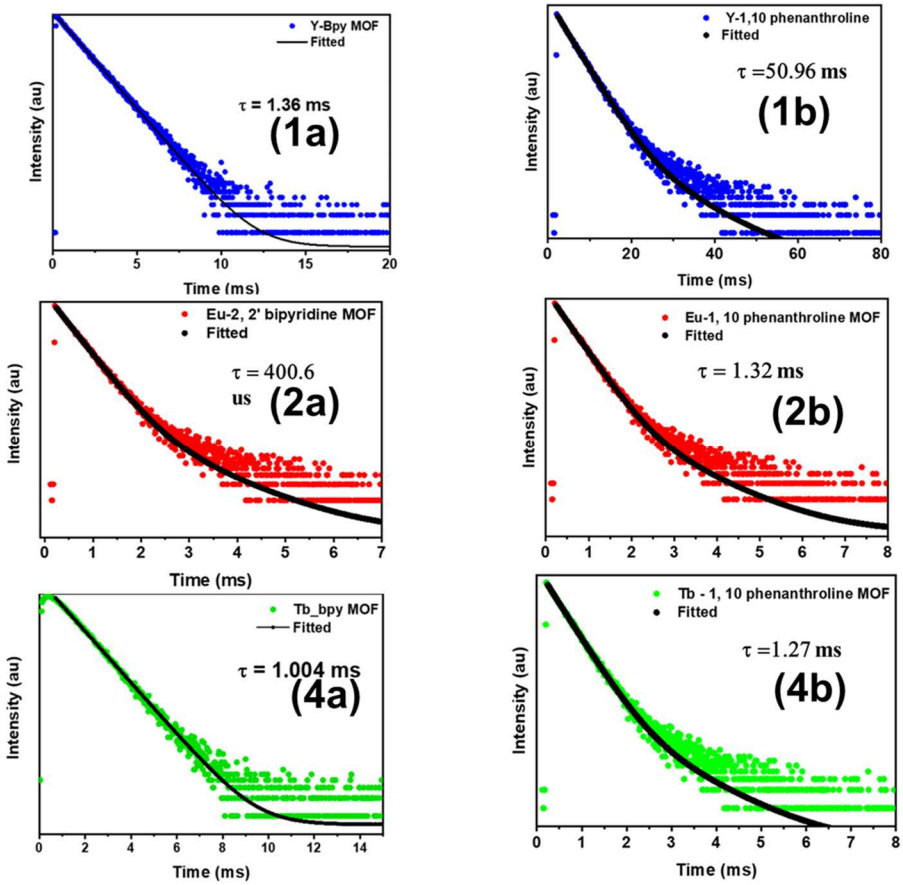

Figure S17. Luminescence decay profiles (298K) for Y, Eu and Tb MOFs.

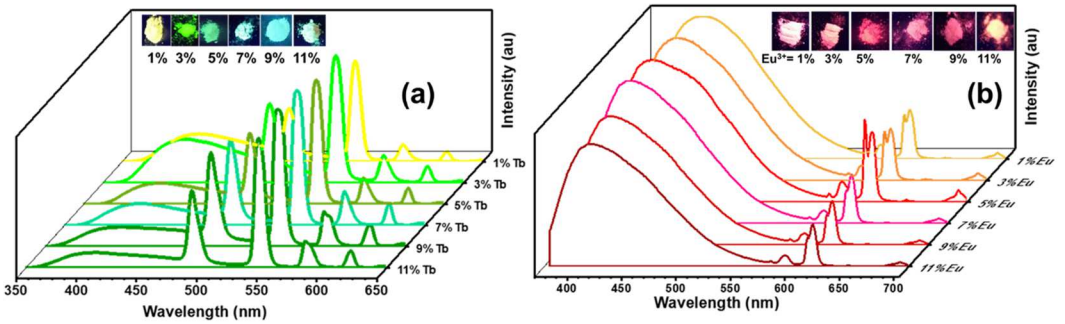

Figure S18. Different substitution of Tb^{3+} **(a)** and Eu^{3+} **(b)** in Y- bpy MOF

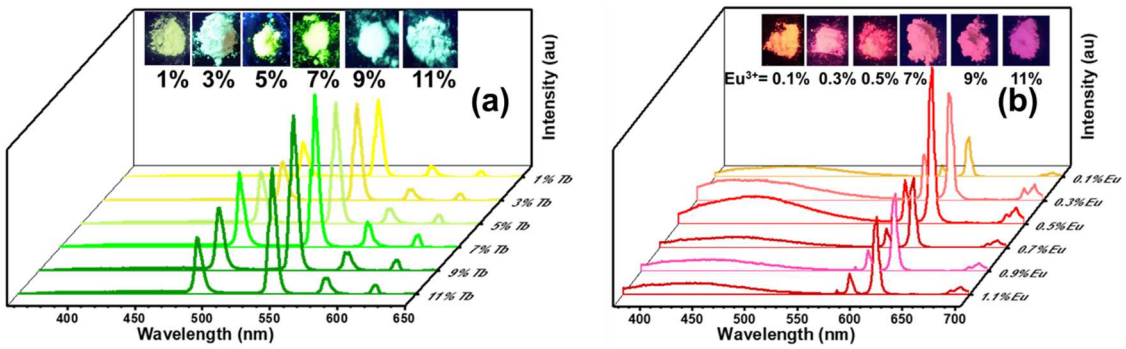

Figure S19. Different substitution of Tb^{3+} **(a)** and Eu^{3+} **(b)** in Y- phen MOF

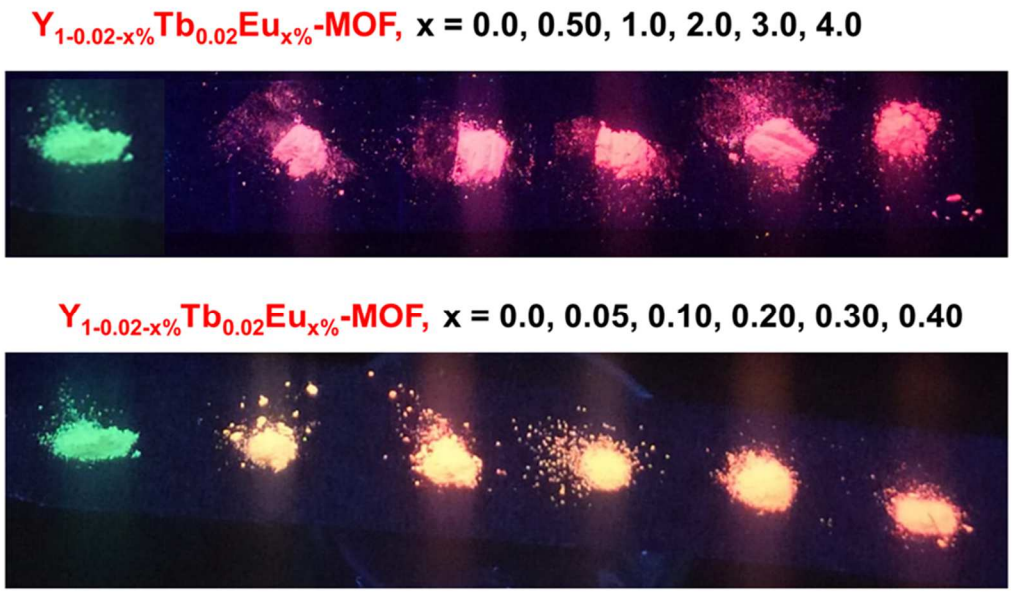

Figure S20. Colour of the $Y_{1-0.02-x\%}Tb_{0.02}Eu_{x\%}$-MOF (x = 0.0, 0.5, 1, 2, 3, 4) and $Y_{1-0.02-0\%}Tb_{0.02}Eu_{x\%}$-MOF (x = 0.0, 0.05, 0.1, 0.2, 0.3, 0.4) samples under UV light

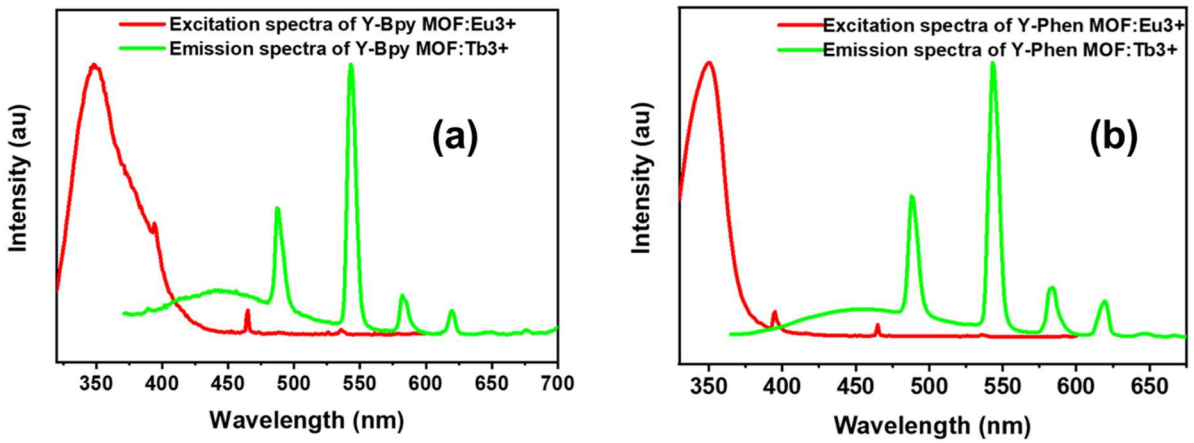

Figure S21. The spectral overlap between the PLE spectrum of Y-MOF: Eu^{3+} and PL spectrum of Y-MOF: Tb^{3+} materials **(a)** Y-bipyridine MOFs **(b)** Y-phenanthroline MOFs.

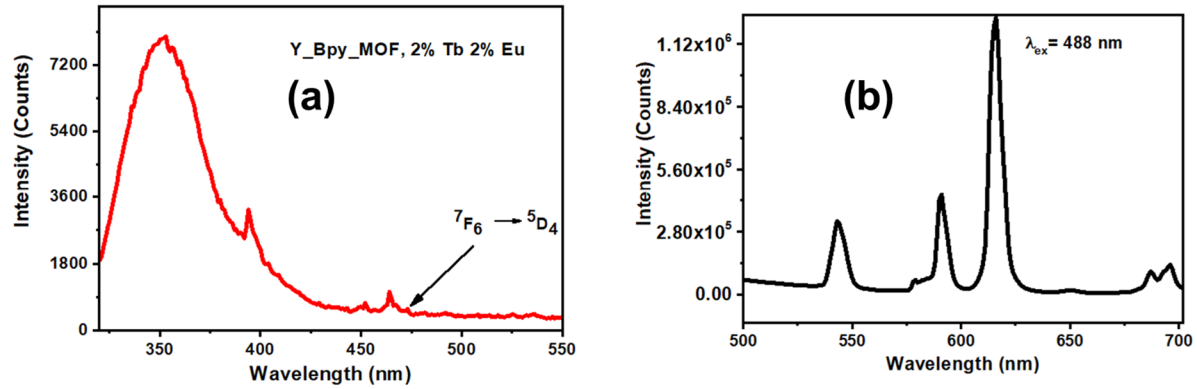

Figure S22. **(a)** The excitation spectrum of Y-MOF bipyridine, 2% Tb^{3+}, 2% Eu^{3+} sample monitored at 616 nm; **(b)** The emission spectrum of the sample at the excitation of 488nm.

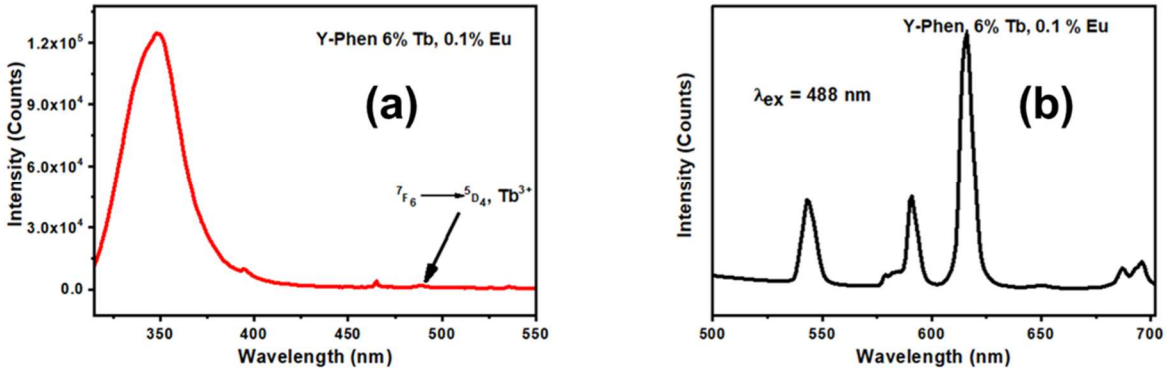

Figure S23. (a) The excitation spectrum of Y-MOF phenanthroline, 6% Tb^{3+}, 0.1% Eu^{3+} sample monitored at 616 nm; **(b)** The emission spectrum of the sample at the excitation of 488 nm.

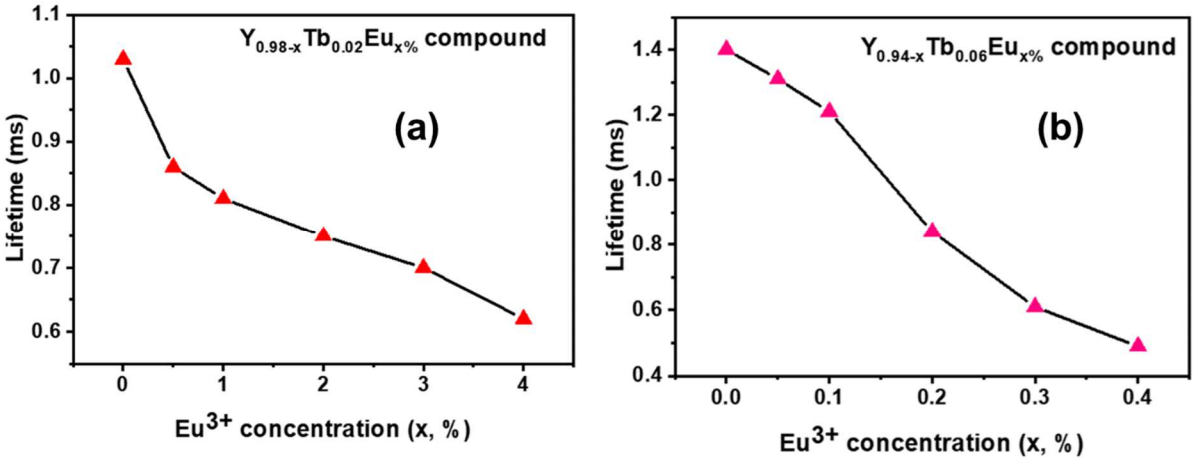

Figure S24. Lifetime vs concentration of the Eu^{3+} plot **(a)** $Y_{0.98-x}Tb_{0.02}Eu_x$ and **(b)** $Y_{0.94-x}Tb_{0.06}Eu_x$ compounds.

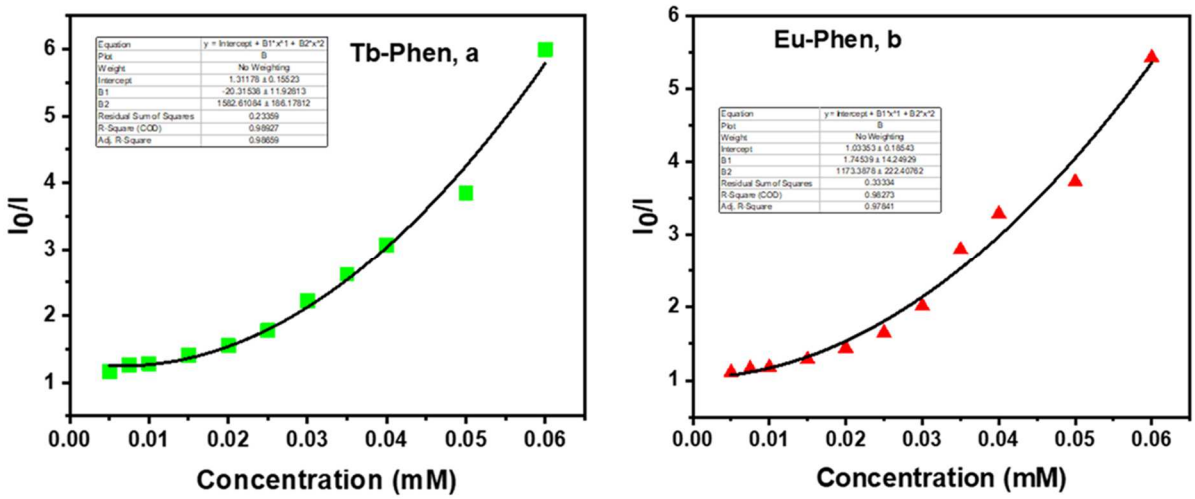

Figure. S25. Stern-Volmer plots for **(a)** Tb and **(b)** Eu – phen MOF at high concentration of azinphos-methyl sensing

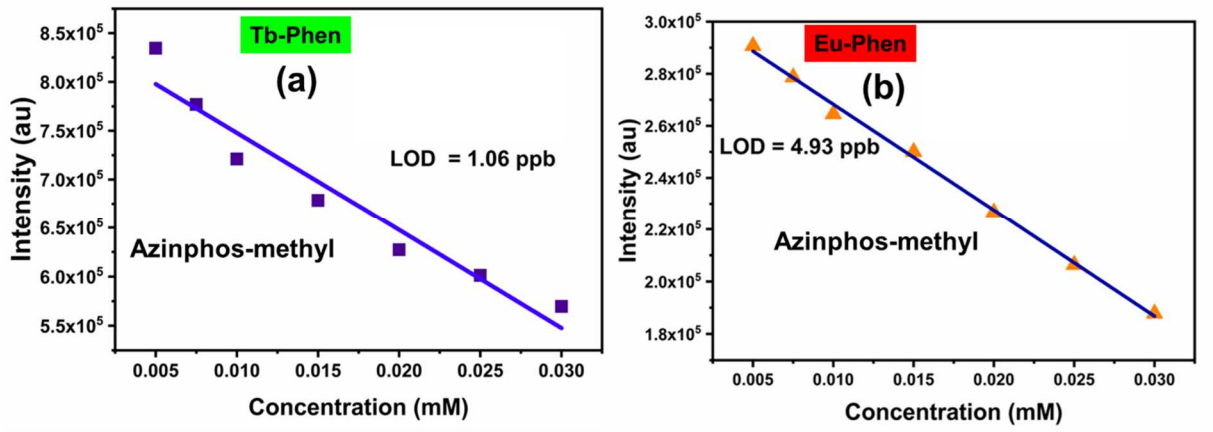

Figure 26. The LOD calculation graph for the pesticide sensing in Tb-phen and Eu-phen MOFs

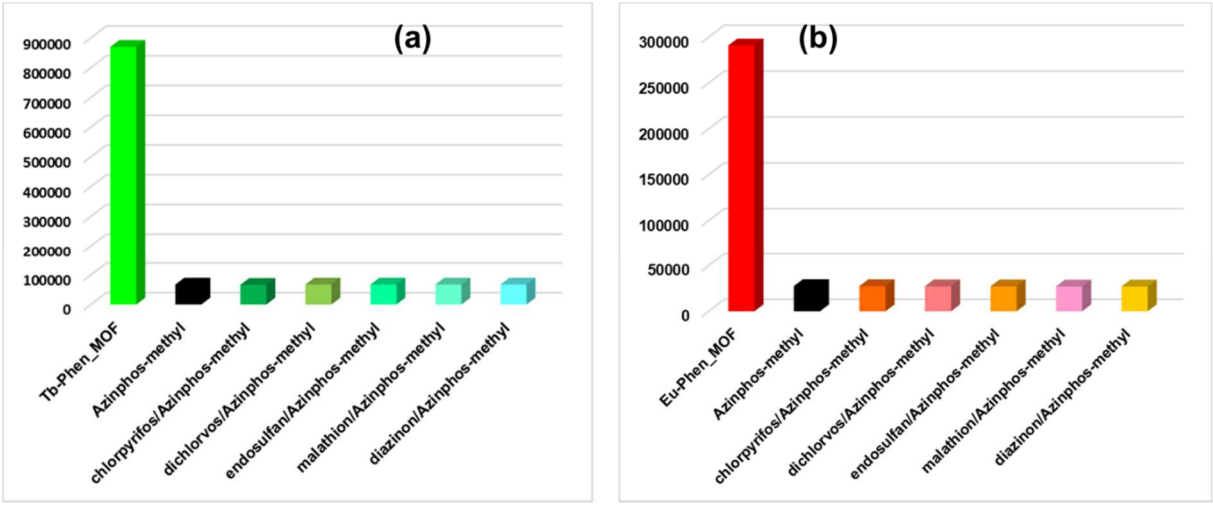

Figure S27. Comparison of the luminescence quenching effect of Azinphos methyl in the presence of other pesticides (75 mM) using **(a)** Tb-phen MOF and **(b)** Eu-phen MOF.

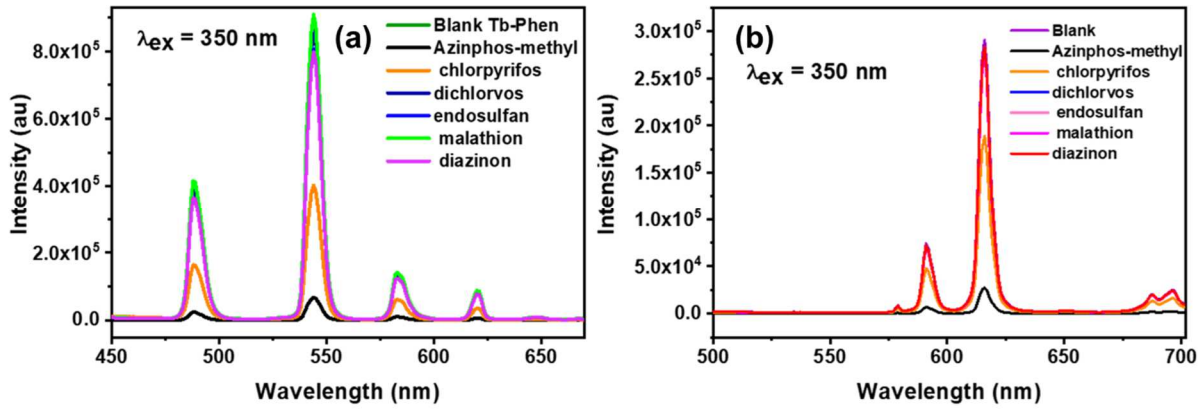

Figure S28. (a) Emission spectra of Tb-phen compound **(b)** Emission spectra of Eu-phen compound dispersed in water upon addition of acetonitrile solution of different pesticide solutions Azinphos-methyl, Chlorpyrivos, Dichlorvos, Endosulfan, Malathion, Diazinon (λ_{ex} = 350 nm). Concentration of pesticides are 75 mM in the medium

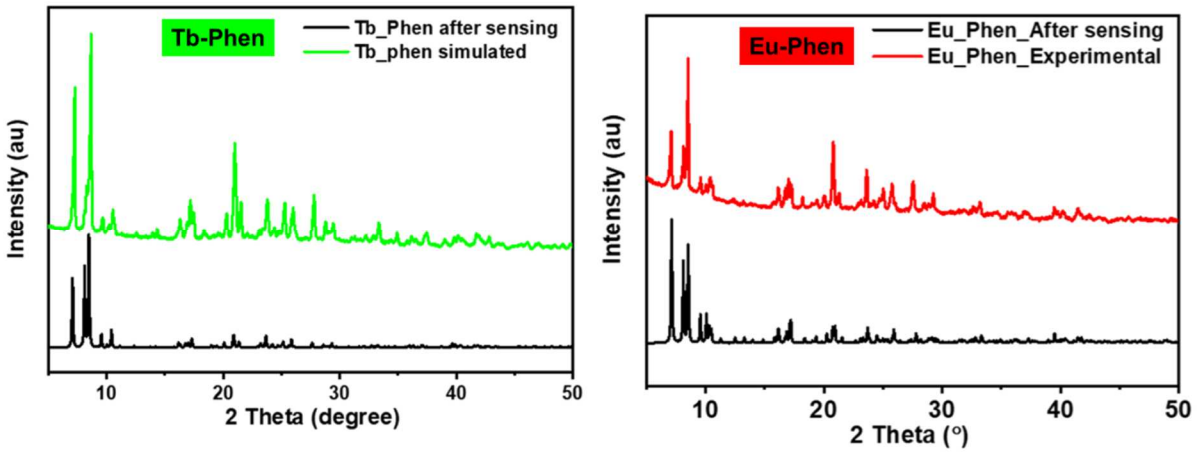

Figure S29. The PXRD study was carried out after the pesticide sensing studies, which indicated the structural integrity of MOF compounds

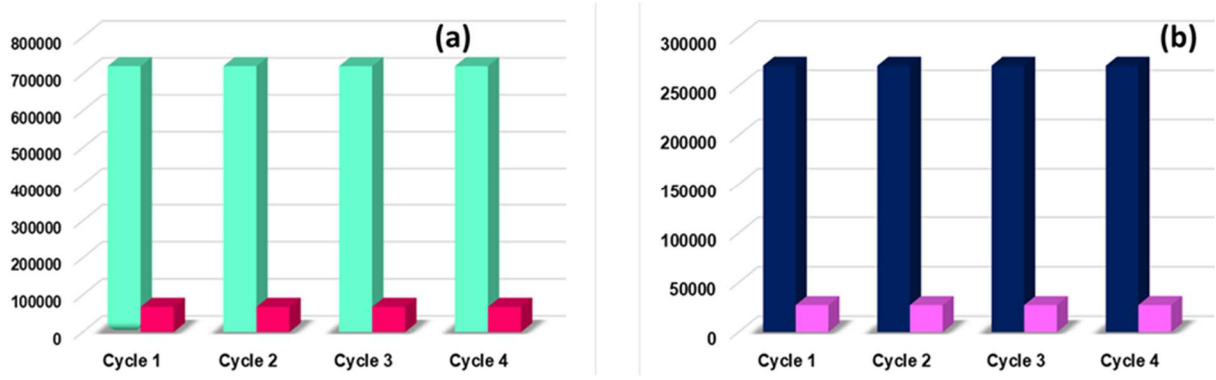

Figure S30. The Recyclability study for the pesticide sensing using the Tb (a) and Eu MOF (b).

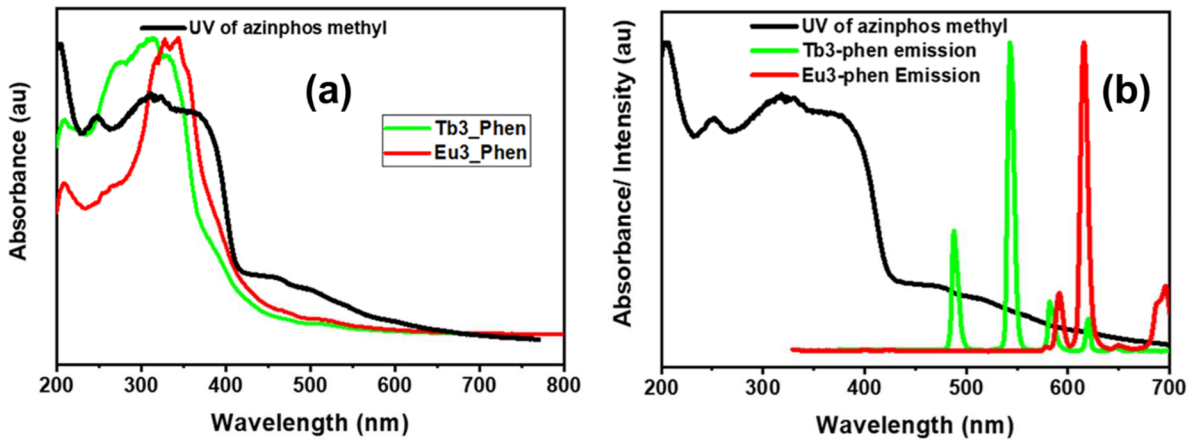

Figure S31. (a) Spectral overlap of the absorption spectra of the azinphos-methyl and the Tb and the Eu – phen MOF compounds. **(b)** The absorption bands of analytes along with the emission spectra of Tb MOF. Note the considerable overlap (see text).

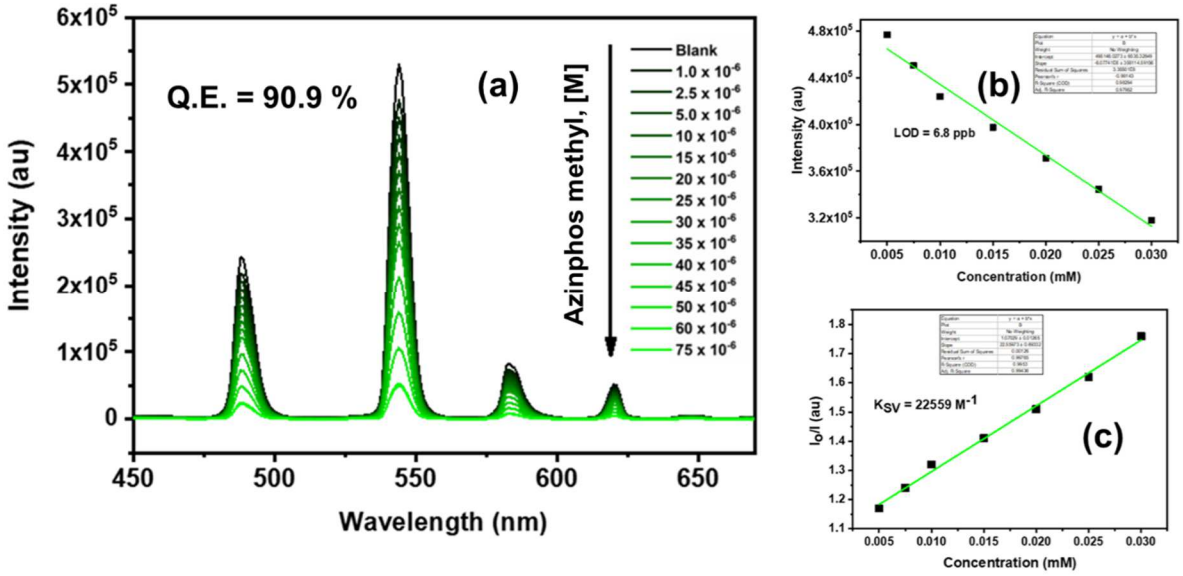

Figure S32. **(a)** Emission spectra of Tb - bpy MOF dispersed in water upon incremental addition of acetonitrile solution of azinphos- methyl (λ_{ex} = 350nm). Final concentration of pesticide in the medium is indicated in the legend. **(b)** The LOD calculation graph for the pesticide sensing in Tb-bpy MOF **(c)** Plot of I_0/I of Tb - bpy MOFs (at 544 nm) *vs* concentration

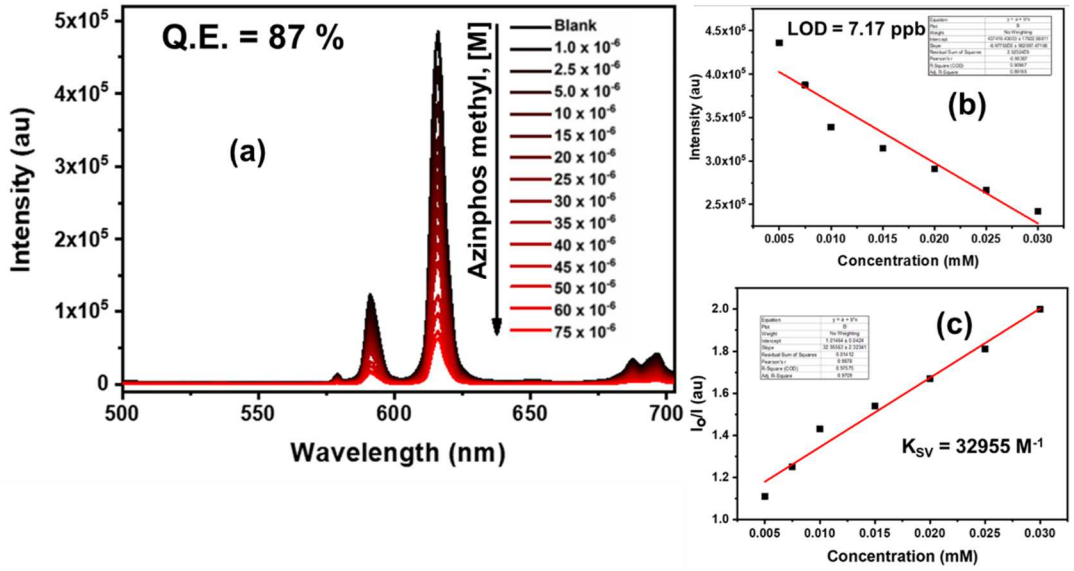

Figure S33. **(a)** Emission spectra of Eu -bpy MOF dispersed in water upon incremental addition of acetonitrile solution of Azinphos - methyl (λ_{ex} = 350nm). Final concentration of pesticide in the medium is indicated in the legend. **(b)** The LOD calculation graph for the pesticide sensing in Eu-bpy MOF **(c)** Plot of I_0/I of Eu-bpy MOFs (at 616 nm) *vs* concentration

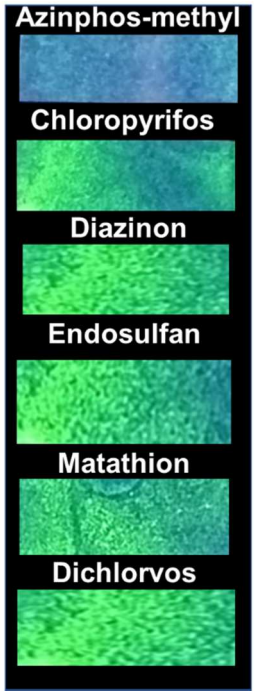

Figure S34. Colour of Tb-phen coated paper strips in presence of different pesticides (75 µM). Note: the green colour vanishes only in the presence of azinphos-methyl.

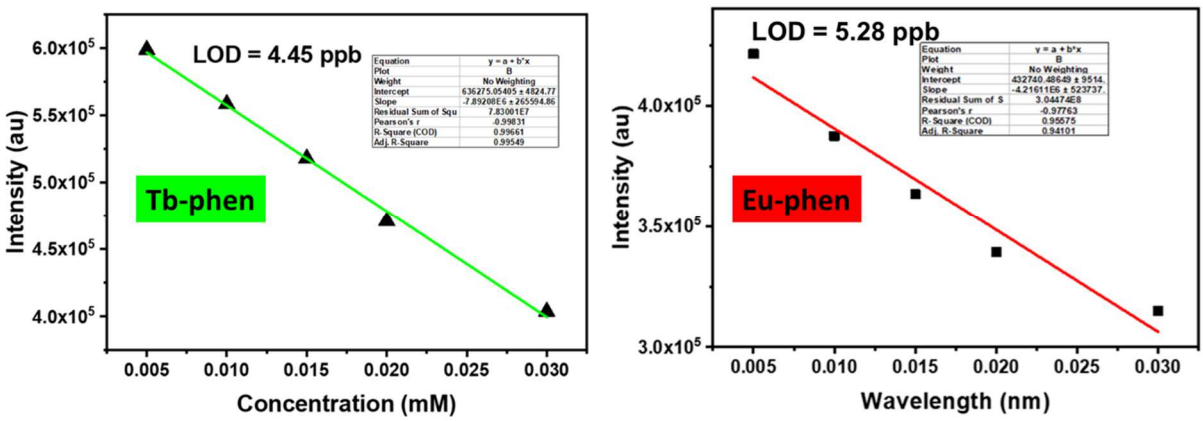

Figure S35. The LOD calculation graph for the azinphos-methyl using paper strips in Tb-phen and Eu-phen

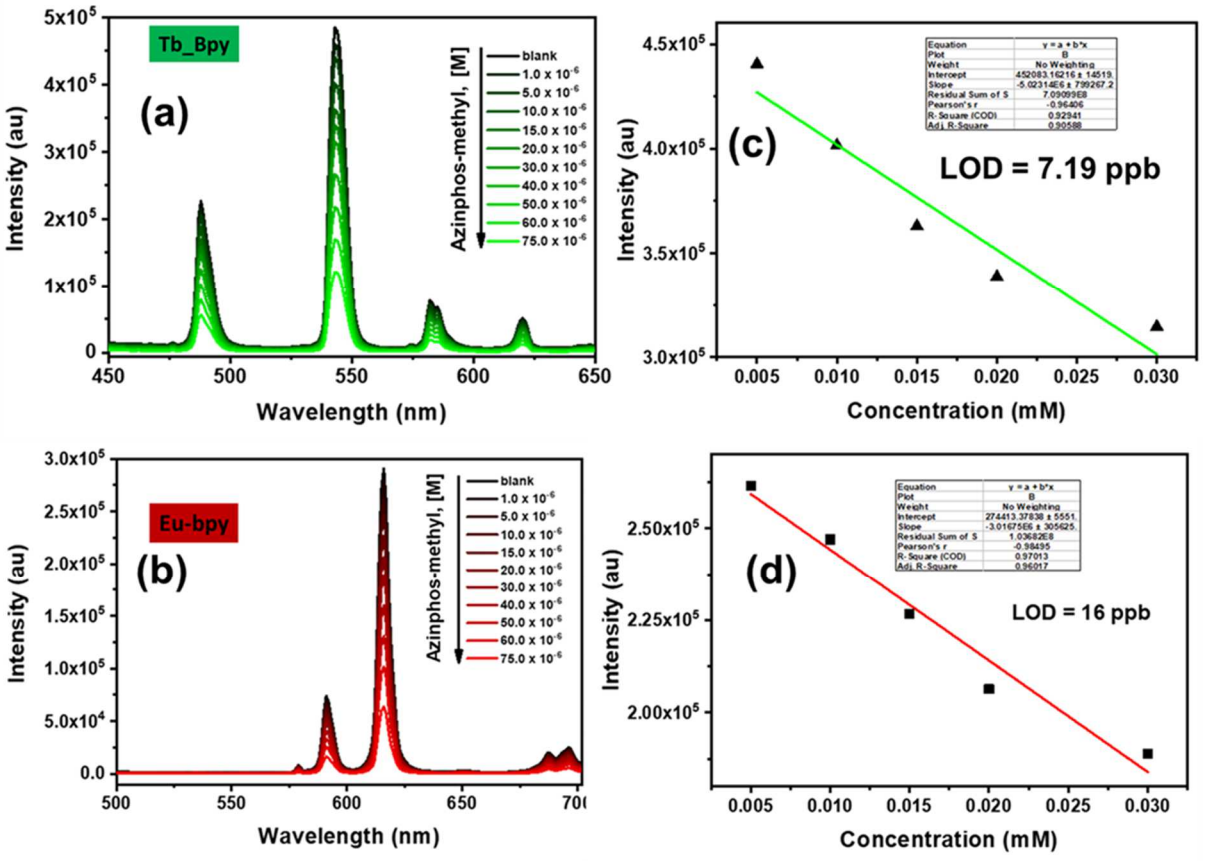

Figure S36. The decrease in luminescence intensity of the MOF coated paper strips dipped in different concentrations of azinphos-methyl solution **(a)** Tb-bpy **(b)** Eu-bpy and LOD values for the azinphos-methyl solution **(c)** Tb-bpy **(d)** Eu-bpy

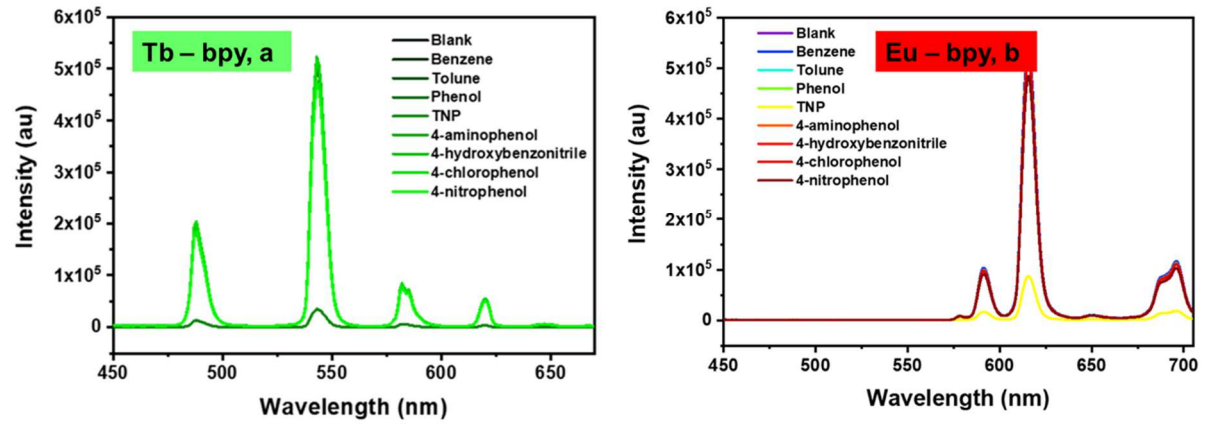

Figure S37. (a) Emission spectra of Tb-bpy compound **(b)** Emission spectra of Eu-bpy compound dispersed in water upon addition of acetonitrile solution of TNP and different Aromatic compound solutions benzene, toluene, phenol (λ_{ex} = 350 nm). Concentration of analytes are 100 mM in the medium

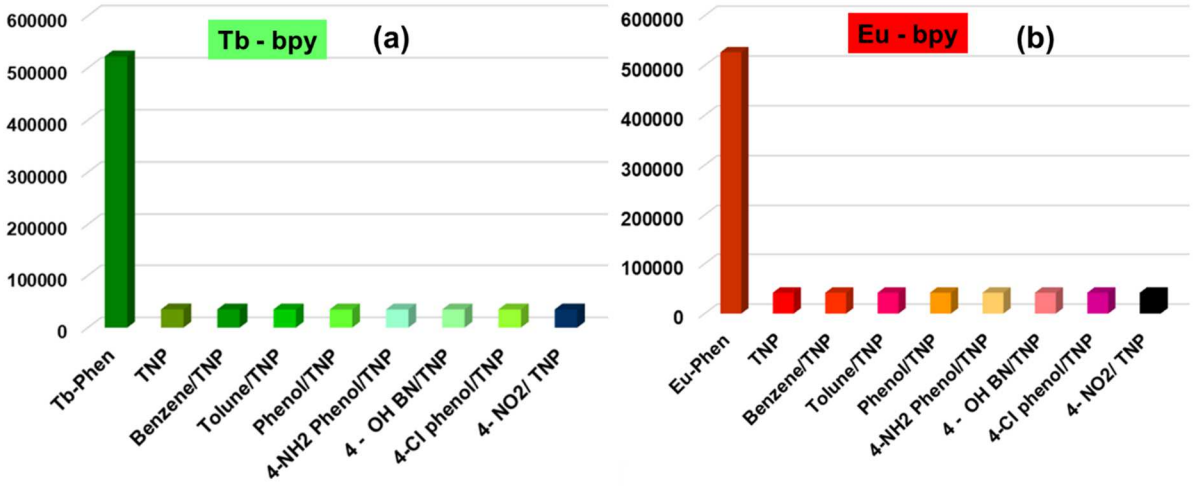

Figure S38. Comparison of the luminescence quenching effect of TNP in the presence of other aromatics (100 mM) using **(a)** Tb-bpy MOF and **(b)** Eu-bpy MOF

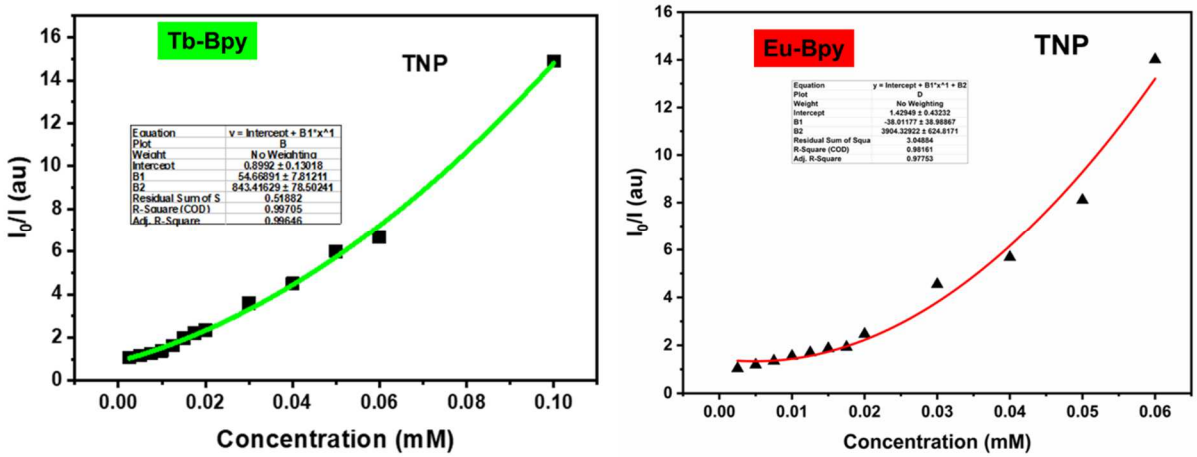

Figure. S39. Stern-Volmer plots for **(a)** Tb and **(b)** Eu – bpy MOFs at high concentration of Trinitrophenol.

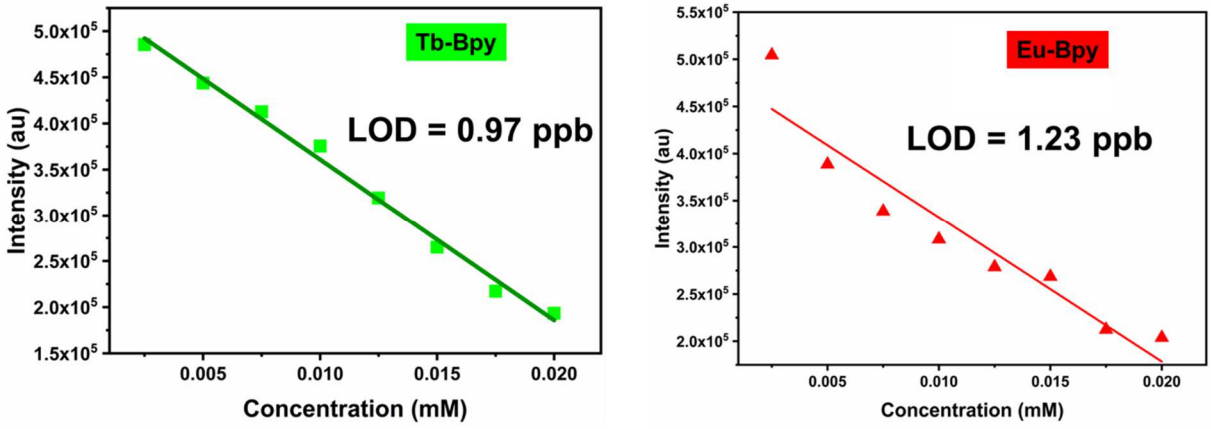

Figure 40. The LOD calculation graph for the TNP sensing in Tb-bpy and Eu bpy

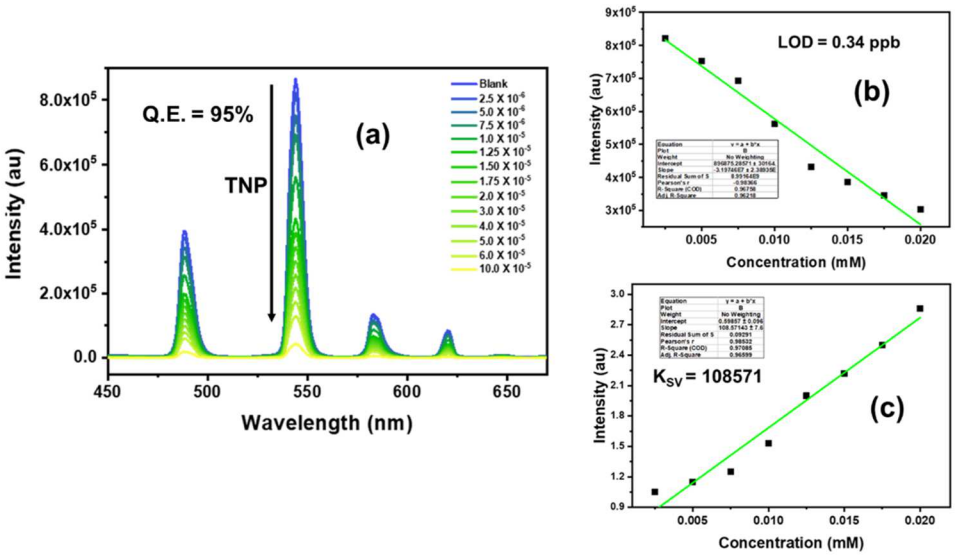

Figure S41. **(a)** Emission spectra of Tb-phen MOF dispersed in water upon incremental addition of acetonitrile solution of Trinitrophenol (λ_{ex} = 350nm). Final concentration of TNP in the medium is indicated in the legend. **(b)** The LOD calculation graph for the TNP sensing in Tb-phen MOF **(c)** Plot of I_0/I of Tb-phen MOF (at 544 nm) *vs* concentration

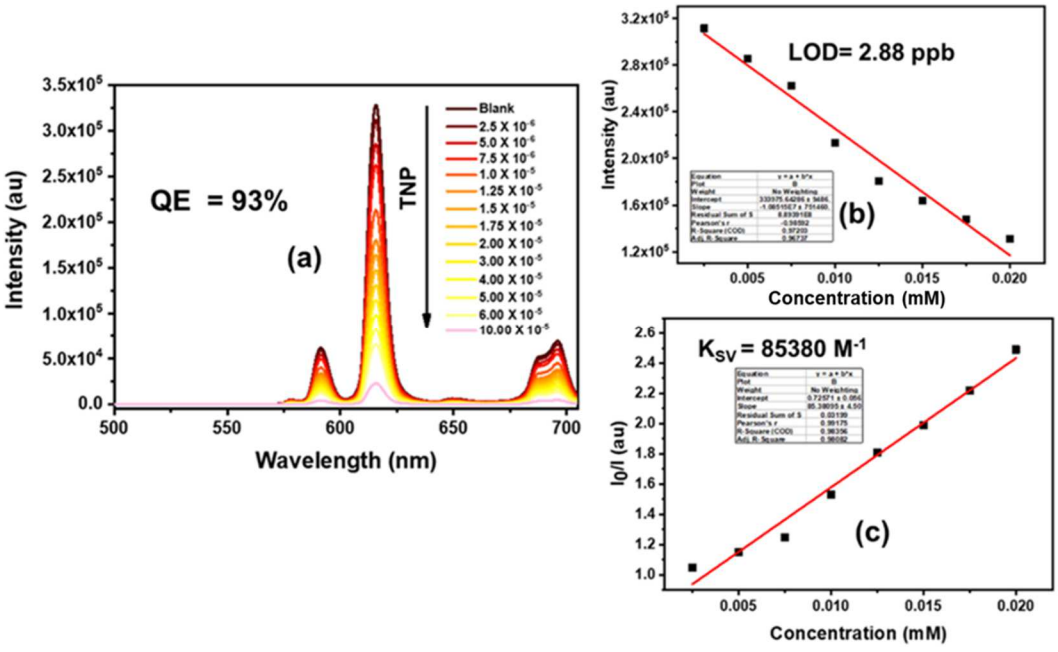

Figure S42. (a) Emission spectra of Eu -phen MOF dispersed in water upon incremental addition of acetonitrile solution of trinitrophenol (λ_{ex} = 350nm). Final concentration of TNP in the medium is indicated in the legend. **(b)** The LOD calculation graph for the TNP sensing in Eu - phen MOF **(c)** Plot of I_0/I of Eu-bpy MOFs (at 616 nm) *vs* concentration

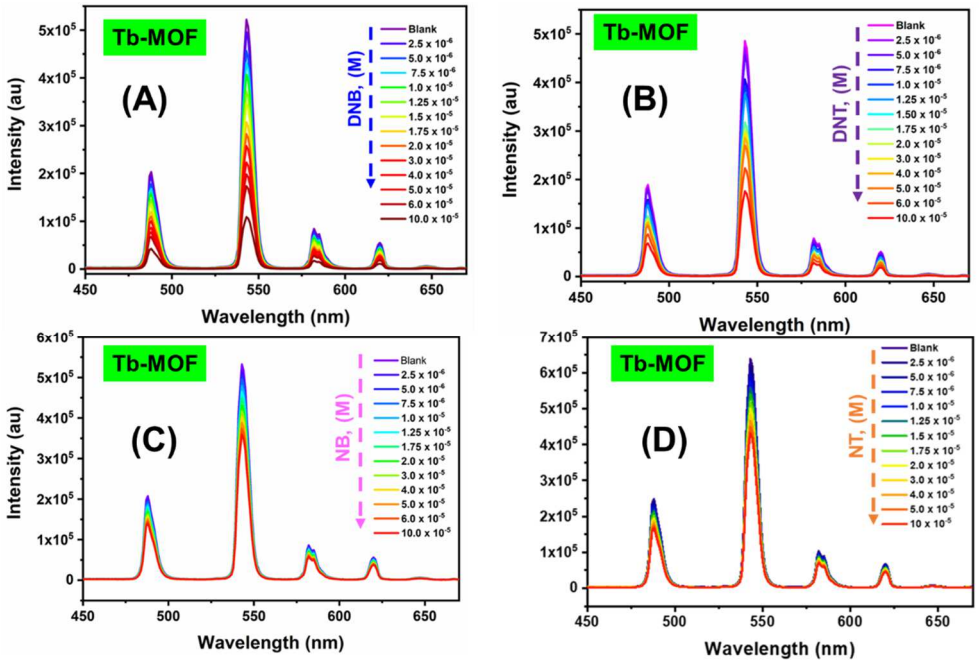

Figure S43. Emission spectra of Tb-bpy MOF dispersed in acetonitrile upon incremental addition of (a) DNB (b) DNT (c) NB (d) NT solution (lex = 350 nm). The final concentration of all the nitroaromatics in the medium is indicated in the legend. The Quenching Efficiency is 77 %, 52.2 %, 32.49 %, 32.28 % respectively.

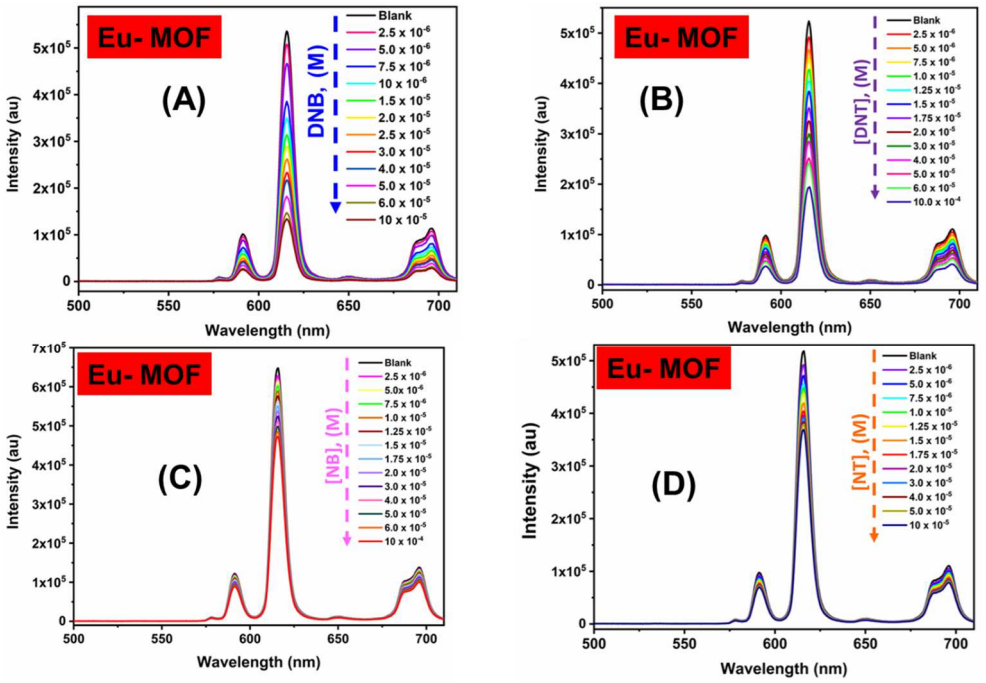

Figure S44. Emission spectra of Eu-bpy MOF dispersed in acetonitrile upon incremental addition of (a) DNB (b) DNT (c) NB (d) NT solution (lex = 350 nm). The final concentration of all the nitroaromatics in the medium is indicated in the legend. The Quenching Efficiency is 75 %, 63.5 %, 28.68 %, 27.62 % respectively.

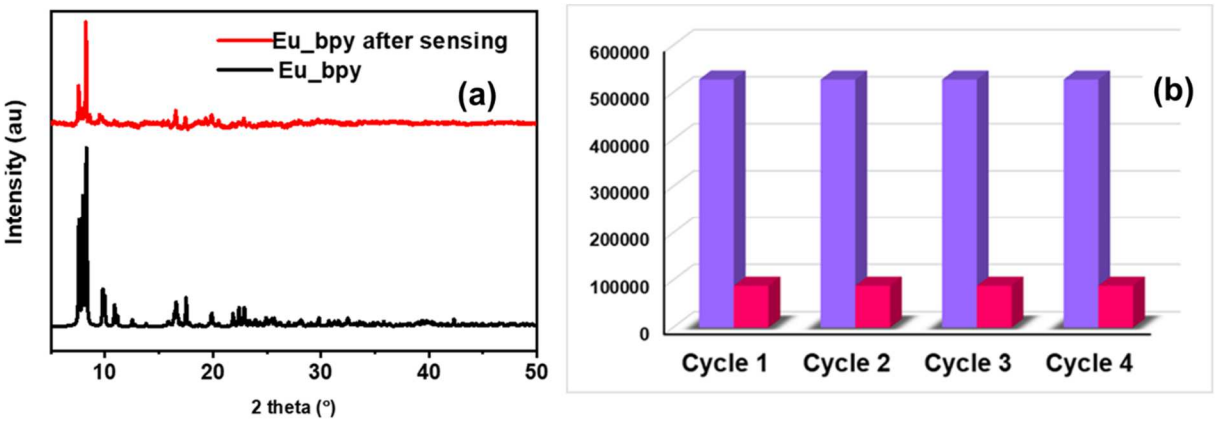

Figure S45. The structural retention of the Eu – bpy MOF after nitroaromatic sensing (a) and recyclability study for the nitroaromatic sensing using the Eu MOF (b).

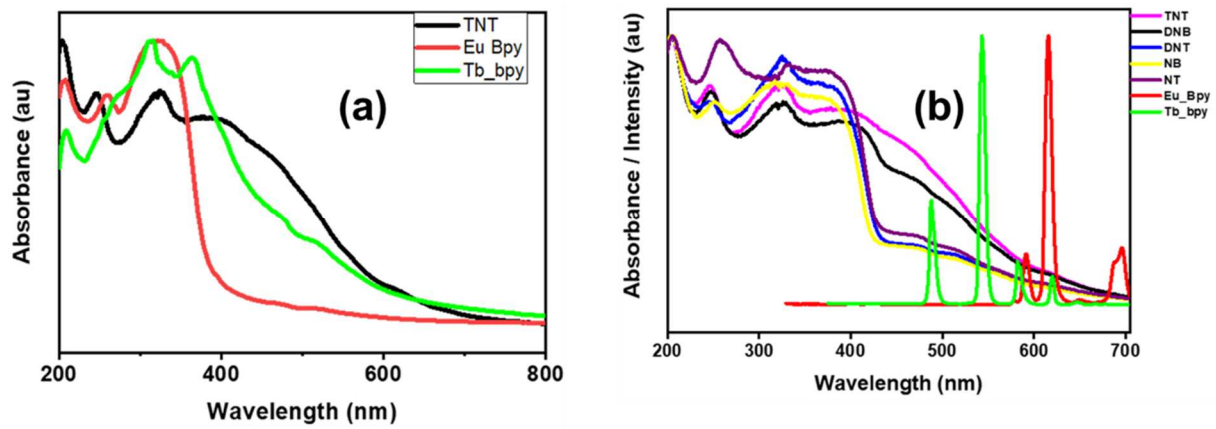

Figure S46. (a) Spectral overlap of the absorption spectra of the trinitrotoluene and the Tb and the Eu – bpy MOF compounds. **(b)** The absorption bands of analytes along with the emission spectra of Eu and Tb MOF. Note the considerable overlap (see text).

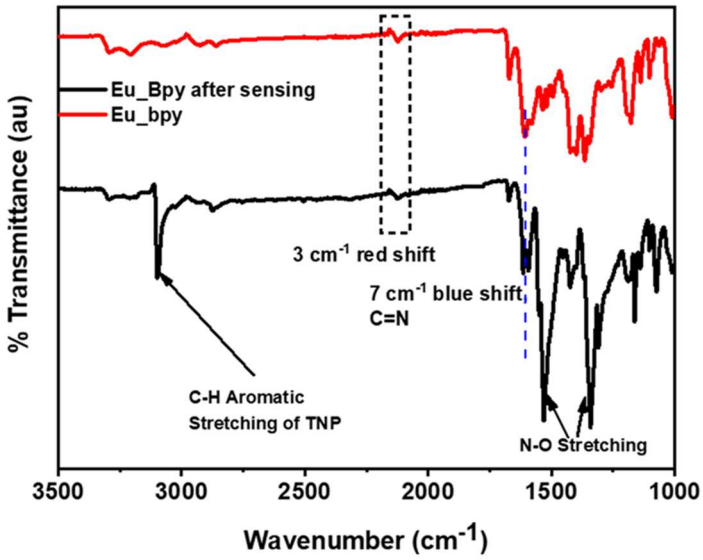

Figure S47. IR spectra of Eu – bpy MOF before and after the pesticide sensing. Note: the shift in the different spectra.

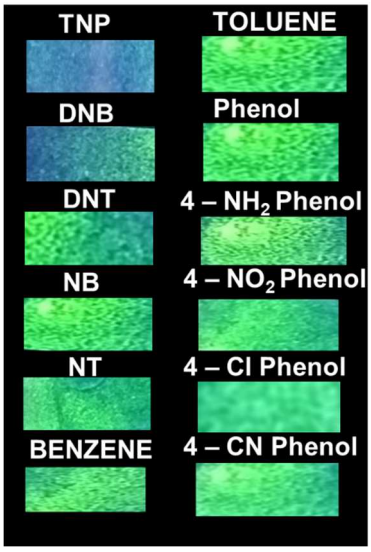

Figure S48. Colour of Tb-bpy coated paper strips in presence of different aromatics. Note: the green colour vanishes only in the presence of TNP

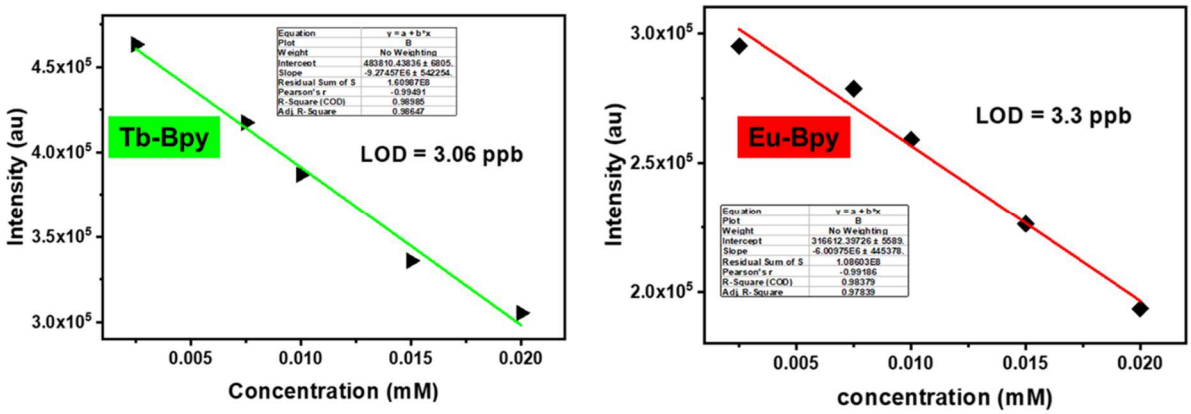

Figure S49: The LOD calculation graph for the TNP using paper strips in Tb-bpy and Eu-bpy.

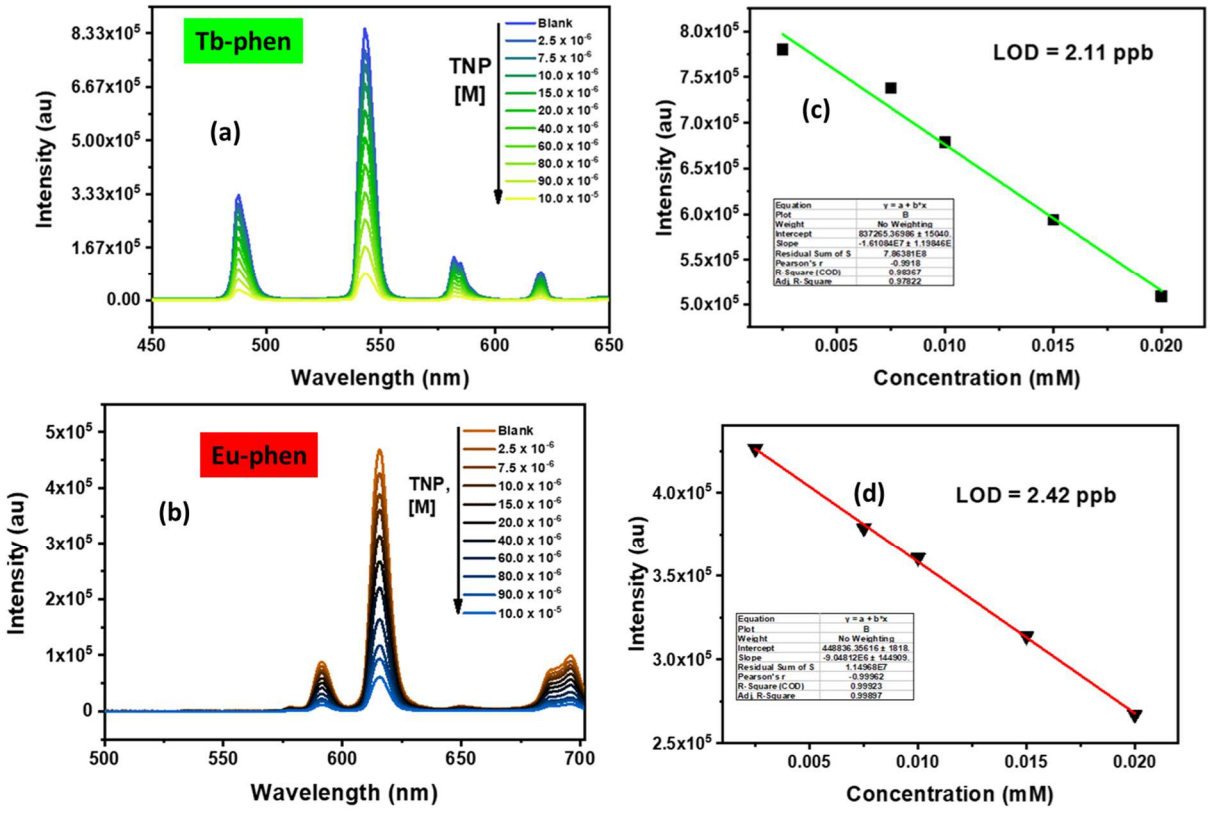

Figure S50: The decrease in luminescence intensity of the MOF coated paper strips dipped in different concentrations of TNP solution **(a)** Tb-phen **(b)** Eu-phen and LOD values for the TNP solution **(c)** Tb-phen **(d)** Eu- phen.

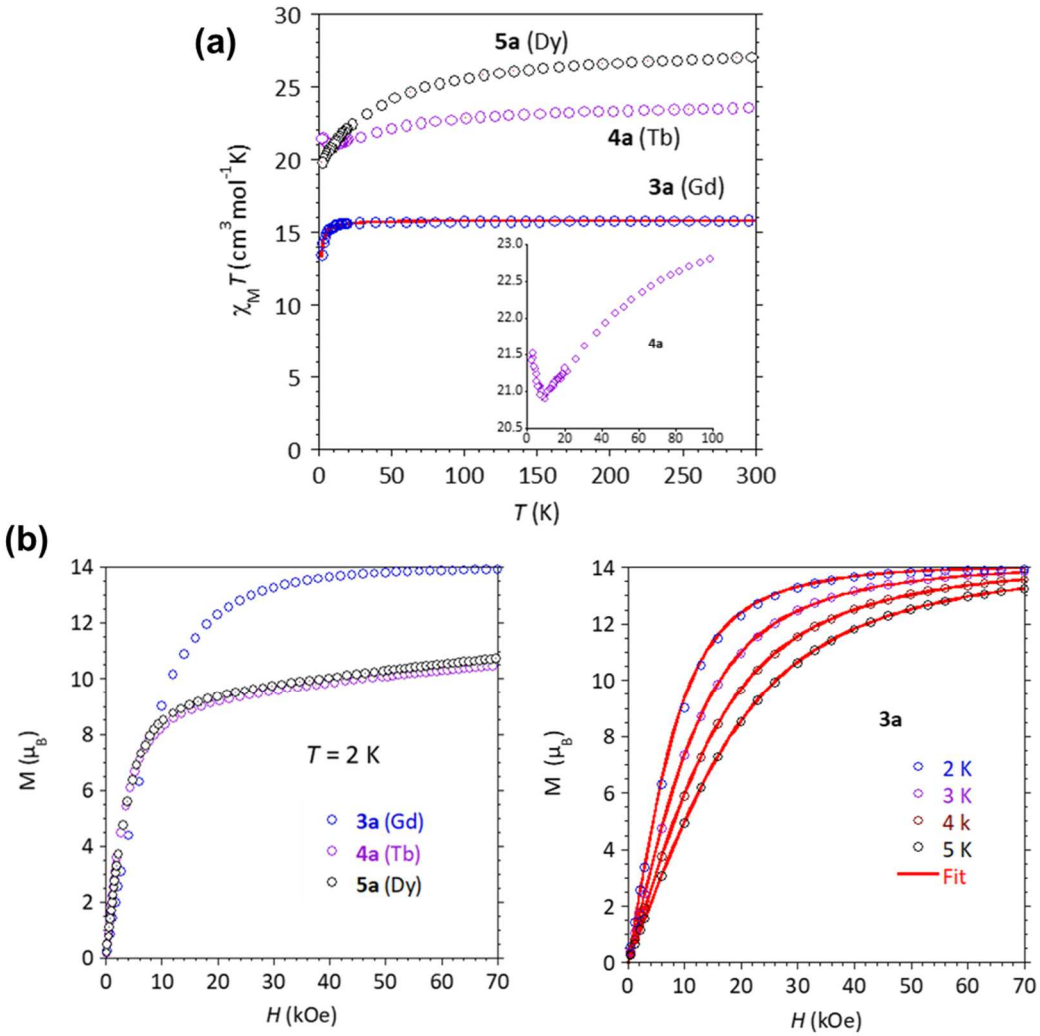

Figure S51. (a) Experimental $\chi_M T$ versus T and (b) M versus H behaviors for **3a**, **4a**, **5a**. The insert in (a) is the low temperature behavior for the Tb derivative. The full line is the calculated behavior for the Gd compound with best-fit parameters J_{GdGd} = -0.041 +/- 0.001 cm^{-1}, g = 2.00 ($H = -J\mathbf{S}_{Gd1}.\mathbf{S}_{Gd2}$).

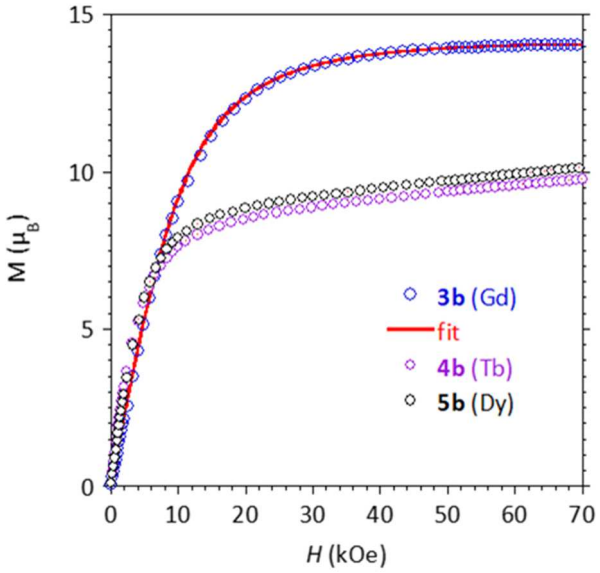

Figure S52. Field dependence of the magnetization of 3b, 4b, and 5b recorded at 2 K.

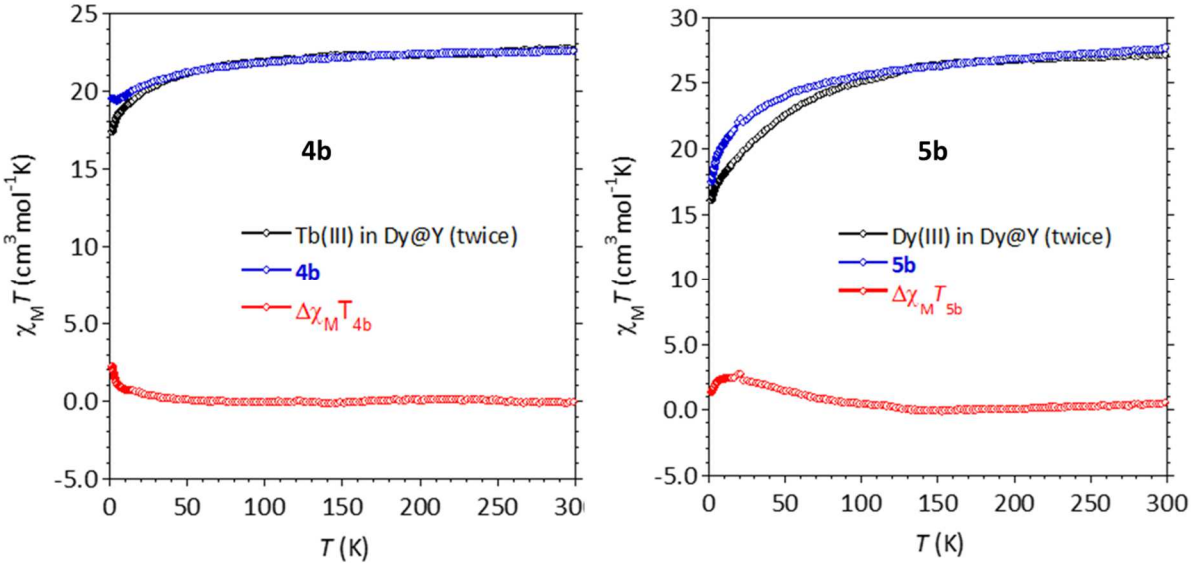

Figure S53. Qualitative Comparison of the $\chi_M T$ versus T behaviors for (a) **4b** and (b) **5b** with the behaviors for isolated Tb(III) and Dy(III) in homologous Y-MOF revealing the contribution ($\Delta\chi_M T$) of the exchange interaction. The contribution of the exchange interaction ($\Delta\chi_M T$ in the plots) was obtained by subtracting the intrinsic magnetic behavior of two isolated Ln ions (i.e. $2\times \chi_M T$ of Ln@Y, black trace below) from $\chi_M T$ of **4b** or **5b**.[21–23] The increase of $\Delta\chi_M T$ at low T is indicative for a ferromagnetic interaction.

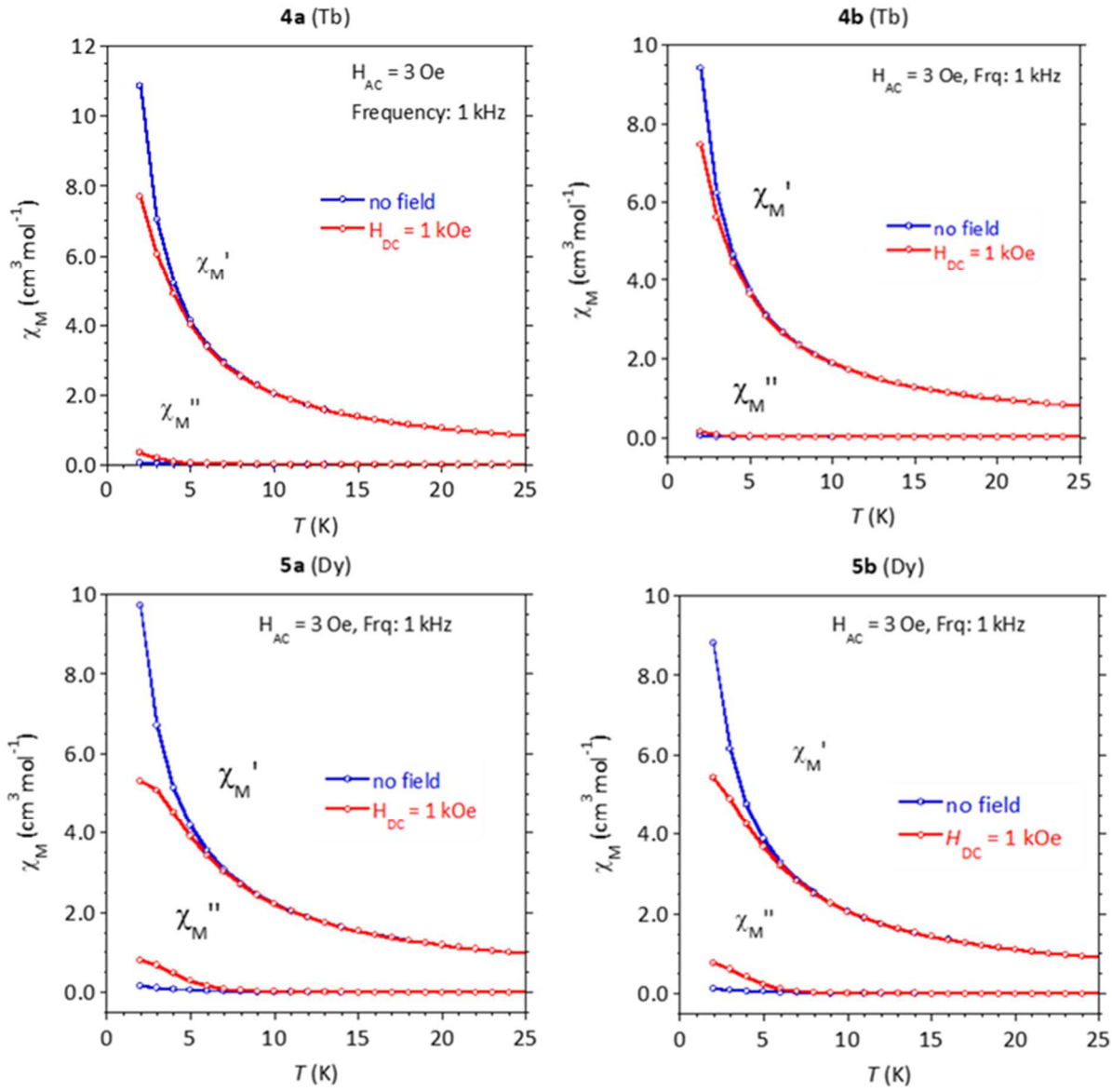

Figure S54. AC susceptibility behaviors for **4a, b** and **5a, b** in absence and with applied static magnetic field (H_{AC} = 3 Oe, ν = 1 kHz).

References:

1 K. Manna, B. Suresh Kumar, T. Maity and S. Natarajan, *ChemNanoMat*, 2022, **8**, e202200081.

2 T. P. Gerasimova and S. A. Katsyuba, *Dalt. Trans.*, 2013, **42**, 1787–1797.

3 A. Schweig and W. Thiel, *J. Electron Spectros. Relat. Phenomena*, 1974, **3**, 27–38.

4 M. M. Campos-Vallette, R. E. Clavijo, F. Mendizabal, W. Zamudio, R. Baraona and G. Diaz, *Vib. Spectrosc.*, 1996, **12**, 37–44.

5 P. G. Sammes and G. Yahioglu, *Chem. Soc. Rev.*, 1994, **23**, 327–334.

6 M. S. Henry and M. Z. Hoffman, *J. Phys. Chem.*, 1979, **83**, 618–625.

7 G. Accorsi, A. Listorti, K. Yoosaf and N. Armaroli, *Chem. Soc. Rev.*, 2009, **38**, 1690–1700.

8 S. Záliš, C. Consani, A. El Nahhas, A. Cannizzo, M. Chergui, F. Hartl and A. Vlček, *Inorganica Chim. Acta*, 2011, **374**, 578–585.

9 N. Sabbatini, M. Guardigli, I. Manet, F. Bolletta and R. Ziessel, *Inorg. Chem.*, 1994, **33**, 955–959.

10 Q.-Y. Yang, K. Wu, J.-J. Jiang, C.-W. Hsu, M. Pan, J.-M. Lehn and C.-Y. Su, *Chem. Commun.*, 2014, **50**, 7702–7704.

11 H. He, F. Sun, T. Borjigin, N. Zhao and G. Zhu, *Dalt. Trans.*, 2014, **43**, 3716–3721.

12 J.-C. Yin, Z. Chang, N. Li, J. He, Z.-X. Fu and X.-H. Bu, *ACS Appl. Mater. Interfaces*, 2020, **12**, 51589–51597.

13 L. Xu, Y. Xu, X. Li, Z. Wang, T. Sun and X. Zhang, *Dalt. Trans.*, 2018, **47**, 16696–16703.

14 R. Peña-Rodríguez, J. A. Molina-González, H. Desirena-Enrriquez, E. Armenta-Jaime, J. M. Rivera and S. E. Castillo-Blum, *J. Mater. Chem. C*, 2021, **9**, 15891–15899.

15 C. Y. Sun, X. L. Wang, X. Zhang, C. Qin, P. Li, Z. M. Su, D. X. Zhu, G. G. Shan, K. Z. Shao, H. Wu and J. Li, *Nat. Commun.*, 2013, **4**, 1–8.

16 L. L. da Luz, B. F. Lucena Viana, G. C. O. da Silva, C. C. Gatto, A. M. Fontes, M. Malta, I. T. Weber, M. O. Rodrigues and S. A. Júnior, *CrystEngComm*, 2014, **16**, 6914–6918.

17 D.-H. Chen, A. E. Sedykh, G. E. Gomez, B. L. Neumeier, J. C. C. Santos, V. Gvilava, R. Maile, C. Feldmann, C. WÖll, C. Janiak, K. Müller-Buschbaum and E. Redel, *Adv. Mater. Interfaces*, 2020, **7**, 2000929.

18 M.-L. Ma, C. Ji and S.-Q. Zang, *Dalt. Trans.*, 2013, **42**, 10579–10586.

19 Y. Wei, R. Sa and K. Wu, *Dalt. Trans.*, 2016, **45**, 18661–18667.

20 K. Manna, J.-P. Sutter and S. Natarajan, *Inorg. Chem.*, , DOI:10.1021/acs.inorgchem.2c02611.

21 M. L. Kahn, J.-P. Sutter, S. Golhen, P. Guionneau, L. Ouahab, O. Kahn and D. Chasseau, *J. Am. Chem. Soc.*, 2000, **122**, 3413–3421.

22 J.-P. Sutter, M. L. Kahn and O. Kahn, *Adv. Mater.*, 1999, **11**, 863–865.

23 J.-P. Sutter and M. L. Kahn, *Magn. Mol. to Mater. 5 Vol. Set*, 2004, 161–187.